AN ABSTRACT OF THE THESIS OF

Irene D. Dumkow for the degree of Doctor of Philosophy in Physics presented on December 1, 1997. Title: Oxygen-deficient $YBa_2Cu_3O_{6+x}$ Films Investigated by Perturbed Angular Correlation Spectroscopy.

Abstract approved: _____ _____

Janet Tate

Perturbed angular correlation spectroscopy (PAC) is well suited to study phase transitions in materials because its sensitivity is temperature independent, unlike that of the related nuclear hyperfine techniques of nuclear quadrupole resonance and Mößbauer spectroscopy. PAC was used to study the normal state of $YBa_2Cu_3O_{6+x}$, a high temperature superconductor which shows unique and interesting features with changing oxygen content. ^{111}In, which substitutes for Y in $YBa_2Cu_3O_{6+x}$, was the PAC probe.

In this thesis, the direction of the main axis of the electric field gradient tensor at the Y site in $YBa_2Cu_3O_{6+x}$ was determined. It points along the chain direction or *b*-axis of fully oxygenated $YBa_2Cu_3O_7$. To establish this result, *a*-axis oriented films were grown and studied by PAC, and the growth mode characterized.

This work also used PAC to establish the origin of a site in some PAC frequency spectra at $\nu_Q = 133$ MHz, $\eta = 0$. This site appears only under strongly reducing conditions. It arises from $CuYO_2$ in the (012) orientation and information about the conditions under which this material forms was gathered, especially with respect to the temperature and pressure. This

material, along with $BaCu_2O_2$ in the (112) orientation, was also observed in x-ray diffraction.

In order to investigate films with varying oxygen content, a system was developed and tested that enabled the oxygen content to be changed reliably. PAC experiments were performed on films with oxygen contents between 6.25 and 7 and it was found that the nuclear quadrupole frequency decreases with decreasing temperature, and that the asymmetry has a maximum for a nominal oxygen content of 6.7. This may be evidence of oxygen ordering. Strong relaxation is observed at all temperatures and this may be a characteristic of the probe rather than the host material.

Oxygen–deficient $YBa_2Cu_3O_{6+x}$ Films Investigated by Perturbed Angular Correlation Spectroscopy

by

Irene D. Dumkow

A THESIS

submitted to

Oregon State University

in partial fulfillment of

the requirement for the

degree of

Doctor of Philosophy

Presented December 1, 1997

Commencement June 1998

Doctor of Philosophy thesis of Irene D. Dumkow presented on December 1, 1997

APPROVED:

Redacted for Privacy

Major Professor, representing Physics

Redacted for Privacy

Chair of Department of Physics

Redacted for Privacy

Dean of Graduate School

I understand that my thesis will become part of the permanent collection of Oregon State University libraries. My signature below authorizes release of my thesis to any reader upon request.

Redacted for Privacy

Irene D. Dumkow, Author

Acknowledgement

I would like to acknowledge the Baden-Württemberg – Oregon exchange program, without which it would not have been possible for me to study at Oregon State University.

My parents supported me financially as well as emotionally by firmly believing that I can reach what I have set out to accomplish.

I have to thank Dr. Janet Tate for all the guidance and support received during the last couple of years. Without her and her door which was always open, this thesis would not exist today.

I have to thank Dr. Roland Platzer for all his expertise in carrying out the PAC measurements. Without him, this thesis would not have been possible.

I have to acknowledge the support of Dr. John Gardner. It was in his laboratories that we took the PAC measurements and he was always there with helpful discussion and suggestions for our data.

I have to thank Dr. Dennis Tom for "showing me the ropes" and having done all the work in developing the evaporation system. I always was grateful about his prompt reply to email questions.

I want to extend my thanks to Dr. Jeanette Roberts and Dr. Goran Karapetrov. They made me feel welcome in the research group and were always willing to answer my questions.

My special thanks go to Dr. Brandon Brown, who always had an open ear to answer questions.

I also want to thank Amy Droegemeier, Eric Moret and Andrew Draeseke , who as the new "crop" will carry on the work in the lab and lifted my spirits quite often.

I would like to thank Dr. A. Sleight for the use of his x-ray diffractometer.

Dr. Roberta Bigelow has been very helpful in performing additional x-ray measurements.

I would like to thank Dr. C. Thomsen for performing the Raman measurement, Dr. L. McIntyre for the RBS measurement and Dr. R. Nielsen for the EMPA measurements.

The financial supports from the Physics Department and the National Science Foundation under grant number DMR 9704052 are gratefully acknowledged.

Table of Contents

Table of Contents (continued)

Table of Contents (continued)

List of Figures

List of Figures (continued)

List of Figures (continued)

List of Figures (continued)

List of Tables

List of Appendices

Oxygen–deficient $YBa_2Cu_3O_{6+x}$ Films Investigated by Perturbed Angular Correlation Spectroscopy

Chapter 1
Introduction

High T_c superconductors, of which $YBa_2Cu_3O_{6+x}$ is the most exhaustively studied, remain very intriguing materials despite 10 years of intensive attention by researchers. The superconducting and normal properties, as well as the crystalline structure, are extremely sensitive to the oxygen content which varies from x=0 to x=1. Depending on the oxygen content, the material either shows superconducting or semiconducting behavior and the structure changes from tetragonal for low oxygen contents to orthorhombic for high oxygen content. The materials are also extremely anisotropic; their properties are different when measured parallel and perpendicular to their trademark Cu–O planes. For the resistivity, this anisotropy ranges from $\rho_c/\rho_{ab} \approx 10^5$ for $Bi_{2+x}Sr_{2-y}CuO_{6+\delta}$ [1] to $\rho_c/\rho_{ab} \approx 100$ for $YBa_2Cu_3O_{7-\delta}$ [1], one of the more isotropic high T_c–materials.

The most reproducible information for the $YBa_2Cu_3O_{6+x}$ system has come from the single crystal material. While much of this is applicable to both thin–film and single–crystal forms of the materials, there remain important differences between them, mostly having to do with processing and disorder issues. These are of crucial importance for applications, particularly those which require films in different crystallographic

---

[1] Both $YBa_2Cu_3O_{6+x}$ and $YBa_2Cu_3O_{7-\delta}$ are used in this thesis. $YBa_2Cu_3O_{6+x}$ usually, but not always, implies that one is looking at oxygen–deficient material, while $YBa_2Cu_3O_{7-\delta}$ is most commonly used for optimally prepared material.

orientations. This thesis focuses on thin–film $YBa_2Cu_3O_{6+x}$, and makes use of a unique thin–film facility capable of introducing radioactive isotopes into thin–film superconductors during the growth process. This allows the use of the hyperfine technique, perturbed angular correlation spectroscopy (PAC), to investigate features of the structure of $YBa_2Cu_3O_{6+x}$, as well as to identify impurity phases. The remainder of chapter 1 discusses some general properties of $YBa_2Cu_3O_{7-\delta}$ and takes a brief look at the importance of the oxygen content. Chapter 2 discusses the growth of the films and how to change the oxygen content, while chapter 3 focuses on the characterization of the films. Chapter 4 is a review of the work to date on PAC in $YBa_2Cu_3O_{6+x}$, and describes the experimental set up and data analysis. Chapters 5 and 6 present the main experimental results of this thesis – X-ray and PAC investigations of both *a*- and *c*-axis oriented $YBa_2Cu_3O_{6+x}$ films with varying oxygen content. Chapter 7 summarizes the results and includes prospects for future investigations.

1.1 Structure of $YBa_2Cu_3O_{6+x}$

Superconductivity has been subject of research since 1911, when H. Kamerlingh Onnes discovered that mercury became superconducting below 4.15K [2]. The era of high–temperature superconductivity was initiated in 1986, when Müller and Bednorz first published their results [3] of superconductivity at 36 K in a lanthanum barium copper oxide. After confirmation of this discovery, which was especially surprising because it was believed at that time that superconductivity could not exist above 30 K, a flurry of research activity started, and intensified when it was discovered that the yttrium–barium-copper-oxygen system became superconducting at $\approx$ 90 K

[4], replacing the need for liquid helium as a cooling medium by liquid nitrogen, which is cheaper and easier to handle. From the start, there has been interest in growing these materials as thin films. This is due to the fact that thin–film superconductors can be used for devices and the potential to operate superconducting devices at the commercially viable temperature of 77 K is an exciting prospect. Nowadays, process issues have been resolved and commercially produced devices are available.

$YBa_2Cu_3O_{6+x}$ structure is based on the perovskite structure. A true perovskite has the formula ABO_3. Fig. 1.1 shows the structure, which is a body centered cube, the A atoms occupying the corners of the cube, while the B atoms occupy the body-centers. The oxygen atoms are on each of the edges of the cube.

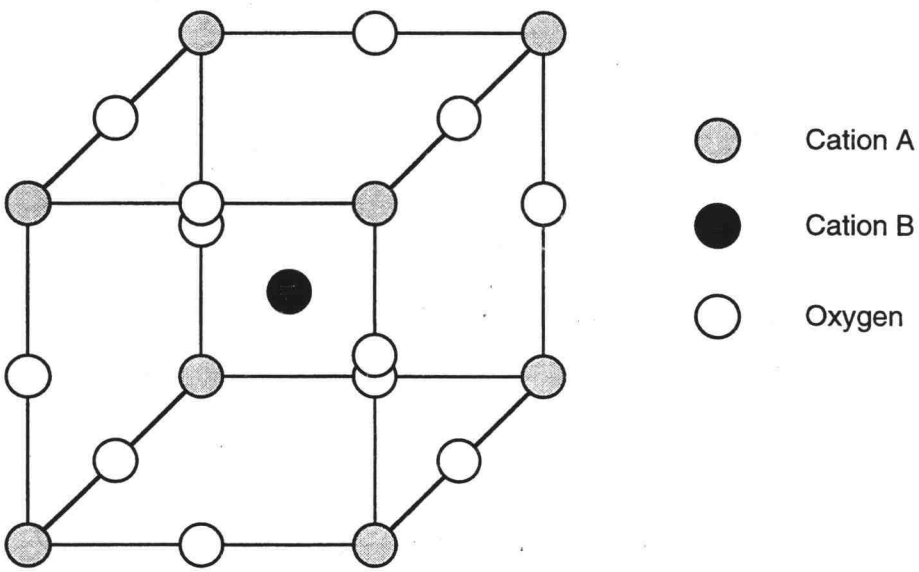

Fig. 1.1 The structure of an ideal perovskite. They can either be cubic, tetragonal or orthorhomic, e.g. $BaTiO_3$ can be all three of them, depending on the temperature.

The $YBa_2Cu_3O_{6+x}$ structure has three such cubes, each of which is deficient in some of the oxygen atoms. The Cu atoms occupy the A site, while the position of the B site is taken up by either the Ba or Y. In the Y cube, the oxygen atoms at the same height as the Y atoms are missing, while the lower and upper oxygen-sites are fully occupied. This leaves the Y atom sandwiched between two Cu–O sheets or planes, which are the site of the superconductivity. In the case of the Ba cube, the picture is more complicated. The oxygen atoms at the height of the Ba are there, as are all the oxygen atoms at the side it shares with the Y cube. At the side that is left, there is great

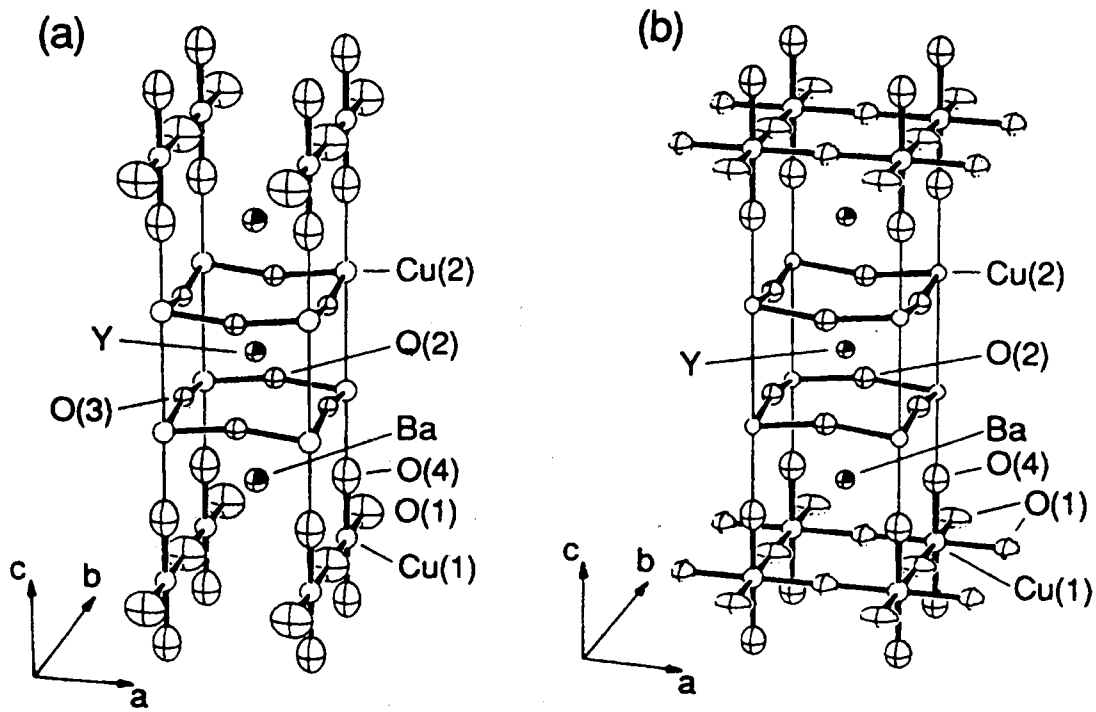

Fig. 1.2 Sketches of the fully oxygenated $YBa_2Cu_3O_7$ (a) structure and the oxygen-deficient $YBa_2Cu_3O_6$ (b) structure. Thermal vibration ellipsoids are shown for the atoms. In the orthorhombic $YBa_2Cu_3O_7$ structure the oxygen O(1) atoms are arranged in long chains along the *b*-axis, in the tetragonal $YBa_2Cu_3O_6$ structure, the O(1) oxygen atoms are randomly distributed in the basal plane. (Plots taken from [5])

variability in the number of oxygen atoms, with consequences for the structure and the superconductivity, which will be shown later in this thesis. Fig. 1.2 shows the structure of both the fully oxygenated $YBa_2Cu_3O_7$ and the oxygen–deficient $YBa_2Cu_3O_6$ and comparing this to the ideal perovskite structure helps to see the differences.

In the case of fully oxygenated $YBa_2Cu_3O_{6+x}$ ($x \approx 1$), two of the possible four sites are occupied and the oxygen atoms form long chains along the *b*-direction in conjunction with the Cu atoms. These chains give the material an overall orthorhombic structure, with ideal values for a=3.82Å, b=3.89Å and c=11.68Å [5]. The more oxygen is taken out, the more the *a*- and *b*-axis

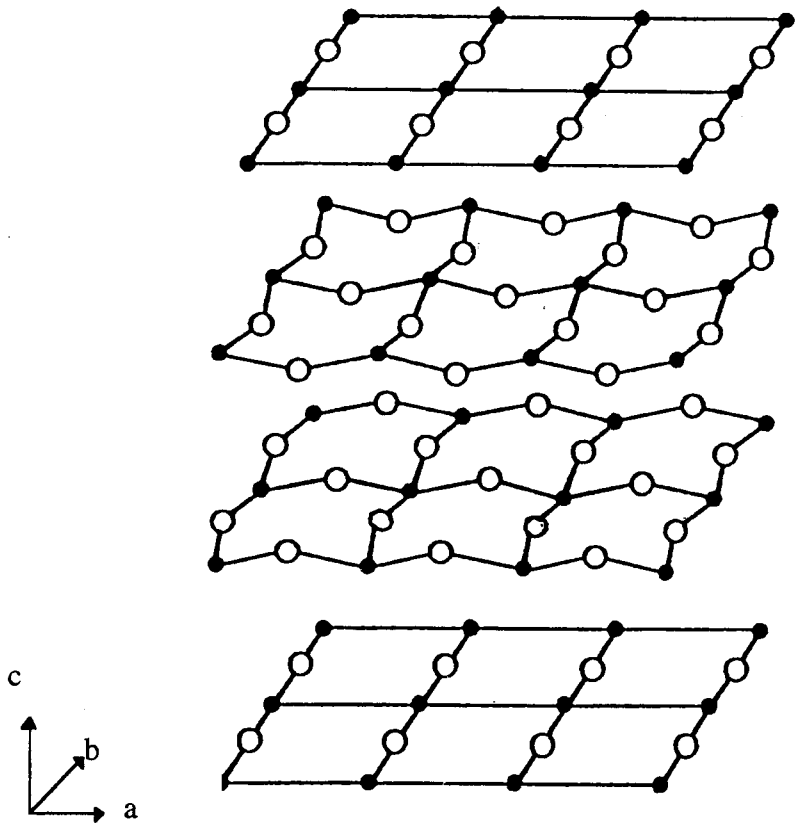

Fig. 1.3 Sketch showing the buckling of the Cu–O planes. Due to symmetry, the Cu–O chains are perfectly straight (Sketch from [6])

become equivalent, with an orthorhombic–to–tetragonal transition at $x \approx 0.35$. In the fully oxygenated $YBa_2Cu_3O_7$, the Cu–O planes are buckled, see Fig. 1.3, but with decreasing oxygen content, the planes straighten, which explains why the *c*-axis lattice parameter increases with decreasing oxygen content.

This thesis is concerned mostly with the structure of the material and approaches it from several different points of view. Perturbed angular correlation spectroscopy (PAC), a hyperfine technique which is based on the interaction of the quadrupole moment of a probe atom with the distribution of charges around said atom, can be used to measure the orientation of the electric field gradient, which is a tensor quantity. Yet our films are twinned, as a consequence of the way they grow, and at the start of the investigation we only knew that the main axis of the electric field gradient lies in the *ab*-plane. The first goal was therefore to grow films with the *a*-axis normal to the substrate as opposed to the films we grew before, which had the *c*-axis normal to the substrate.

After being able to grow the films with different orientations, we are now trying to take a closer look at the role of oxygen in the material. This interest was sparked by the fact that it is relatively easy to grow $YBa_2Cu_3O_{6+x}$ with an oxygen content of $x \approx 7$ in the orthorhombic structure or of $x \approx 6.25$ in the tetragonal structure. In order to vary the oxygen content more, we first had to learn as much as possible about what happens during the growth and anneal right after the deposition. After investigating options of changing the oxygen content right after the deposition, which did not prove to be very reliable, we turned to building a system to change the oxygen content in a post-deposition anneal outside the main evaporation chamber, which gives us more control over the whole process.

1.2 Differences Between Crystals and Films

Even though crystals and thin films of $YBa_2Cu_3O_{6+x}$ are made of the same material, often they seem to be two very different beasts. This is already evident in the preparation methods, which make the films more susceptible to small changes in preparation. While papers dealing with crystals seem to have reached some consensus about the properties of $YBa_2Cu_3O_{6+x}$, this consensus has not quite been reached for films, making them at the same time an interesting and challenging subject to study.

To see the difference between crystals and films, it is instructive to look at the methods of preparation and the time-frames involved. In order to grow good crystalline material, materials are usually mixed, sintered, ground and reground and annealed several times in flowing oxygen. Jorgensen *et al.* [5], for example, mixed powder of Y_2O_3, $BaCO_3$ and CuO in the right proportions, after they were individually prescreened through 200 mesh. This mixture was pressed into pellets and put into a platinum crucible. The pellets were heated to 960 °C in flowing oxygen and annealed for 24 h. Afterwards they were cooled in air, ground to 200 mesh, remixed and pressed again into pellets. Again they were taken up to 960 °C in flowing oxygen and kept there for 24 h. Afterward the temperature was reduced to 670 °C and held for 24 h followed by a cool-down to ambient temperature at 5°C/min. The sample spends three days at a constant temperature and that does not include heating and cooling. For single crystals, the annealing times are often several weeks in order to completely oxygenate the crystal [7].

Compared to this elaborate and time-consuming procedure, making a films of $YBa_2Cu_3O_{6+x}$ is fast. There are several different methods commonly used to deposit films, the most widely used being sputtering, laser ablation,

evaporation techniques like MBE (molecular beam epitaxy) and reactive co-evaporation, and chemical vapor deposition. In our case, using reactive co-evaporation, the deposition is over in about 4 min. for a 2000Å thick film, resulting in a deposition rate of 500Å/min or about 8Å/s, which is very fast. Using the slower sputtering technique , Burmann *et al.* [8] investigated the influence of the deposition rate on the orientation, used deposition rates between 0.2Å/s (12Å/min) and 1.8Å/s (108Å/min), or 20 min to 3 hours for a 2000Å thick film. We usually follow the deposition by an anneal lasting for 30 minutes at a pressure of 15 torr.

Because of these differences in preparation methods, one can consider the crystals to be in equilibrium and having had enough time to equilibrate, while the films might not have had time to equilibrate. This is also obvious in the published papers, where the papers on crystals are more likely to agree with each other, while papers on thin films are very dependent on the preparation method used and the treatment after deposition. In addition, published papers on films and crystals are not necessarily in agreement with each other, showing that films are more disordered than crystals and results from films should be considered within the context of the preparation method.

1.3 Examples of Differences between Films and Crystals

The oxygen content of $YBa_2Cu_3O_{6+x}$ is very important, because it is strongly related to the properties of $YBa_2Cu_3O_{6+x}$. There are several established methods to measure the oxygen content in crystals, some of which are available only for crystals. The most common ones for crystals are idiometric titration and graviometry. For idiometric titration, see Refs. [9] and [10], the

sample is dissolved in an acidic solution of KI. This results in the reduction of all copper to solid Cu(+I) iodide. Back-titration of the liberated iodine by thiosulfate gives the average oxidation state of copper, from which the oxygen content of the sample can be calculated. In order to determine the oxygen content by graviometry, one measures the weight loss while the sample is heated in an nitrogen atmosphere (this is done especially when the exploration of the phase-diagram is of interest) or in a reducing atmosphere. In that case, the reduction products have to be known [9]. Neither method works for films, because a thin film does not provide enough material. Either method can be used to calibrate other methods which can be used on films. Several groups doing research on oxygen–deficient films usually had some bulk material in the vicinity when they were taking oxygen out of films, and used the bulk material to establish the oxygen content. Apart from providing a means to establish the oxygen content, the bulk material stabilizes the films and prevents decomposition [11].

1.3.1 *Tc versus Oxygen Content*

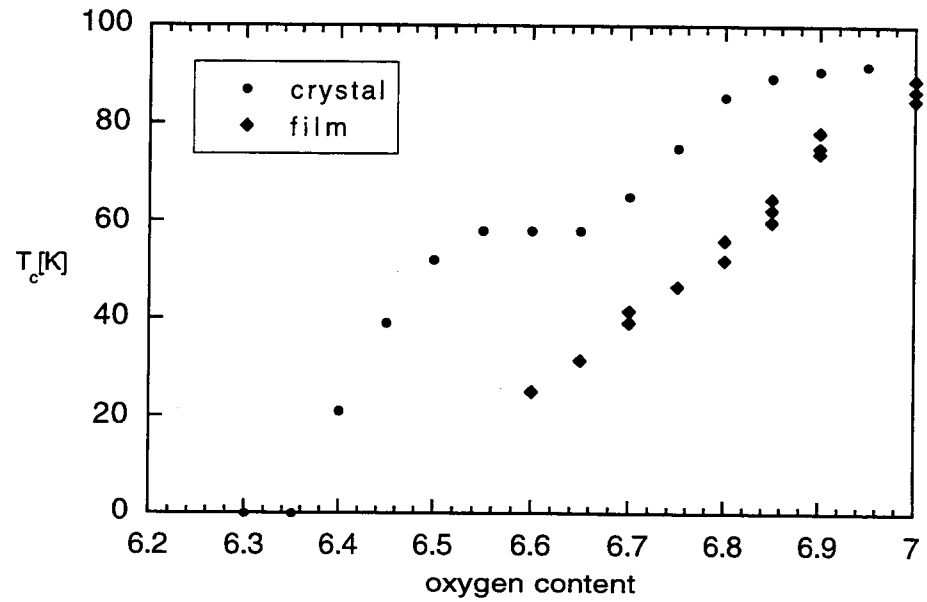

Fig. 1.4 T_c vs oxygen content for crystals and films. The crystal curve is from Ref. [5] and is taken from a fit to their measured data; the oxygen content determined from weight loss. The film data is from [12] who infer the oxygen content from the anneal procedure and are careful to refer to it as "nominal".

T_c is greatly influenced by the oxygen content. Usually the T_c versus δ (oxygen deficiency)[2] curve shows two marked plateaux, one at 90 K, for $\delta<0.2$, the other at 60 K, for $0.3<\delta<0.5$, with the material becoming semiconducting for $\delta>0.65$ [5]. In films this behavior seems to be less pronounced and there are papers published which show no plateaux at all. A good example is in Ref. [12]. Fig. 1.4 is a comparison between the data published by Jorgensen *et al.* [5] and Osquiguil *et al.* [12]. For the films, the plot of T_c versus δ looks linear and there is no hint of a plateau. Taking the same T_c, one would determine two

[2] δ is normally used to indicate the oxygen deficiency from a fully oxygenated O_7; x is used to indicate the oxygen content, from the oxygen-deficient O_6. Occasionally, x is also used to indicate the total amount of oxygen.

very different oxygen contents for a crystal or film sample. Osquiguil *et al.* [12] are very careful about calling their oxygen content nominal and state that the same behavior has also been observed in pellets of $YBa_2Cu_3O_{6+x}$, which were quenched from temperature between 650 °C and 550 °C, depending on the annealing atmosphere, either pure O_2, air, or 5%O_2, 95% N_2 [13].

1.3.2 c-Axis Length versus Oxygen Content

The *c*-axis length is a very reliable indicator of the oxygen content in a crystal, yet in films it should be used very carefully. A good example is from Ref. [14], which compares the *c*-axis length of oxygen–deficient films with the same length for oxygen–deficient crystals given in Ref. [5][3]. In the comparative graph, the *c*-axis length for films is greater by about 0.03 to 0.04Å for the whole range of oxygen contents.

The usual suspects for the well–known expanded *c*-axis length of $YBa_2Cu_3O_{6+x}$ thin films are strain, because the film is mismatched to the substrate, and cation disorder, though oxygen disorder might also be possible. Ref. [15] has an in–depth discussion about the possible reasons for the *c*-axis length expansion, summing up the general reasons. They consider insufficient oxygen unlikely because of high T_c's ($\approx$ 90 K) and exclude substrate strain because the *a*- and *b*-parameters are not expanded. They claim that extended defects are unlikely to cause the expansion, because that would give a distribution of lattice parameters. This leaves them with cation disorder

---

[3] As an interesting aside, the *c*-axis length expands if oxygen is taken out. This seems to be counterintuitive, but has to do with the fact that the Cu–O planes, which are buckled in the fully oxygenated material, straighten with decreasing oxygen content[5].

(especially Ba substituting on the Y site) as the likeliest candidate for the *c*-axis parameter expansion.

Another paper that nicely shows how much one has to be careful with determining the oxygen content of films is Ref. [16]. Using Raman spectroscopy, they find in several of their films the oxygen content to be > 7 if they use the published empirical formula (for example in Ref. [17]), which determines the oxygen content from the frequency of the O(4) line, the 500 cm^{-1} line. From their *c*-axis length (which they seem to compare to crystal data), the film oxygen content is below 7, which makes more sense. They also attribute these discrepancies to strain and disorder.

1.4 Role of Oxygen

As is obvious from the preceding paragraph, oxygen is very important in $YBa_2Cu_3O_{6+x}$ and a lot of research has gone into investigating oxygen. The oxygen content is tied to electrical and structural properties and especially the electrical properties are important from an applications point of view. In addition, because the oxygen content can vary between 6 and 7, the question arises about how the oxygen atoms are arranged. It is also noteworthy that the structure actually provides space for 9 oxygen atoms, evident in some of the earliest papers, where the formula $YBa_2Cu_3O_{9-\delta}$ was used, and even if one neglects the possible oxygen atoms on the Y level, one could naively expect the structure to have 8 oxygen atoms in it. Ref. [6] gives a short sketch on how the scientific community realized that $YBa_2Cu_3O_{7-\delta}$ was the correct formula instead of $YBa_2Cu_3O_{9-\delta}$.

1.4.1 Chain Length and Charge Transfer

In the completely oxygenated structure the planes are the place where the electronic transport takes place, but the chains play an important role in it. The hole concentration in the planes depends on the oxygen concentration and ordering in the chains [18]. Transfer of charge from the chains to the planes increases the hole concentration in the planes [19]. The chains are therefore considered a "charge reservoir". In order to do that the chains need to have a certain length. Ref. [20] shows that a minimum chain length of four Cu–O segments is required in order to initiate the charge transfer from the chains to the planes.

1.4.2 Oxygen Ordering: Experiment and Theory

The fully oxygenated $YBa_2Cu_3O_7$ has only half of the possible oxygen sites in the basal plane filled and the more oxygen is taken out, the more possible sites are available to the remaining oxygen atoms. These oxygen atoms can be arranged in ordered ways and the arrangement of the oxygen atoms is of great importance, but experimental and the theoretical research have been difficult to reconcile. Oxygen is very hard to image directly and experimental techniques usually rely on diffraction techniques which need order over rather large areas (several 100 Å). Computational techniques, on the other hand, consider the atomic level and, if anything, might have a problem of covering too small an area due to limited computing power.

There are two main models used to explain oxygen ordering which yield two different kinds of ordering. Before explaining the models in more

detail, one has to clarify the interactions between the oxygen and copper atoms. Fig. 1.5 shows the interactions used by the models.

V_1 is the potential between two oxygen atoms at 90° to a copper atom (nearest neighbor interaction). V_3 is the potential between two oxygen atoms across the unit cell, and V_2 is the potential between two oxygen atoms mediated by a copper atoms; both are next nearest neighbor interactions. V_1 and V_3 are assumed to be repulsive, but V_2 is the potential which is responsible for the difference between the different models and can be either attractive or repulsive.

In the ASYNNNI model (asymmetric-next-nearest-neighbor-interaction Ising model), first proposed in Ref. [21] the potential V_2 is assumed to be attractive, with the conditions $V_2<0<V_3<V_1$. As a consequence, this model predicts that only long chains are stable and for example predicts a doubling of the unit cell for x=0.5 with every second chain unoccupied with respect to the fully oxygenated material (which follows from the weakly repulsive V_3).

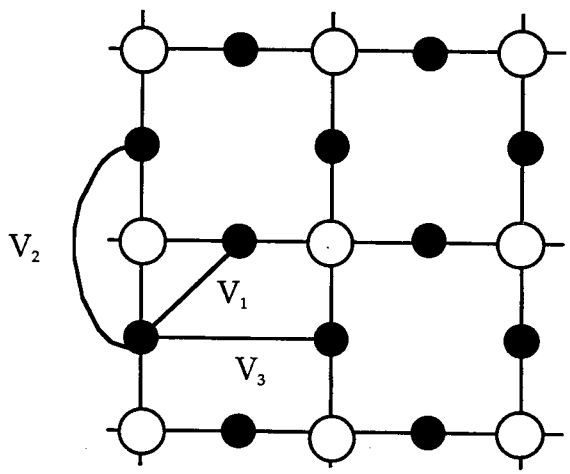

Fig. 1.5 Definition of the potentials between oxygen and copper atoms. Filled circles represent Cu atoms, white circles oxygen atoms.

In another widely used model proposed in Ref. [22], there is a strong repulsion between all the oxygen atoms, including V_2. As a consequence, this model leads to the formation of only the basic O–Cu–O fragments, but not the formation of any kind of chains.

The difference between the two models can be seen most clearly if one looks at the prediction of the order for an oxygen content of 6.5. In the case of the ASYNNNI model the oxygen atoms order in long chains, with every second chain missing with respect to the fully oxygenated structure. For the second model, the oxygen atoms order in the so-called herring-bone structure which is distinctively different from the chain structure, as can be seen in Fig. 1.6.

It seems that it should be fairly simple to decide between these two models, especially around an oxygen content of 6.5, because the ordering

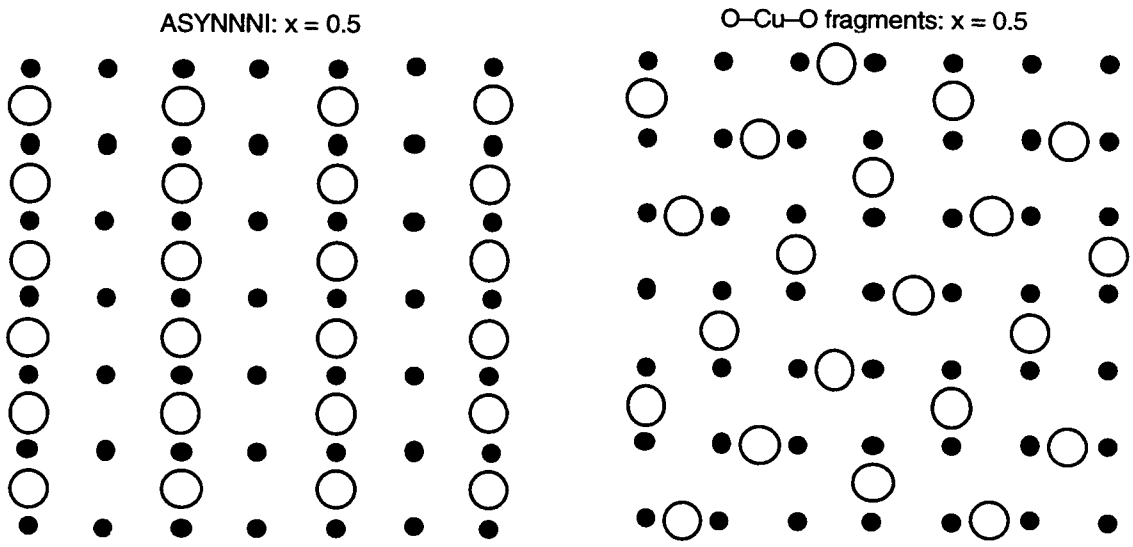

Fig. 1.6 Examples of the ordering of oxygen atoms in the basal plane for an oxygen content of 6.5. Filled circles represent Cu atoms, the open circles represent oxygen atoms. The ASYNNNI model predicts long chains, with every other row unoccupied. For O–Cu–O fragments, the predicted structure is reminiscent of a herring-bone weave.

proposed by the ASYNNNI model clearly has an orthorhombic structure to it, while the other model has an average tetragonal structure. Yet experimentalists have had difficulty establishing the validity of either of the models. This is mostly due to the fact that these techniques have to rely on diffraction and therefore average over larger areas, while in reality, the order can be fairly easily disturbed, for example by grain boundary and dislocations. Some experiments indicate that there also might be a cross-over in the interaction V_2 from being repulsive to attractive, depending on the size of the rare earth ion [20].

An additional ordering phenomenon in $YBa_2Cu_3O_{6+x}$ is the so-called room-temperature annealing. Even at rather low temperatures of room-temperature and slightly above, the oxygen atoms can rearrange. This in turn affects the transition temperature and X-ray spectrum [23] and happens for the orthorhombic as well as the tetragonal structure. Ref. [23] shows the example of a $YBa_2Cu_3O_{6.45}$ sample that took several days to reach its final T_c of $\approx$ 44 K (starting at 35 K) at room temperature and of another $YBa_2Cu_3O_{6.45}$ sample that took several weeks at 0 °C to reach its final T_c of $\approx$ 46 K (starting at 39 K). Furthermore, in x-ray diffraction studies, they see a sharpening of the (400) and (040) peaks over time for samples with different oxygen contents. This is most pronounced for the samples with an oxygen content of 6.30 (tetragonal) and 6.35 (orthorhombic) and happens over $\approx$ 40 h. In neutron diffraction experiments ([24]), a relaxation of the *a*- and *c*-axis parameters is seen, again indicative of oxygen ordering.

Chapter 2
Sample Preparation

2.1 Thin Film Deposition Techniques

Shortly after the discovery of the HTSC's, scientists started to grow thin films of the material. Several different techniques have been used, each with its own set of advantages and disadvantages. One usually differentiates between physical (sputtering, MBE, e-beam) and chemical (MOCVD) deposition techniques. During a physical deposition, generally no chemical reactions occur (but there are some methods during which a chemical reaction occurs, especially if oxygen is introduced). During a chemical deposition, there always is a chemical reaction. In addition, the deposition can either happen in the vapor phase or in the liquid phase. In this discussion, I divide the different techniques as applied to $YBa_2Cu_3O_{6+x}$ into two groups according to the control of stoichiometry.

The first group contains techniques which use a target made of $YBa_2Cu_3O_{7-\delta}$ in the right composition, which is evaporated by some means. For example, ions may bombard the target and therefore transfer momentum to the surface atoms. This is known as sputtering. In the case of laser ablation, a laser is directed at the target and evaporates the material. The plume created then deposits the $YBa_2Cu_3O_{6+x}$ on the substrate. The advantage, and at the same time, disadvantage, of these methods is that the target has to have the right composition. In some methods, the stoichiometry of the target is transferred to the film. In others, some target species are preferentially transferred, so that the film has a different stoichiometry. This difference may vary with deposition conditions, and has to be carefully established. Ref. [25]

shows that using a stoichiometric target (Ba/Y = 2), gives the best films if an oxygen pressure of 80 mtorr during sputtering. If they decrease the oxygen pressure to 5 mtorr, the best films are deposited if the target has a Ba/Y ratio of 1. They do not do any compositional analysis on the film itself.

The second group of deposition techniques evaporates the constituent materials separately. In the simplest case, the evaporation is achieved by placing the constituent metals into metal boats and resistively heating them. The evaporation can also be effected using electron beams or Knudsen effusion cells, which produce very directed evaporant streams. Because the metals are evaporated individually, the composition can be changed during the deposition. On the other hand, three rates have to be kept constant in the case of $YBa_2Cu_3O_{7-\delta}$ as opposed to just one in the case of the techniques like sputtering from one target.

Chemical vapor deposition (CVD) belongs into the second group. CVD is usually used to provide coatings over large areas. In order to deposit $YBa_2Cu_3O_{7-\delta}$, MOCVD (metallo-organic CVD) is usually used. Because the carrier gases are based on carbon derivatives, films deposited by MOCVD usually contain carbon impurities.

2.2 Reactive Co-Evaporation

Our films are deposited by a technique called reactive coevaporation. Evaporation of the material can be achieved by several means. In our case, the metals, Y, Ba and Cu are evaporated from metal boats, depending on the material either W (for Y), Ta (for Ba) or Mo (for Cu). These boats are resistively heated and the evaporation rates are kept constant with the help of feed-back loops. An important point to keep in mind for the design of an

evaporation system is that the evaporant does not uniformly coat the substrate, but the thickness falls off from the center according to the following formula (for a small area source):

$$\frac{d}{d_0} = \left[1 + \left(\frac{l}{h}\right)^2\right]^{-2} \tag{2.1}$$

with d the thickness at a point l from the center of the substrate and h the substrate-source distance [26].

"Coevaporation" refers to the simultaneous evaporation of materials. This adds problems mostly from a design point of view. The advantage is that film stoichiometry can be easily varied, but it adds design complexity. Several sources have to be regulated at the same time. This either means using a technique which can pick the different species out of the evaporant stream (like mass-spectrometry) or assuring that each detector is exposed to the stream from only one source (our technique).

"Reactive" refers to the introduction of oxygen close to the substrate to facilitate formation of the oxide. This is unusual; most evaporation techniques try to use as low a background pressure as possible because the mean free path decreases with increasing pressure from 500 cm at 10^{-5} torr to 5 cm at 10^{-3} torr and 5 mm at 10^{-2} torr. For $YBa_2Cu_3O_{7-\delta}$ it was shown very early on, that the "in–situ" process, whereby oxygen was introduced during the deposition in order to grow the material, produced films with far better structure and qualities than those produced by "ex–situ" processes where the oxide formation was performed after in–vacuo deposition. The in–situ process seldom requires local pressures greater than 10^{-4} torr, where the mean free path is still of the order of 50 cm. This means that even though collisions between the evaporated metals and the oxygen might occur in the gas phase resulting in the formation of metal oxides, the probability is very small.

Instead, the formation of the material will take place at the substrate, which is exposed to a high incidence of metal and oxygen particles [26].

2.3 Factors Influencing the Film Growth

It should be already clear that there are several parameters which influence the film growth and therefore the quality of the film grown. The most important factors are the stoichiometry, evaporation rates, the temperature of the substrate during the deposition, the oxygen pressure during the deposition, the substrate temperature during the annealing and pressure during the annealing. Several additional factors can influence the quality of the film, but are not well controlled in our system, like the quality of the substrate, and the surface cleanliness. In addition, these parameters are not all independent. The following gives examples of what the individual parameters mostly influence.

2.3.1 Stoichiometry

Even though it seems obvious that the individual rates should be set as to achieve the perfect 1:2:3 stoichiometry, Dr. Dennis Tom in his thesis [27] showed that the best film are films which are slightly copper-rich.

2.3.2 Substrate Temperature During the Deposition

This is the crucial factor in order to achieve the desired orientation. The substrate temperature has to be higher to grow *c*-axis oriented films and lower to grow *a*-axis oriented films (the actual temperatures strongly depend

on the technique used, but there is ≈ 100 °C difference for the two orientations). On the other hand, it has to be high enough (the lower limit was never actually determined, but ≈ 550 °C is probably a good guess) to grow films that are oriented.

2.3.3 Oxygen Pressure During Deposition

Some oxygen (pressure depends on the technique used) has to be supplied during the deposition, otherwise the material will not grow. Depositing just barium, copper and yttrium at the same time without oxygen and then annealing it in oxygen will grow an amorphous material (as evidenced unintentionally by a PAC run) rather than oriented $YBa_2Cu_3O_{6+x}$.

2.3.4 Postanneal: Oxygen Pressure

This parameter influences the length of the *c*-axis parameter and it also changes the oxygen content. There is a known correlation between the *c*-axis length and the oxygen content for crystals, but because films are more disordered than crystals, this relationship cannot be simply carried over, but has to be carefully checked, as illustrated in Chapter 1.

2.3.5 Postanneal: Substrate Temperature

Not much investigation was done by me into this parameter. In the case of the tetragonal $YBa_2Cu_3O_{6.25}$ films, which were produced by adding an anneal in vacuum after the "standard" deposition, the higher the substrate

temperature is during the anneal, the more we produce of the impurities $BaCu_2O_2$ and $CuYO_2$.

2.4 Description of the Evaporation System

A very detailed description of the evaporation system is given in Dr. D. Tom's thesis [27]; I will only give a brief overview in this chapter. A more detailed description, describing the relevance and possible choices at each step of the deposition process, can be found in Appendix A.

The film deposition is accomplished by evaporating the constituent metals individually from metal boats which are resistively heated. In order to control the rates, a quartz crystal is mounted above each boat and shielded from the evaporant stream of the other boat. (This is important, because the quartz crystals can not distinguish between the different materials. Their operating principle is to detect a change in frequency which relates to a change in weight). The crystals are connected to Sycon[4] quartz rate monitors, which regulate the current supplied to the boats via a feedback loop. For PAC experiments, a fourth source is added, which also is resistively heated, but is shaped more like a gun or cannon in order to supply a directed stream of ^{111}In atoms at the substrate. The substrate is mounted in a ring–shaped annulus, which supplies the oxygen locally at the substrate. The amount of oxygen supplied during the deposition is regulated by a mass flow controller. A PBN heater is placed on the oxygen annulus, heating the substrate to between 550 °C and 650 °C and the annulus to a somewhat lower temperature. Because

[4] STC–200 Deposition Rate Controller: Sycon Instruments, Inc., 6757 Kinne Street, Syracuse, New York, 13057

the rates take some time to stabilize, a shutter is mounted between the substrate and the boats and is opened only after the rates are stable.

2.5 Control of Oxygen Content

In order to reliably control the oxygen content of $YBa_2Cu_3O_{7-\delta}$ films, an apparatus was built, drawing mostly on ideas provided in Refs. [11] and [12]. The basic idea in both papers is to enclose the film in a quartz tube with bulk material and keep it at certain temperatures and pressures according to the phase diagram established by Ref. [28] and reproduced in Fig. 2.1. The lines indicate the temperature and pressure required to maintain a particular values of 6+x and are later referred to as phase lines. The bulk material is used as an oxygen reservoir and helps to establish the desired value. In

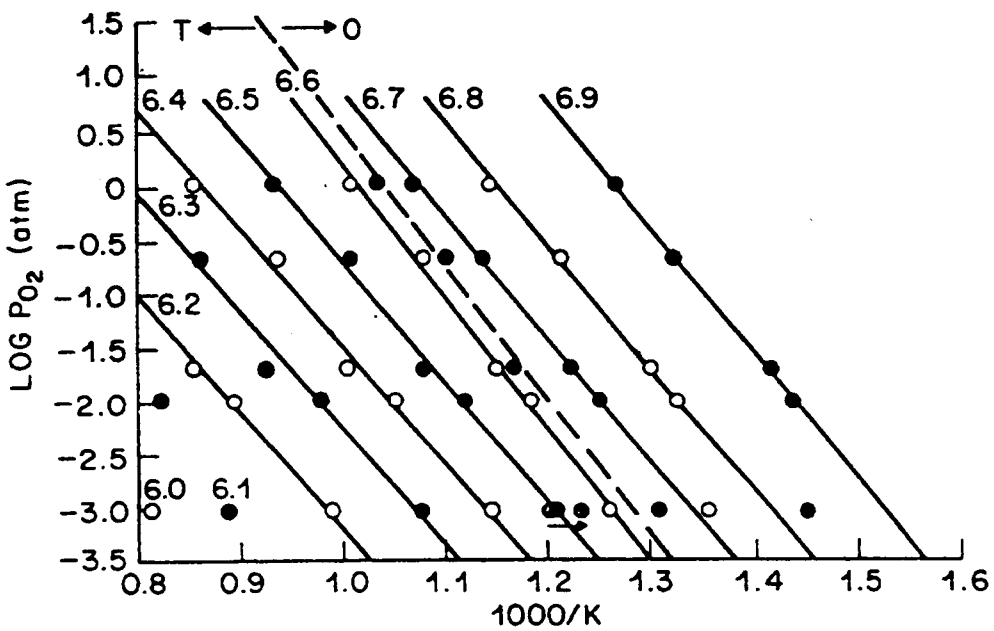

Fig. 2.1 Phase diagram used to change the oxygen content of our films. It was proposed in Ref. [28] for bulk.

addition, Ref. [11] found that if they did not have bulk material in the vicinity when they tried to achieve high oxygen deficiencies, their films decomposed completely.

Both methods start out by evacuating the quartz tube to 10^{-6} Torr. Osquiguil then backfills the tube with 10 Torr of oxygen. The anneal temperature therefore is determined by the pressure in the quartz tube and the desired oxygen content. After the system has equilibrated (the pressure stays constant), the sample is cooled down following the appropriate phase line, and eventually quenched.

In the method used by Ref. [11] the sample is heated up to 400 °C, where a rapid rise in pressure is observed when the oxygen becomes mobile. Then the valve connecting the quartz tube to the pump is closed and the sample is heated to 600 °C, where the pressure is adjusted to the value appropriate to the desired oxygen content.

2.5.1 Description of Apparatus

The main component of the system I developed in this laboratory is an 11"-long, 1/2"-diameter quartz tube, connected via a glass-to-metal seal to a stainless steel KF-flange, which in turn is connected to five-way cross. The length of this quartz tube was determined by an existing tube furnace used to heat the sample. The "sweet spot" of the mainly furnace is about 8" into the furnace. With the length chosen for the quartz tube, the glass-to-metal seal is then far enough from the furnace that the seal's integrity is not breached[5]

[5] This was shown inadvertently when the thermocouple shortened out right next to the glass-to-metal seal and therefore was reading the temperature there. Even though the furnace was red hot (>600 °C), the thermocouple was reading not more than 30 °C.

(quartz is not a good conductor of heat). Besides the quartz tube, a Pirani gauge (reading from atmosphere to 10^{-4} Torr), a K-type thermocouple feedthrough, a needle valve connected to an oxygen tank, and a Varian turbo-pumping station are connected to the cross, all with NW 40 KF-flanges. This set-up facilitates the easy loading of the films.

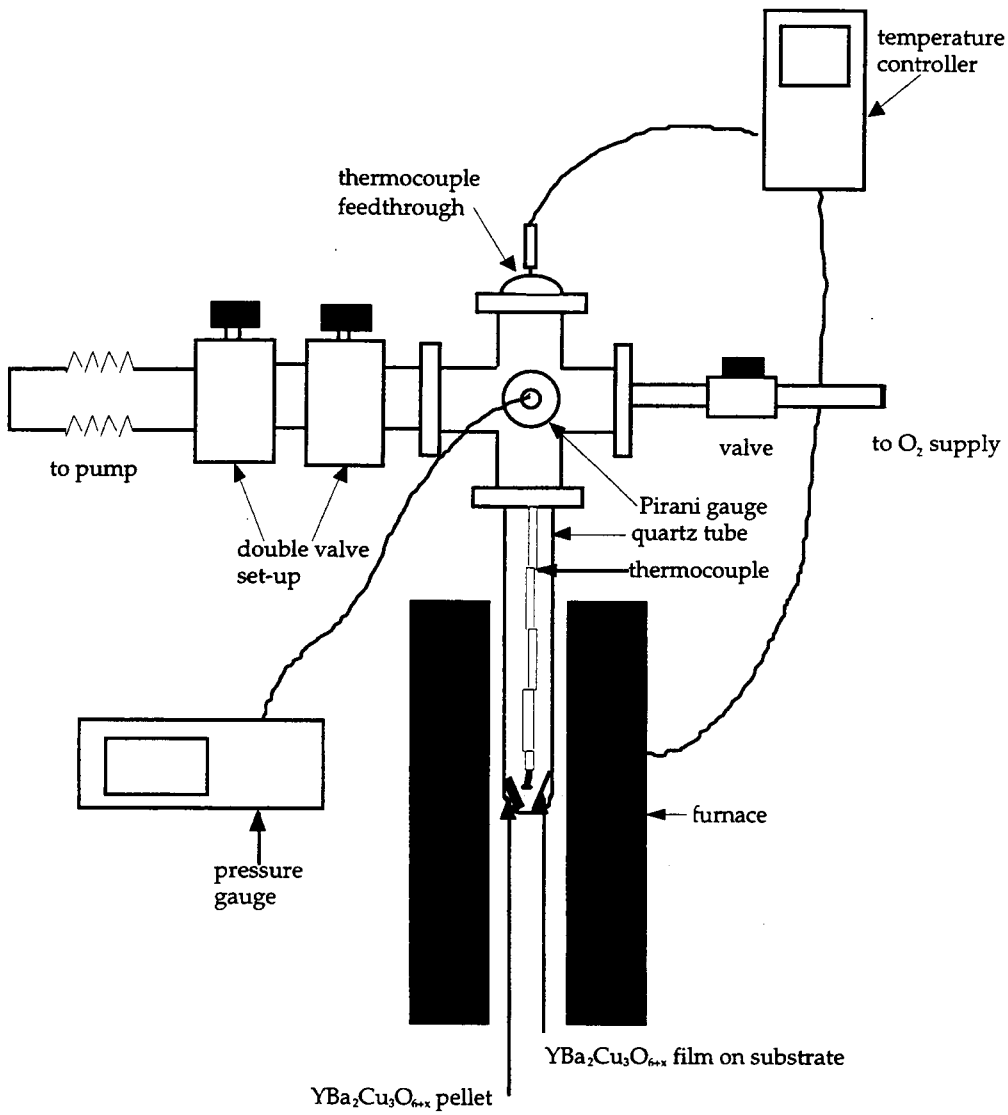

Fig. 2.2 System used to control the oxygen content

Between the pumping station and the cross are two block valves which serve the same purpose as a throttle valve by having both of them barely opened when trying to stay on a given phase line. The two–valve system allows finer control of the oxygen pressure, and with both of the valves barely opened, the one closest to the pumping station is used for the coarse regulation, while the one closest to the sample does the fine-tuning. With the two–valve set–up, a wide range of pressure changes can be regulated, from e.g. 18 torr/min needed during part of the anneal for an oxygen content of 6.7 to 0.5 mtorr/min required during part of the anneal for an oxygen content of 6.4. The cooling-rate is about 6 °C/min, determined by how fast the furnaces cools down by itself. The temperature is controlled via a type K thermocouple and a Eurotherm 808 temperature controller[6], with the tip of the thermocouple in close proximity to the film. With the current PID (P = 25, I = 12, D = 0) setting, the furnace has a stability of about -2 °C and +5 °C. The cross and quartz tube are mounted on a cart in order to facilitate quenching the film by pulling the set-up out of the furnace. Fig. 2.2 is a sketch of the system described above.

2.5.2 General Description of the Procedure

The steps to deoxygenate a film are the same, regardless of the desired final oxygen content. First a film and a pellet of $YBa_2Cu_3O_7$, pressed in Dr. Sleight's lab from powder bought from Alfa Aesar[7] are put into the quartz tube. The tube is connected to the rest of the apparatus, making sure that the

---

[6] Eurotherm Corporation, 11485 Sunset Hills Road, Reston, Virginia 22090-5286

[7] YBa_2Cu_3O powder, stock # 39534, lot # K16F14 from Alfa Aesar, 30 Bond Street, Ward Hill, Ma 01835–8099

thermocouple is right next to the sample and does not short electrically along its distance. Then the whole system is evacuated to $<10^{-5}$ torr and heated to 600 °C. The controller is set to ramp at 10 °C/min, but for temperatures lower than 250 °C, the furnace has a tendency to overshoot. During the heating, one usually (not always, if a pellet is reused) observes a rise in pressure at temperatures slightly less than 100 °C, when adsorbed water vapors start to evaporate. The pressure does not go any higher than 10^{-2} torr and goes back down to below the detection limit (10^{-4} torr) of the Pirani gauge. Because the furnace does not regulate very well for these "low" temperatures, the heating is continued. The system continues to warm, while being evacuated, till about 400 °C, when there is another rise in pressure, which can be explained by the oxygen becoming mobile and leaving the film and pellet. At this time the valve closest to the tube is quickly closed. The pressure in the system rises as the film is heated to about 600 °C (for PAC films, 550 °C was often used), as more oxygen is released from the film and pellet. After reaching 600 °C, depending on the oxygen content desired, the system either has to be backfilled carefully with oxygen or the pressure has to be equally carefully reduced. This is done by opening both valves just barely. If the system has to be backfilled, the lines are flushed with oxygen beforehand in order to ensure that only oxygen is being admitted to the system. The pressure is adjusted to the value determined by the temperature (600 °C) and the desired oxygen content. The anneal at 600 °C lasts for about 1 hour, after which the temperature and pressure are adjusted to the appropriate phase line, until the temperature is 450 °C, where it is held constant for 1 hour. The final step is cooling the system down to 400 °C, again staying on the phase line, and then quenching by quickly pulling the whole apparatus out of the furnace.

The temperature of 600 °C for the initial anneal step was chosen because it is high enough to ensure adequate oxygen mobility to reach the equilibrium, but not high enough to cause relaxation of crystallographic defects [11]. Except for film HTC 32, the higher anneal temperature for the PAC films was 550 °C, because there was evidence of a impurity site (also referred to as B site) forming in the spectra.

Quenching from 600 °C does not ensure that the film will have the desired oxygen content, because the pressure does not drop fast enough and the film might incorporate some additional oxygen. The additional step at 450 °C is therefore added to ensure that the film has the desired oxygen content. At this temperature the oxygen mobility is still high enough to ensure that the film will be in equilibrium.

The oxygen contents that can be easily achieved with this set-up and this procedure are between 6.3 and 6.7. Below 6.3 the pressures required for the 450 °C anneal are below the range of the Pirani gauge, and above 6.7 the 600 °C anneal step would require pressurizing the system above atmospheric pressure, a task it is not designed for. Anneals with a lower initial temperature have not been tried yet, but they should make it possible to obtain films with oxygen contents between 6.7 and 7.0.

Chapter 3
Characterization

3.1 Raman Spectroscopy

Raman spectroscopy is one of the techniques used to quantify the oxygen content of $YBa_2Cu_3O_{6+x}$ and determine the orientation of $YBa_2Cu_3O_{6+x}$ thin films and crystals. The basic principle behind Raman spectroscopy is the inelastic scattering of photons off phonons from the structure under investigation. The energy difference between the incoming and scattered photons excites the lattice vibrations. Because there are so many atoms in the $YBa_2Cu_3O_{6+x}$ unit cell, there are several possible excitations, the main ones used are listed in Table 3.1.

Spectra are commonly labeled by the Porto notation $z(x,x)\bar{z}$, which describes the polarization geometry. The first and last letter describe the propagation direction of the incoming and scattered photon, the letters in

frequency [cm^{-1}]	atoms responsible
118	Ba-Ba motion
145	Cu-Cu (in plane) motion
335	O(2)-O(3), out–of–phase vibration, along the c-axis
440	O(2)-O(3), in-phase vibration, along the *c*-axis
500	O(4), vibrations along the *c*-axis

Table 3.1 Raman frequencies (in cm^{-1}) for $YBa_2Cu_3O_7$. Frequencies are taken from Ref. [29].

brackets indicate the incoming and scattered polarization of the electric vector **E** [30]. x is parallel to the a-axis, y is parallel to the b-axis and z is parallel to the c-axis. Sometimes x'– and y'–axis are used, which are oriented at 45° to the x– and y–axis.

The line at 500 cm^{-1} is the most sensitive to oxygen content and is most commonly used to determine the oxygen content, based on an empirical formula [31], using the frequency $\omega(x)$ (in cm^{-1}).

$$x = 0.037\omega(x) - 11.555 \tag{3.1}$$

This line shifts approximately linearly down from 500 cm^{-1} to 475 cm^{-1} with decreasing oxygen content [29]. Thomsen *et al.* [29] also quote results from Macfarlane *et al.* [32], which differ somewhat from their own. They are in agreement about the 500 cm^{-1} line and the 145 cm^{-1} line, but for the 335 cm^{-1} line, Thomsen finds a linear change by about 10 cm^{-1}, while Macfarlane finds no change at all. For the 440 cm^{-1} line, Thomsen finds the line to change linearly with oxygen content, while Macfarlane finds that the frequency decreases with decreasing oxygen content till about 6.5 and then stays constant. They attribute the differences to sample preparations and the near-surface oxygen concentration.

As an example, Fig. 3.1 shows Raman spectra taken on c-axis oriented films deposited on $SrTiO_3$ substrates. These spectra were taken by Dr. Christian Thomsen's research group at the Technische Universität in Berlin and are of an orthorhombic and two tetragonal films from our laboratory. Features in the spectra below 340 cm^{-1} are an artifact of the filters used. The 627 cm^{-1} is strong because the excitation was done with red light and the 645 cm^{-1} and 417 cm^{-1} are consequences of this excitation and are a Froehlich–induced resonance.

Because polarized light is used and only certain polarizations excite certain vibrations, this method can also be used to determine the orientation of the film. Thomsen *et al.* [33] developed a method to determine the epitaxy of *c*-axis oriented films, Dieckmann *et al.* [30] expanded upon it and used it for both *a*-axis and *c*-axis oriented films.

Gibson *et al.* [34] and Cohen *et al.* [35] showed that the 500 cm^{-1} line as well as the 115 cm^{-1} line and an additional line at 585 cm^{-1} yield some information about cation disorder in this films. The frequency of the 115 cm^{-1} decreases with increasing disorder and the intensity of the 585 cm^{-1} line (normalized to the 340 cm^{-1}) is larger for higher disorder. They also found that with increasing disorder the frequency of the 500 cm^{-1} line decreases, which can lead to too low an estimate for the oxygen content. On the other hand, Martínez *et al.* [16] found a shift to higher frequencies for some of films and attributed it to departures from the cation stoichiometry. This again shows that in thin films, several factors contribute to changes in a certain quantity and it might not always be possible to determine the particular factors in any given case.

Furthermore, Raman spectroscopy can be used to find impurities, at least within the penetration depth of the light used. $BaCuO_2$, Y_2BaCuO_5, $Y_2Cu_2O_5$, Y_2O_3, BaO and CuO are the most commonly found impurities, and Ref. [29] gives a list of references for the Raman spectra of the impurities.

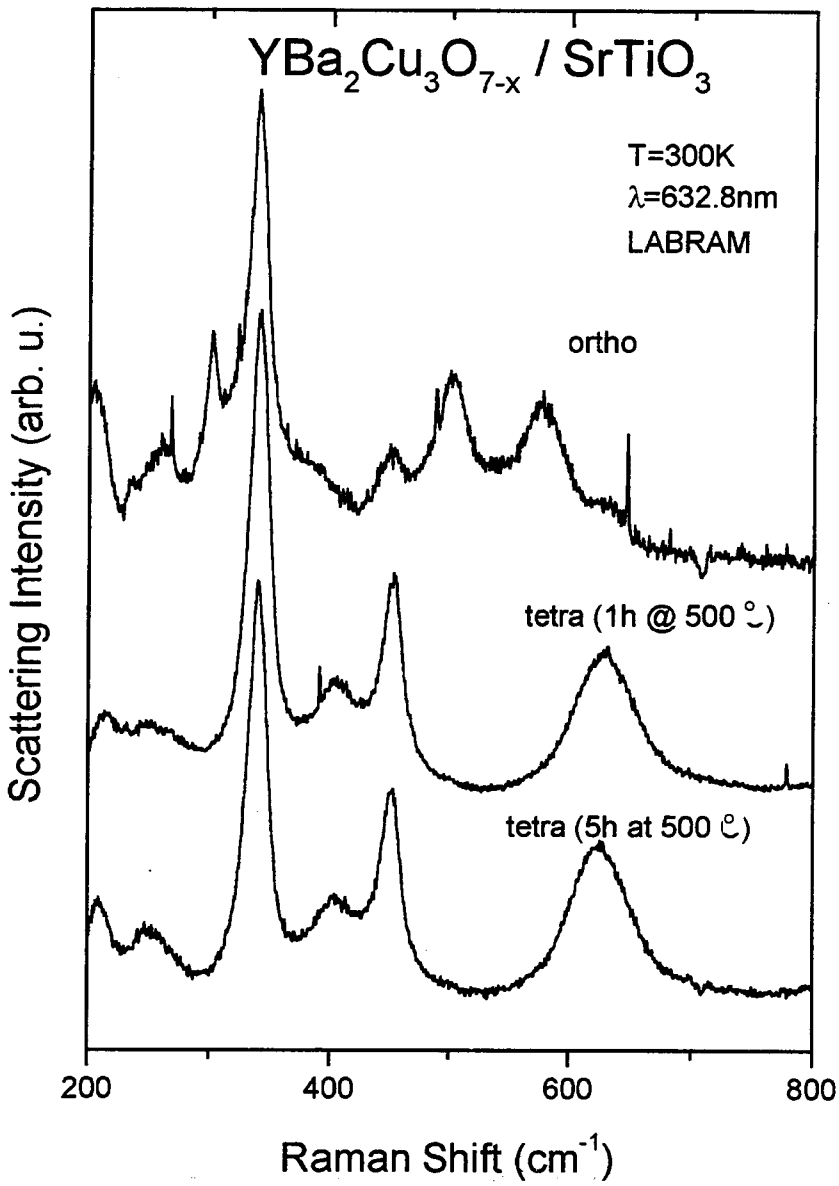

Fig. 3.1 Raman spectra taken on an orthorhombic film and two tetragonal films subjected to different anneals. The differences between the orthorhombic and tetragonal films are very obvious, but the differences between the two different anneals for the tetragonal films do not show up in the Raman spectra. The orthorhombic film was determined to be fully oygenated, and the tetragonal films have an oxygen content of 6.25 (±0.15). The data was taken by Prof. Thomsen's research group at the Technische Universität in Berlin.

3.2 Rutherford Backscattering

Rutherford's famous expression for the elastic scattering of charged particles is the basis of the technique of Rutherford backscattering (RBS) which is used to determine the composition of materials. It can also give information about thickness, crystallinity, and homogeneity of films under certain conditions. A brief overview follows, that extracts the most important points from [36].

In a nutshell, RBS is the shooting of a charged projectile of known energy at a target and the measurement of its energy after the scattering. Because the energies chosen are small enough that nuclear forces are not important, the interaction is considered entirely Coulombic.

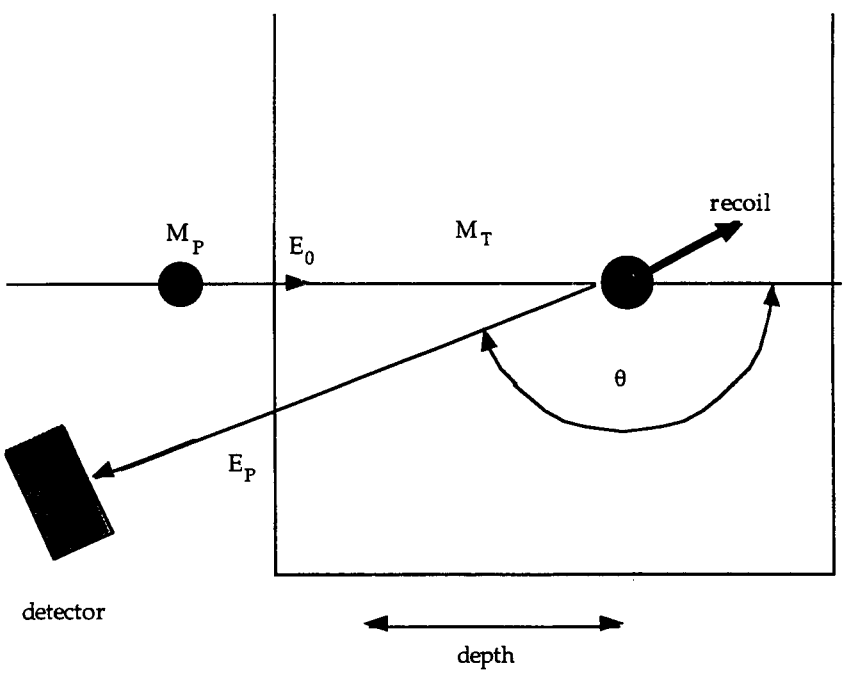

Fig. 3.2 Typical Rutherford Backscattering setup.

The kinematic factor K is defined as the ratio of the energy of the projectile after the scattering (E_P) to the energy before the scattering E_0 and using energy and momentum conservation:

$$K = \frac{E_P}{E_0} = \left[\frac{\sqrt{1-\left[(M_P/M_T)\sin\theta\right]^2} + (M_P/M_T)\cos\theta}{1+(M_P/M_T)} \right]^2 \tag{3.2}$$

It depends only on the ratio of the masses of the projectile (M_P) and the target (M_T) and the scattering angle.

From an experimenter's point of view, the more energy that is lost by the projectile during the scattering the better, because that makes it easier to measure and identify the projectile after the scattering. For a given E_0, this means that K should be as small as possible. Leaving the masses fixed, K is the smallest for $\theta = 180°$, hence the term "backscattering". In reality, the detector cannot be placed at 180°, because that would put it into the path of the incident beam (see also Fig. 3.2), but it is placed at least 170°, or a detector in the shape of a ring is used.

If two nuclei scatter from each other by the Coulomb interaction (and $M_P << M_T$) the differential cross section is:

$$\frac{d\sigma}{d\Omega} = \left(\frac{Z_P Z_T e^2}{16\pi\varepsilon_0 E} \right)^2 \frac{1}{\sin^4(\theta/2)} \tag{3.3}$$

The scattering cross section depends strongly on the atomic number Z of the material under investigation and hence serves as a means to differentiate between the different elements that comprise a material.

If a particle scatters in a depth x, with α_1 and α_2 the angles of the incident and scattered particle beams with the surface, the energy loss is

$$\Delta E = \left[\frac{K}{\sin\alpha_1} \left.\frac{dE}{dx}\right|_{E_0} + \frac{1}{\sin\alpha_2} \left.\frac{dE}{dx}\right|_{KE_0} \right] \cdot x \tag{3.4}$$

which means that from the energy attenuation dE/dx in the material one can calculate the thickness of the film. There is a linear relationship between the energy loss and the thickness. Points in an energy range Δ corresponds to scattering events from a layer of thickness Δx. Fig. 3.3 exemplifies this relationship. RBS data usually is taken by counting the number of backscattered particles at an energy $E_P(i)$ and within an energy interval Δ (given by the energy resolution of the detector) and sorting it in different bins with i being the channel index. In the case of perpendicular incidence of the projectile ($\alpha_1 = 90°$) and perfect back-scattering ($\theta = \alpha_1+\alpha_2 = 180°$), the above equation reduces to

$$\Delta E = \left[K\frac{dE}{dx}\Big|_{E_0} + \frac{dE}{dx}\Big|_{KE_0} \right] d \tag{3.5}$$

Therefore, by measuring ΔE, one can measure the thickness of the film or layer under question.

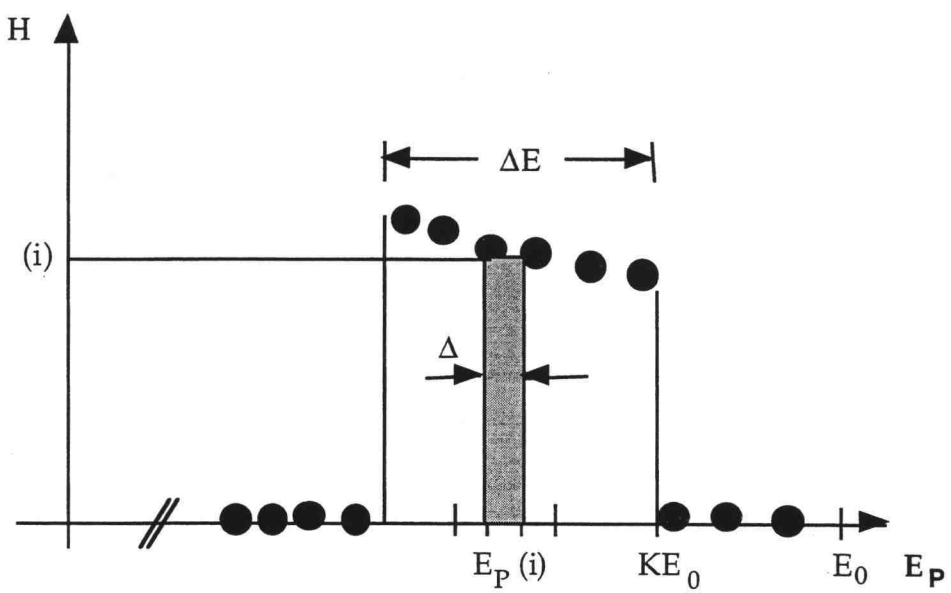

Fig. 3.3 Sample histogram of a thin self-supporting film

Because the kinematic factor K depends on the mass of the target, if a material contains several different kind of atoms, the leading edges will be at different energies, which makes the identification of different materials possible, unless the atomic numbers are too close for the energy resolution of the detector. The thinner the material, the better separated are the peaks from different kind of atoms.

Additional information can be gained by integrating the area under the curve. Starting from

$$H(i) = \frac{\mathrm{d}I}{\mathrm{d}\Omega}\Delta\Omega t_0 = \left.\frac{\mathrm{d}\sigma}{\mathrm{d}\Omega}\right|_{E(x_i)} I\frac{N_i}{A}\Delta\Omega t_0 \tag{3.6}$$

one can calculate the area F under the curve and find the following equation:

$$F = I_0\Delta\Omega t_0 nd\left.\frac{\mathrm{d}\sigma}{\mathrm{d}\Omega}\right|_{E_0} \tag{3.7}$$

with I_0 the beam intensity, t_0 the measuring time, $\Delta\Omega$ the detector solid angle and n the target particle density. The thickness can therefore be calculated if all the terms in the equation are known.

Additional information about the stoichiometry can also be gained from the above equation. One can get absolute stoichiometry (at least within a factor of d) because all the terms in equation (3.7) except nd are known. By forming the ratio for two kinds of atoms, most of the factors cancel and one is left with terms relevant to the different kind of atoms, e. g. taking atom 1 and atom 2

$$\frac{F_1}{F_2} = \frac{n_1}{n_2}\left(\frac{Z_1}{Z_2}\right)^2 \tag{3.8}$$

This formula gives only ratios, and in order to get absolute number, the additional condition for $YBa_2Cu_3O_{6+x}$ is imposed that the cations have to add up to 6.

Our RBS analyses are performed at the University of Arizona by Professor L. C. McIntyre. The α–particles used are accelerated to 2 – 4 MeV, and the detector is positioned at θ = 170°. With this set-up, an accuracy of 1% on the relative stoichiometry and 3% on the absolute stoichiometry can be achieved – if the peaks are separated. This requires a thin film (≤ 2000Å for $YBa_2Cu_3O_{7-\delta}$) on a low–Z substrate like MgO. RBS showed that our best films tend to be copper–rich.

In Rutherford backscattering, a phenomenon known as channeling can be used to gain structural information. Due to the periodicity of a lattice, a charged particle can experience many small glancing collisions and be guided deep into the crystal along atomic rows or atomic planes (channels). The better the crystallinity of the material under investigation, the deeper the charged particles will penetrate the sample and the fewer will be detected in a detector set up for Rutherford backscattering. χ_{min}, the ratio between the yield for a random spectrum and an aligned spectrum, for our films are about 20 – 50 %, which is large compared to 3 – 8 % for very good films. Ito *et al.* [37] used channeling to investigate *a*-axis films of different thickness and found that the χ_{min} value increased with increasing film thickness, indicating strain relaxation along the *c*-axis, which, for *a*-axis films, is in the substrate plane. Another application of channeling is probing the orientation of our films relative to the substrates and it has been found that the MgO substrate normal and the film normal are misaligned by ≈ 1°.

3.3 The Transition Temperature

In order to measure T_c, the critical temperature at which the resistance of a superconductor drops below the noise level, a four-probe measurement is

used. The design of the probe has been described extensively in Dr. D. Tom's thesis; I will give just a quick summary.

The sample is mounted on a copper block with the help of four Be-Cu wires, which are bent to act as springs. These wires keep the sample in place and also provide the electrical contact with the outer two supplying a current, and the inner two measuring the voltage. This 4–terminal measurement eliminates lead and contact resistance. The copper block houses a Pt resistance thermometer. The temperature is measured by monitoring its resistance, which decreases linearly with decreasing temperature over the range 30 K to about 500 K. With the help of the calibration curve, the resistance is translated into a temperature. The range of a Pt thermometer can be extended up to 800 K and down to about 14 K; for temperatures lower than that it becomes insensitive to temperature changes. The copper block is used to ensure that the thermometer is at the same temperature as the sample and that the sample temperature is uniform[8].

This whole unit is mounted in 1–inch stainless steel tube and covered with a copper shield. The shield is used to protect the sample from refrigerant splashing. With different adapters, the probe can either be mounted in a dewar and used with liquid nitrogen, or it can be used on a transport dewar filled with liquid helium. In both cases, the temperature is changed by making use of the temperature gradient between the outside and the boiling refrigerant.

The measurement is controlled by a computer program written in LabVIEW™ [9]. The sample voltage is measured twice, first with the current in

[8]A good example for that is seen during the warm-up of the probe after a measurement has been taken. As soon as the probe is exposed to air, it frosts over. During the warm-up, the frost on the copper-block melts all at once, very differently from the frost melting on the rest of the probe.

[9] LabVIEW™ is a trademark of National Instruments Corporation.

one direction, then in the other. The two voltages are subtracted to eliminate thermal voltages[10] and then divided by two. Then the resistance is calculated according to R=U/I. At the same time, the temperature is measured twice and averaged, to compensate for any cooling of the sample during the two voltage measurements.

A good measurement yields a very smooth curve with instrument–limited noise, which means that for a good *c*-axis oriented, orthorhombic $YBa_2Cu_3O_7$ film with decreasing temperature the resistance has to decrease for each data point. Noisy data are an indication of some form of trouble, usually not with the sample, but rather with the contacts as can be seen in Fig. 3.4, which shows data for a film, where the contacts became faulty around 90 K. Even the data for higher temperatures is not as smooth as it should be for a good T_c measurement. Measuring the resistance across any of two pairs of contacts with the sample in place should give about the same resistance for all the different pairs. If one contact gives a significantly higher resistance than the others (by comparing the different pairs of wires), one can try to carefully bend the wire to give it more tension, but very often one has to resolder the wire.

The high resistance is an indication that the wire is barely making contact with the sample surface, and that it is very susceptible to mechanical disturbances, like moving the sample further into the dewar. This shows up as large changes in the resistance and random readings if the contact is lost altogether. Sometimes these measurements can be used to get a rough feel for where the transition temperature is, but they cannot be used for much more.

---

[10] From the first measurement, one gets $U_{sample} + U_{thermal}$, the second measurement yields $-U_{sample} + U_{thermal}$, because the thermal voltage does not change with the reversal in current. Taking the difference $U_{sample} + U_{thermal} - (-U_{sample} + U_{thermal}) = 2U_{sample}$.

Much information can be gained from the resistance measurements. Most important are the transition temperature, where the resistance drops below the noise level, and the width of the transition, which gives an indication of homogeneity. Information about the nature of the carriers and the normal state can be obtained from the general shape of the transition curve, but we never explored that venue.

For a good orthorhombic film, the transition should be > 90 K with a width of ≤ 0.5 K. In addition, the general shape should be decreasing linearly with temperature and extrapolate to zero like a metal, which leads to a ratio of R(300 K)/R(100 K) ≈ 3. Because most of my research was concerned with films deliberately deposited under non-ideal conditions, most of the curves I took did not have this shape. This is especially evident in the case of the *a*-axis films' R(T) curves, which in most cases are almost flat with decreasing temperature. They do not have the slope of 3 required for a good metallic film and in many cases show a slight increase just before going through the

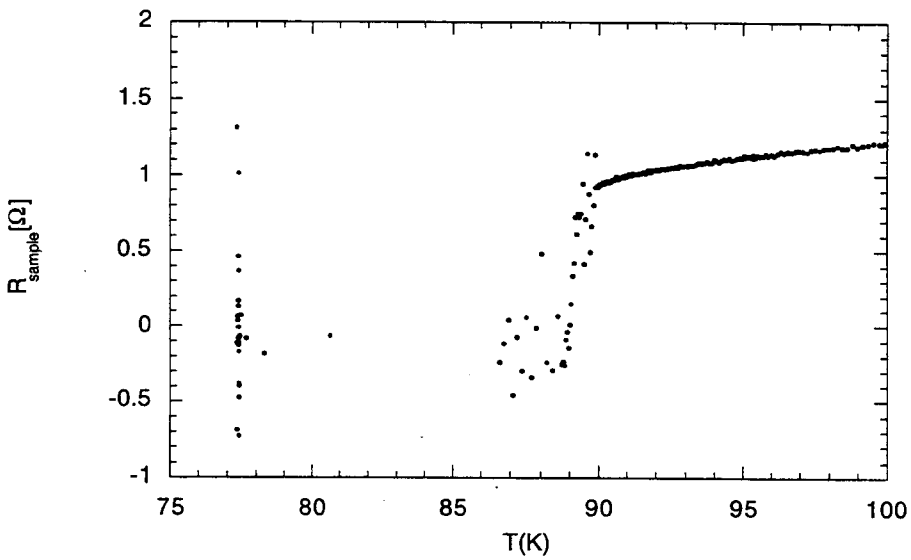

Fig. 3.4 Example of a R(T) –curve, where contacts became faulty around 90 K.

transition. Fig. 5.6 is an example of a *c*-axis film (though not optimal) and an *a*-axis film which clearly shows the difference in shape and is an example of a good T_c measurement, compared to the example in Fig. 3.4.

Transition temperature measurements are a strange hybrid, neither a bulk characterization nor a truly local characterization technique. Because a continuous, macroscopic path between the contacts is required, it is not a local technique, but because only a single path out of the multitude possible is necessary, it is not a true bulk technique like AC susceptibility, where the whole sample contributes to the signal.

3.4 X-Ray Diffraction

X-ray diffraction is one of the main tools I used to characterize my films and it is very widely used in thin film science in general. It is used to gain information about the structure and the orientation of films. It can also be used to get information about disorder, but x-ray diffraction's forte is the investigation of order, which means it can tell us only about small deviations from order.

There are two different descriptions of x-ray diffraction, one associated with Bragg, the other with von Laue; Ref. [38] show the equivalence of these two points of view quite nicely. Both descriptions consider elastic x-ray scattering (the wavelength does not change in the case of the Bragg condition or $|\mathbf{k}|=|\mathbf{k}'|$ when using the von Laue condition). This scattering is from a periodic lattice and therefore when the x-rays interfere constructively, a peak in the scattering intensity is observed. The difference between the two descriptions is how the source of the scattering is described.

In order to derive the Bragg condition, it is helpful to look at a typical set-up as illustrated in Fig. 3.5. Within the crystal, we can define an imaginary set of planes, some distance d apart, which diffract the incident x-ray beam. These planes can be identified by Miller indices, h, k, and l. The angle of incidence is assumed to be the same as the angle of reflection. In order to observe a peak, the x-rays diffracted from all the planes in the crystal have to interfere constructively, namely the path difference between two successive planes has to be an integral multiple of the wavelength, which leads to the Bragg-condition:

$$n\lambda = 2d\sin\theta \tag{3.9}$$

It is important to note that even though Fig. 3.5 looks like the incident beams are diffracting off atoms, the dots are representations of the unit cell

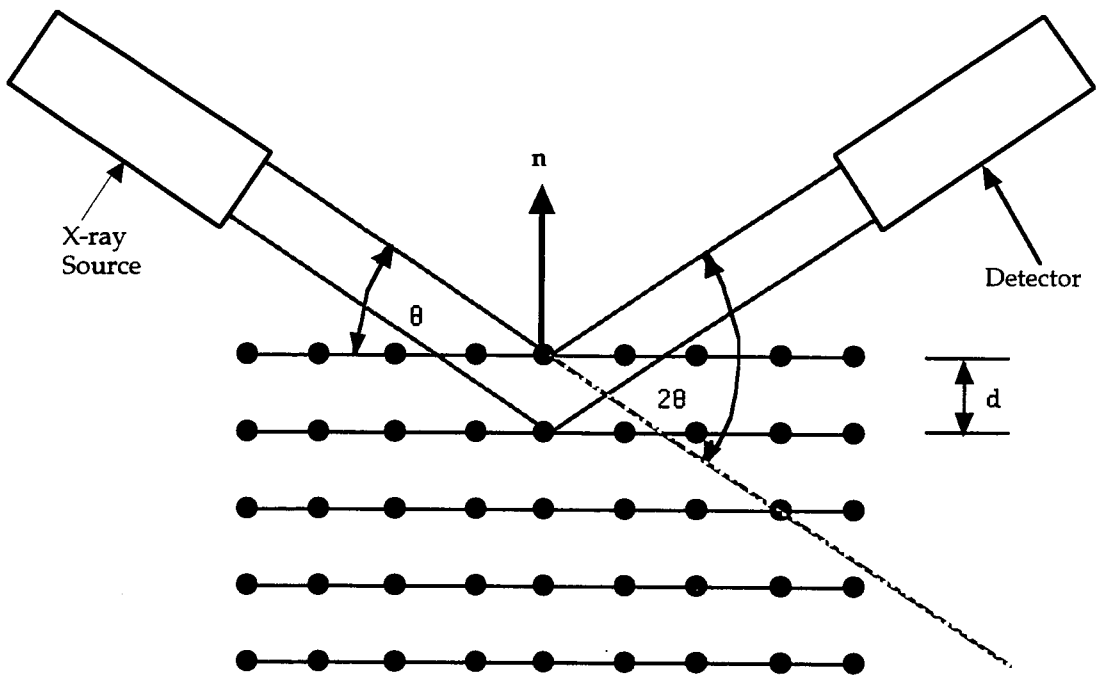

Fig. 3.5 X-ray diffraction in Θ–2Θ mode (Bragg–Brentano geometry). The source moves through Θ, while the detector moves through 2Θ. (More commonly, the source is fixed and the sample and detector move to maintain to maintain the Θ–2Θ relationship.

and can have many atoms associated with them, as in the case of $YBa_2Cu_3O_{6+x}$, where each dot represents 12 to 13 atoms, depending on the oxygen content.

In the von Laue description, the crystal is regarded as composed of identical scatterers (sets of ions or atoms), placed at the sites **R** of a Bravais lattice. Each can reradiate the incident radiation in all directions. To derive the von Laue condition for constructive interference of scattered radiation, we consider Fig. 3.6 which shows the scattering from two points of the Bravais lattice, separated by *d*. The condition for constructive interference, when the path difference is equal to an integral number of wavelengths, is

$$\mathbf{d} \bullet (\hat{\mathbf{n}} - \hat{\mathbf{n}}') = m\lambda \tag{3.10}$$

Multiplying the above equation by $2\pi/\lambda$ to get from the unit direction vectors to the wave vectors, and realizing that all **d** are vectors of the Bravais lattice, one obtains the following equation

$$\mathbf{R} \bullet (\mathbf{k} - \mathbf{k}') = 2\pi m. \tag{3.11}$$

In words, constructive interference will occur if the change in wave vector **k**-**k'** is a vector of the reciprocal lattice.

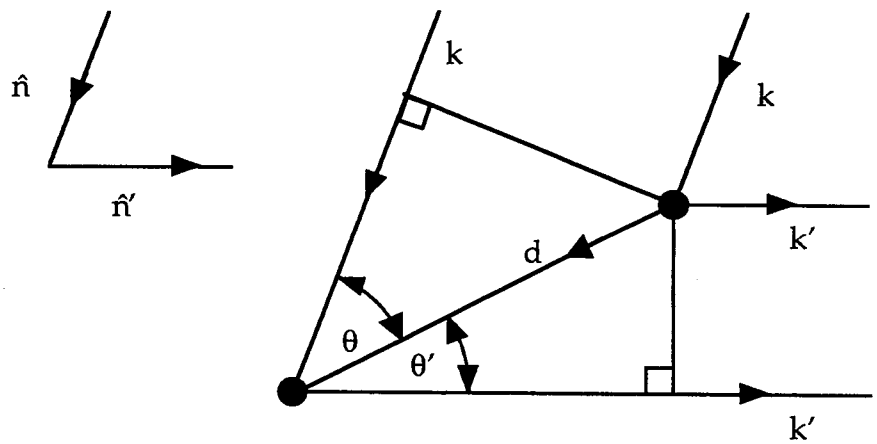

Fig. 3.6 The path difference between rays scattered from two points of a Bravais lattice is $\mathbf{d} \bullet (\hat{\mathbf{n}} - \hat{\mathbf{n}}')$

The von Laue description is mainly used when dealing with single crystals, because it provides an easy way to test which peaks can be expected in a diffraction spectrum, depending on the (range of) wavelength (white x-ray light or one particular line) used and the orientation of the crystal with respect to the incident radiation. When working with powder samples, where all different orientations are present, using the Bragg condition is the easiest and most intuitive.

To investigate what influences the x-ray spectrum and therefore provides additional information, it is best to start with an infinite crystal. The Bragg condition defines where it is possible to expect peaks.

In this case, there is a path difference of an integer multiple of λ between the beams diffracted off the different planes. If the angle is slightly different from a Bragg angle, there is always a plane somewhere in the infinite crystal, which has a path difference of exactly $\lambda/2$ from the plane under consideration, .and so the diffracted beams from these two planes will cancel each other. Therefore, in a perfect infinite crystal, one finds infinitely sharp peaks.

Real crystals are not infinite, and diffraction peaks consequently broaden, because of the absence of planes to complete the destructive interference for the off-resonance condition. This is best illustrated by an example. Imagine a crystal having 1000 diffracting planes. Suppose for an angle θ, the beams diffracted from the 1^{st} and 601^{st} plane cancel each other. Then the same will happen with #2 and #602, and so on all the way up to #400 and #1000. Beams diffracted off the planes #401 to #600, on the other hand, will not destructively interfere and therefore will contribute to the detected intensity. In an infinite crystal, there still would have been another

plane to destructively interfere with. A rigorous treatment results in the Scherrer formula [39]

$$B = \frac{0.9\lambda}{t\cos\theta_B} \tag{3.12}$$

B gives the breadth (above instrumental broadening) of the curve in 2θ and is defined as the width at half maximum of the peak[11], t is the thickness of the sample (or more precisely the thickness of the crystallites) and θ_B is the angle for the Bragg reflection. For a typical film thickness of 2000 Å, this leads to a broadening of the (005) peak at $2\theta = 38.42°$ by 0.042°. The broadening becomes more important with increasing θ_B or decreasing thickness, as shown in Fig. 3.7. This is well below the experimental values of the FWHM of our films.

There are other peak-broadening mechanisms. No x-ray beam is truly monochromatic; the K_α line has a linewidth of about 0.001Å. For $\lambda = 1.5$Å, and $\theta = 45°$, this broadens the line by 0.08°. In addition, no real x-ray beam is truly parallel, which was an assumption in the original derivation. Strain in the film can cause the peaks to broaden, because it induces variations in the lattice parameter. Differentiating Bragg's law with respect to θ, one obtains

$$\Delta\theta = -\frac{\Delta d}{d}\tan\theta \tag{3.13}$$

which shows the broadening of the peaks with respect to a variation in lattice parameter. Since tan θ approaches infinity as θ approaches 90°, the influence on the peak width can be rather marked, which Fig. 3.8 also illustrates.

[11] Also referred to as FWHM: Full Width Half Maximum

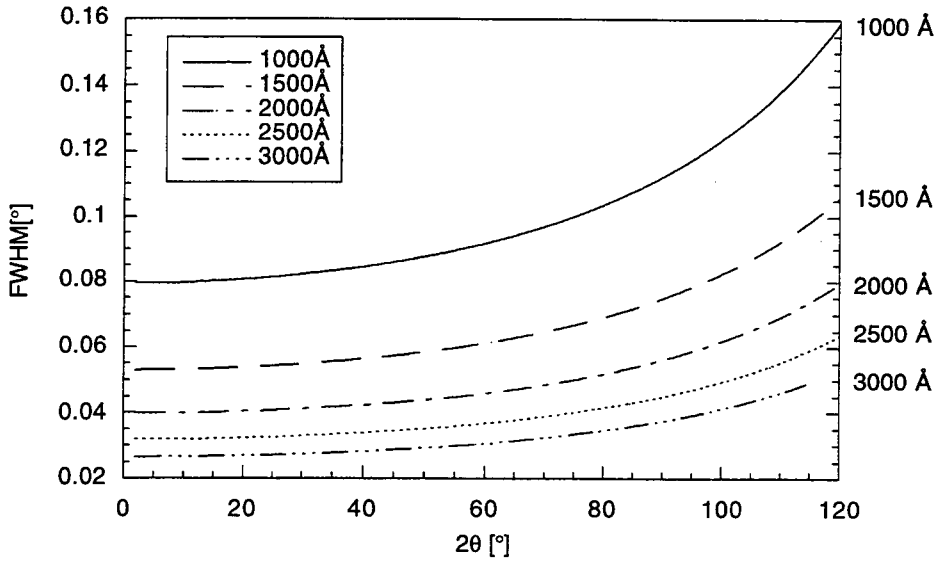

Fig. 3.7 Influence of the film thickness on the broadening of diffraction peaks at different angles. The wavelength of Cu K_α (1.54 Å) was used for the calculation.

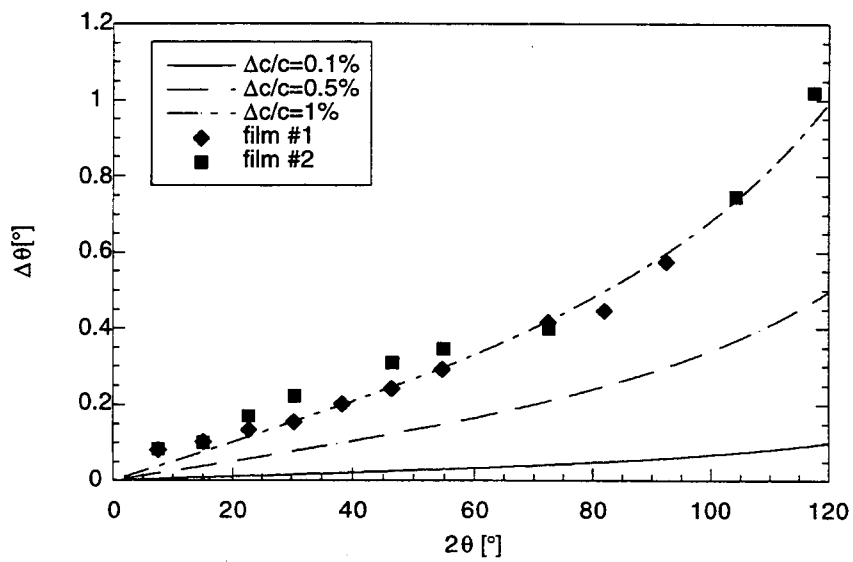

Fig. 3.8 Influence of a variation in the lattice parameter on the peak width. $\Delta c/c=1\%$ is a variation in lattice parameter of ≈0.1Å, $\Delta c/c=0.5\%$ yields ≈0.06Å and $\Delta c/c=0.1\%$ yields 0.01Å for a lattice parameter of 11.7Å. Film #1 was deposited on a MgO substrate with small substrate peaks, film #2 was deposited on a MgO substrate with strong substrate peaks. The (008) peaks are missing, because the peaks are too small to fit reliably.

Fig. 3.8 also has some data from films deposited in this laboratory. The two films chosen are "standard" films, except that film #1 was deposited on a MgO substrate with small substrate peak, possibly indicating an old substrate that formed an amorphous surface layer, and film #2 was deposited on a MgO substrate with strong substrate peaks. Fig. 3.8 in conjunction with Fig. 3.7 shows clearly that the main factor responsible for the broadening of the film peak are variations in the lattice parameter, resulting from strain in the film. As [40] pointed out, this result is not as undesirable as it might sound, because there is a 9% lattice mismatch between $YBa_2Cu_3O_{6+x}$ and MgO and the adjustment of the lattice parameter is evident in the line broadening and shows that there is a semi–coherent interface between the film and the substrate.

There is additional information to be obtained from the differences in intensities of the Bragg reflections, including the case where the intensity is zero (even though the reflection is allowed according to Bragg's law).

To explain this, we have to put the atoms back into the unit cell. The phase difference for a wave scattered from an atom at the origin and that scattered from an atom at the point B with the coordinates (x,y,z) or the fractional coordinates ($u=x/a$, $v=y/b$, and $w=z/c$) for the hkl reflection can be written as

$$\phi=2\pi(hu+kv+lw) \tag{3.14}$$

Using the complex notation for describing waves, the amplitude of the scattered wave can be written as

$$Ae^{i\phi} = fe^{2\pi i(hu+kv+lw)} \tag{3.15}$$

where f is the atomic structure factor and gives a measure of how efficiently the atom scatters the incoming beam. It depends on the wavelength of

radiation used, the atom, and the angle of detection [41]. The atomic structure factors are tabulated in Cullity [42].

The resultant wave is obtained by summing the above equation over all the individual atoms in the unit cell at their respective positions. If a unit cell contains atoms 1, 2,... N, each having fractional coordinates $u_1\ v_1\ w_1$, $u_2\ v_2\ w_2$, $u_3\ v_3\ w_3$,... and individual atomic scattering factors f_1, f_2, f_3,.. then the structure factor F for the hkl reflection will be:

$$F = f_1 e^{2\pi i(hu_1+kv_1+lw_1)} + f_2 e^{2\pi i(hu_2+kv_2+lw_2)} + f_3 e^{2\pi i(hu_3+kv_3+lw_3)} + \ldots \qquad (3.16)$$

The measured intensity is given by $|F|^2$. Because of the exponential, which can take positive and negative values (and complex values), the diffracted beams from different atoms can cancel each other. One example is a body-centered cell with only one kind of atom, where one finds that for $h+k+l$ even, $F = 2f$ but for $h+k+l$ odd, F is zero. This means that even though these reflections are allowed according to Bragg's law, they are not in the X-ray spectrum. Noting which reflections are missing helps identify the different structures within the cubic system. If there are different kinds of atoms in the unit cell, reflections which might cancel each other in a unit cell with only one kind of atom, might not cancel completely, but still the amplitudes will be reduced due to the different atomic structure factors.

There are several additional factors which influence the intensities, like absorption, multiplicity, temperature effects, some of which depend on the type of sample or the method used and which are discussed in any basic text-book on this subject, e.g. Cullity [42].

In summary, the position of the Bragg reflections and possibly missing reflections gives very basic structural information about the unit cell. Relative intensities yield information about the atoms in the unit cell, and are used in refinement techniques to learn about the atomic structure by

modeling the structure, calculating the intensities and comparing them to measured intensities. The width of the peak is influenced by imperfections like finite crystal size, variations in lattice parameter, caused by strain and several other possible factors.

No thin film is a true single crystal, but is composed of individual grains. To gain information about the alignment of the grains, rocking curves and ϕ-scans are used.

For a rocking curve, the detector is set at an angle 2θ that satisfies the Bragg condition, and locked in position. The sample is then rotated ("rocked") through θ, keeping its normal in the source–detector plane. This brings crystallites whose normal to the diffracting plane does not bisect the incoming and reflected beam in the standard θ–2θ set-up into the diffraction condition. In oriented film samples, the width of a rocking curve is a measure of how well aligned the different grains of the film are with respect to the normal of the film surface.

To determine the in-plane alignment, ϕ-scans are used [43]. In a θ-2θ scan, only planes parallel to the sample surface can be detected. If the sample

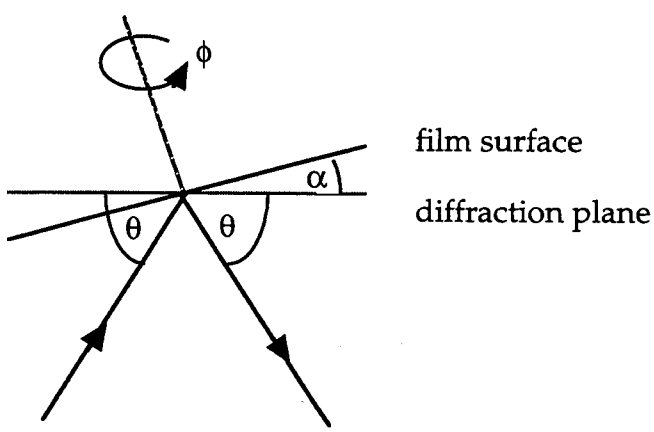

Fig. 3.9 Schematic diagram of Field-Merchant method to determine in–plane alignment of textured samples.

is tilted relative to the x-ray beam as in Fig. 3.9, other peaks can be detected. If for example a film is tilted by α=56.8° (the interplanar angle between the $YBa_2Cu_3O_7$ (102) and (001) orientations) and 2θ is set to 32.5° (calculated from (102) lattice spacing), by rotating the sample around the ϕ-axis, the diffraction signal will be detectable only if an *a*-axis oriented grain is parallel to the plane of incidence of the diffracted x-ray. A plot of ϕ versus the diffracted intensity provides a measure of the distribution of grain orientations in the film sample. Zheng *et al.* [44] show that for $SrTiO_3$ and $LaAlO_3$, the *a*-axis aligns with the (100) orientation of the substrate, but for MgO, 4% of the grains are aligned along the (110) direction and in the case of YSZ 66% of the grains are aligned along the (110) direction. These results are explained by lattice mismatch, for MgO the mismatch in the (100) direction is ≈8%, in the (110) direction ≈50%, but if one considers the $YBa_2Cu_3O_{7-\delta}$ [300] and the MgO [220] directions, the mismatch becomes only 1.8%.

3.4.1 Interpretation of X-Ray Data

The x-ray data is taken on a Siemens D5000 powder diffractometer with a Kevex Si(Li) detector. It is used as a θ-2θ diffractometer, with the added capability of taking rocking–curves. The spectrometer is set at a current of 30 mA and an accelerating voltage of 50 kV. Appendix B gives the typical settings of the programs used to investigate the films.

Before any data concerning the film can be extracted from the recorded spectra, one has to identify which peaks are related to the substrate and which are film related. Table 3.2 gives the expected 2θ positions of the peaks for *c*-axis oriented $YBa_2Cu_3O_{7-\delta}$ films and Table 3.3 does the same for the substrates used in this investigation: MgO, $LaAlO_3$ and $SrTiO_3$. Because the substrate

contains so much oriented material, the substrate peaks are far stronger than any of the film peaks. This causes several problems.

One problem is that the strong substrate peaks usually cause the detector to overload. A peculiarity of the diffraction system used is the fact that in that case it sets the data to zero as it can be seen in Fig. 3.10. (Because the detector can be used to determine the energy of incoming photons, it rejects two photons which come in too close to each other and would give a

Reflection (00*l*)	2 θ [°] (c=11.68 Å)	2 θ [°] (c=11.81 Å)
(001)	7.56	7.48
(002)	15.15	14.99
(003)	22.81	22.56
(004)	30.58	30.23
(005)	38.49	38.05
(006)	46.6	46.06
(007)	54.96	54.31
(008)	63.66	62.88
(009)	72.79	71.86
(0010)	82.48	81.38
(0011)	92.97	91.65
(0012)	104.58	102.96
(0013)	117.97	115.9

Table 3.2 The expected θ-2θ values for *c*-axis oriented $YBa_2Cu_3O_{6+x}$. The left column is for fully oxygenated material, while the right column is taken from a powder with an oxygen content of 6.09 [5].

	MgO	$SrTiO_3$	$LaAlO_3$
(100)		22.74	23.44
(200)	42.91	46.45	47.95
(300)		72.53	75.11
(400)	94.04	104.13	108.71

Table 3.3 Expected 2θ values in ° for the substrates used in this thesis. MgO is face centered cubic and does not have (100) and (300) reflections.

wrong energy. As a consequence, for part of the substrate peaks the detector rejects all of the incoming photons.) The next several datapoints after the overflow do not represent real data either. This means that the substrate peaks can be used only to give a rough indication of the quality of the substrate: if there are strong substrate peaks the sample is well oriented. The reverse is not quite true. Small substrate peaks can indicate a "bad" substrate, especially in the case of MgO, which can form an amorphous surface layer if exposed to water vapor. But they might also indicate that the substrate changer did not pick up the sample correctly or that the sample was not mounted properly in the substrate holder. Fig. 3.12 illustrates this point very clearly. First the low intensity spectrum was recorded, then the same sample was run again, without ever touching or remounting it. The only thing that touched the sample holder was the sample changer, which picks up the sample from the loader and puts it into the beam. With low intensity spectra, the first order of business is to rerun the sample; if that does not help, then remount the sample. The last step would be running a rocking curve on the substrate peaks. If the substrate peaks are still small, it is almost certainly an indication that the substrate is of bad quality.

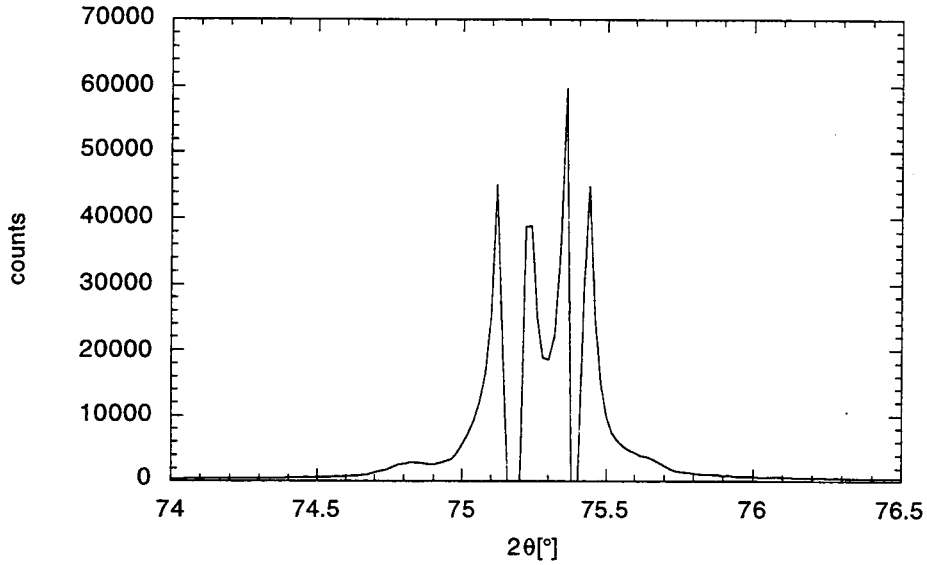

Fig. 3.10 Overloading of the dectector due to intensely diffracting substrate peaks. This data was taken on $LaAlO_3$, but the same behavior occurs for MgO and $SrTiO_3$.

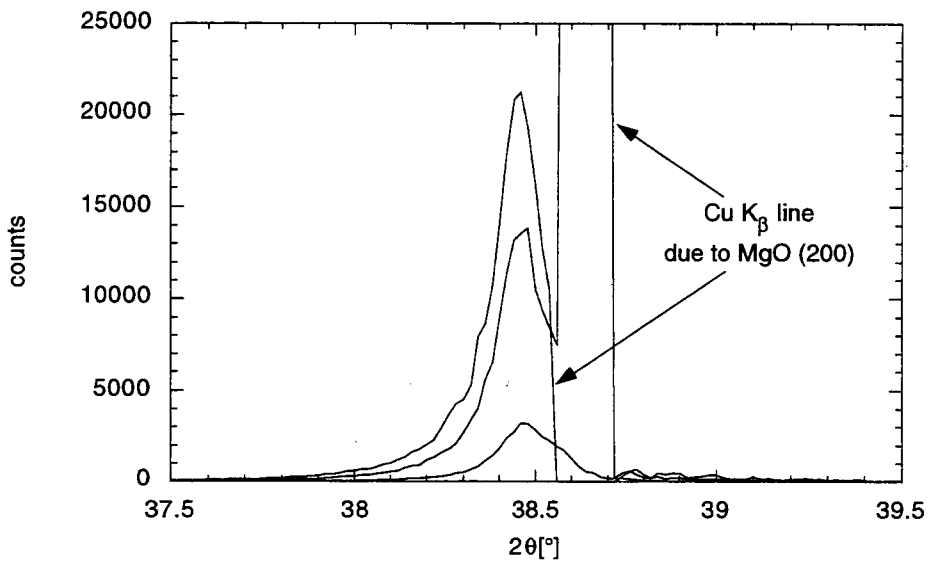

Fig. 3.11 Influence of the Cu K_β line due to the MgO substrate on the shape of the $YBa_2Cu_3O_7$ peak. With a slit with of 0.4°, the spectrometer overflowed and cut out part of the peak. For a 0.2° slit width, it was able to record the very high intensity, showing that one sees two peaks. In the 0.1° slit width case, the Cu K_β line does not cause any problems, but the intensity is significantely reduced. Because the intensity of the substrate peak is still not reduced enough to avoid the overflow problems, usually a slit width of 0.3° is used.

In addition, there can be several lines in the spectra caused by the substrate diffracting wavelengths other than the intended Cu K_α at 1.54Å. In order to get a reasonable intensity for the Cu K_α line, the electrons are accelerated towards the Cu target with about 50 kV. This is enough energy to also excite the Cu K_β line. In order to remove this additional line, a 12 μm Ni filter is put into the beam. This filter reduces the intensity of the K_β line to 1% of the K_α line (and reduces the intensity of the K_α line), but the K_β is still detectable, because the substrate is so strongly diffracting. This is especially annoying in the case of the (005) peak for a $YBa_2Cu_3O_{7-\delta}$ film on MgO, where the K_β from the substrate (200) peak sits near the $YBa_2Cu_3O_{7-\delta}$ (005) peak, and is almost coincident for the $\delta = 0$ case, as seen in Fig. 3.11.

Further non-film lines may be introduced into the spectrum because of the tungsten filament used to supply the electrons which are accelerated

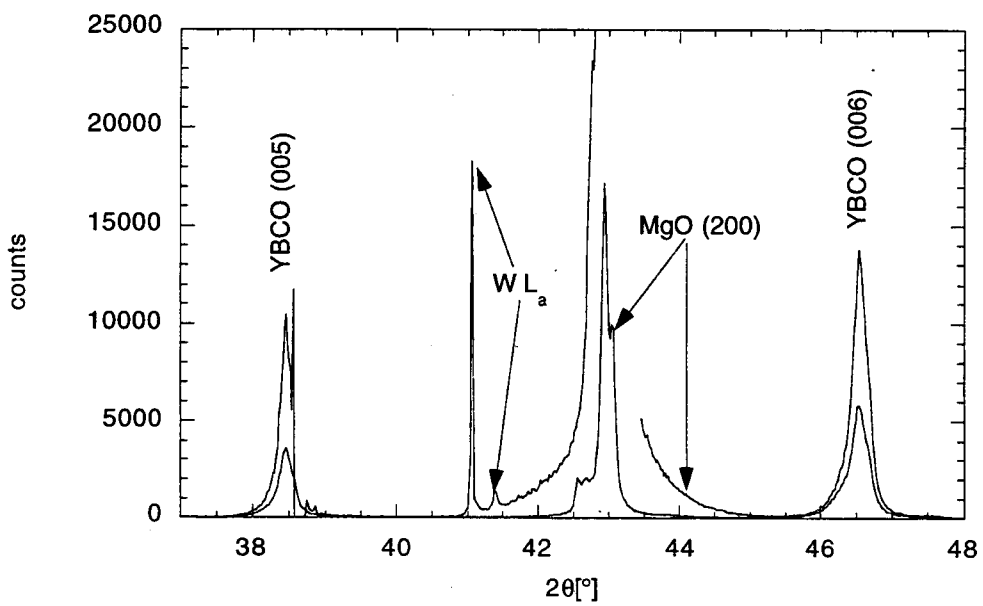

Fig. 3.12 θ-2θ spectra on the same $YBa_2Cu_3O_7$ film deposited on MgO. After the first spectrum was taken, the spectrum was rerun, without remounting the sample. The automatic sample changer was the only thing that touched the sample.

towards the Cu target. When the filament is heated up, it evaporates small amounts of tungsten everywhere in the tube, including on the Cu target. Because the voltage needed to excite the tungsten L line is relatively low (8.4kV), there can be some contamination of the spectra with tungsten lines. Fig. 3.12 shows an example of how tungsten lines will affect a spectrum. The strength of the tungsten lines depends on the age of the x-ray tube; the older the tube the more likely it is to see tungsten lines.

I interpret my x-ray data according to the following procedure: I first check the substrate peaks, and if they overloaded the detector, it means that I mounted the sample properly. If not, I have to decide if the sample changer picked up the sample improperly and I just have to rerun it or if I should remount it.

Then I identify all the $YBa_2Cu_3O_{7-\delta}$ (00*l*) peaks, checking that they are in the right positions and that all other peaks can be accounted for by being substrate related. Any other peaks are an indication of oriented impurities or other orientations of $YBa_2Cu_3O_{7-\delta}$.

Identification of peaks that cannot be traced back to the substrate is an art in itself because in general identification of a material by x-ray diffraction is done with powders. Powder spectra show all possible orientations and not just a selected subset as in the case of oriented film samples. The identification of a powder spectrum is then done by matching the position and intensities of the observed lines and the measured intensities with measured spectra in databases like the JCPDF files, which have been created specifically for this purpose. In oriented film samples, only a few lines are visible. In addition, if there are two different orientations, their ratio will not be the same as in a random powder sample, which means that the ratio of intensities will not be the same as in the data files. The ratios still have to

correspond within a family of planes like, for example, the (00*l*) family, but not in the case of two unrelated orientations. Depending on how many additional peaks one sees, the identification turns into a little more than educated guesswork that must be backed by other methods.

Additional information can be extracted from the x-ray spectra by determining the lattice parameter. This is especially important in the case of oxygen–deficient films, because even though is it significantly harder to associate a *c*-axis length with a certain oxygen content, a *change* in *c*-axis length is an indication that the oxygen content changed.

3.4.2 Determination of Lattice Parameter from X-Ray Data

This following procedure is used to determine the length of the *c*-axis. The first step is to find the exact peak positions of all the (00*l*) peaks. This is done by using a program called PROFILE on Dr. Sleight's x-ray machine, which fits the peaks from the spectra (see Appendix C). In addition to giving the peak position, the program also determines the height, area, FWHM and *d*-spacing of the selected peak. From this the *c*-axis length of each (00*l*) peak is calculated according to

$$c = \frac{l\lambda}{2\sin\theta} \tag{3.17}$$

To get the most precise lattice parameter measurement, one is especially interested in the high angle reflections. The reason can be seen by differentiating Bragg's law with respect to θ.

$$\frac{\Delta d}{d} = -\cot\theta\Delta\theta \tag{3.18}$$

Since cot θ approaches zero as θ approaches 90°, the relative error also approaches zero as θ approaches 90° or 2θ approaches 180° (the maximum possible angle). Simply calculating the lattice parameters from different reflections, plotting them against 2θ and extrapolating to 2θ=180° will not give a very precise result because the resulting function is not linear. Nuffield [41] and Cullity [42] show in their respective x-ray diffraction books that if the calculated lattice parameters are plotted against certain functions of θ, the resulting curves are linear and can be extrapolated with confidence. Nuffield especially goes into detail to derive the different sources of error, for example the displacement of the sample, divergence of the beam and absorption of x-rays by the sample and shows that by plotting the calculated lattice parameter against

$$\frac{\cos^2\theta}{\sin\theta}+\frac{\cos^2\theta}{\theta} \tag{3.19}$$

the most reflections can be used to extrapolate the lattice parameter. Therefore, the *c*-axis length is obtained by plotting the *c*-axis length calculated from Bragg's law against (3.19) and then extrapolating to zero (which is the same as letting θ go to 90°).

For *c*-axis oriented films, the lattice parameter is typically between 11.7 Å for a fully oxygenated film $YBa_2Cu_3O_7$ and 11.88 Å for a $YBa_2Cu_3O_{6.25}$ film. Several factors like cation disorder or inhomgeneity in the sample influence the *c*-axis length and the length even for nominally fully oxygenated $YBa_2Cu_3O_7$ films with good T_c 's can vary between 11.7Å and 11.72Å. Data can be found in Chapter 6.

Chapter 4
Perturbed Angular Correlation Spectroscopy

The main technique used for analyzing our films is PAC (perturbed angular correlation spectroscopy). In a nutshell, PAC investigates the interaction between the quadrupole moment of a probe atom, here ^{111}In, and the electric field gradient at the site of the probe atom. It is done by measuring the angular correlation between two γ-quanta emitted during the decay of the probe atom.

^{111}In substitutes into the $YBa_2Cu_3O_{6+x}$ structure at one single site. It decays with a life time of 2.8 days to an excited state of ^{111}Cd. From this state it decays via a γ–γ cascade into the ground state. The decay scheme for ^{111}In is shown in Fig 4.1. During the time the probe atom is in the intermediate state, the quadrupole moment of the probe atom interacts with the electric field

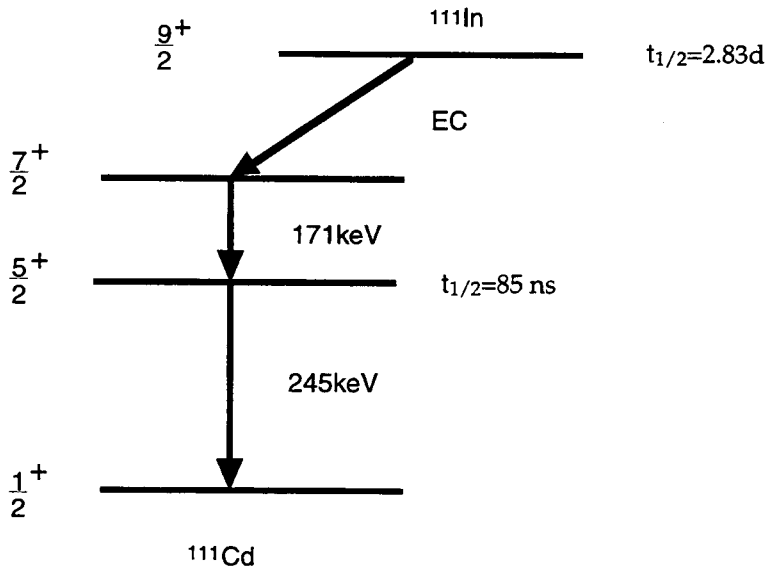

Fig. 4.1 Decay scheme for ^{111}In, showing only the transitions relevant for PAC.

gradient. This interaction changes the correlation between the first γ–quantum and the second one emitted. Compared to the unperturbed case, the second quantum is emitted in a different direction.

It is also possible to investigate interactions with a magnetic field, internal as well as external, but in $YBa_2Cu_3O_{7-\delta}$, the local magnetic field is zero. We tried one experiment to trap magnetic flux, but only about 10% of the applied field of 8 T was trapped, which was too small to measure. This thesis will concentrate only on electric interactions.

4.1 Naive Theory

To get a feel for perturbed angular correlation, one has to look at the angular distribution of the γ-radiation, which is anisotropic in space and depends on the angle between the angular momentum l of the γ-radiation and the quantization axis, commonly referred to as the z-axis. Especially important is that for certain l and m, (the projection of l on the z-axis) there is no emitted radiation along the z-axis.

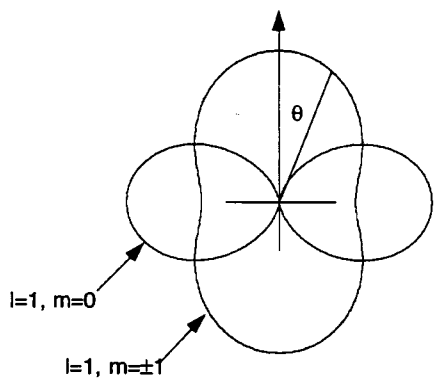

Fig. 4.2 Emitted radiation pattern for $l = 1$ and $m = 0,\pm1$ (dipole radiation). For $l = 1$, $m = 0$, there is no emitted radiation along the z-axis.

Only by the superposition of all possible states does one get an isotropic distribution, which means that for all directions one measures the same intensity. Consider the hypothetical γ–γ cascade with 0–1–0 as the sequence of spins. If for the first detected γ–quantum the quantization axis is taken as the line connecting the nucleus with the detector, only quanta with $m=\pm1$ can be detected, because only they have non-zero intensity in the z-direction, as illustrated in Fig. 4.2. Due to conservation of momentum, this means the nucleus in the intermediate state (with $I = 1$) can only have an angular momentum of $M = +1$ or $M = -1$. By choosing a particular quantization axis, the sublevels are no longer equally populated. If the second quantum is measured *in coincidence* with the first one, it can only be detected in the state $m = \pm1$, because the state $M = 0$ is not populated. It is important that the second quantum has to be in coincidence with the first one, for without the coincidence condition, one would measure an isotropic distribution.

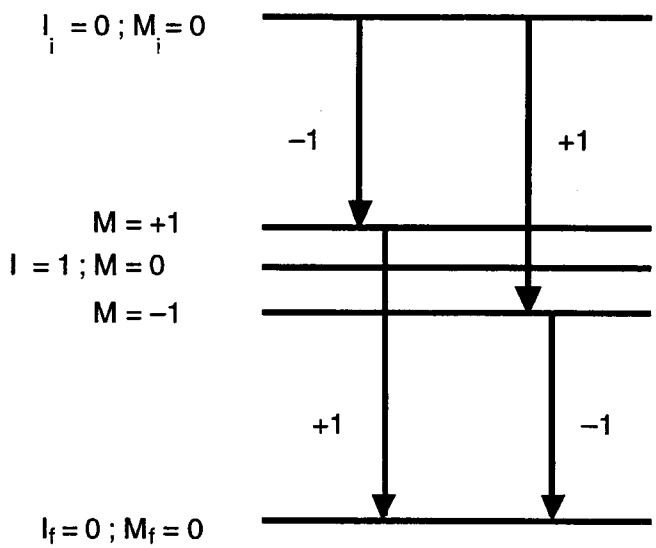

Fig. 4.3 Hypothetical decay scheme of a 0–1–0 cascade. The M levels are degenerate but are displaced for clarity. Note the population of the $M = 0$ level is zero.

Up to now we only have a spatial correlation between the two γ–quanta, which can be described by the angular correlation function $W(\theta)$, defined later in this chapter. The spatial correlation was achieved by fixing the quantization axis by measuring the first γ-quantum, causing certain sub-levels associated with it to become depopulated and then measuring the second quantum in coincidence with the first. In addition one can start a counter when the first γ-quantum arrives and stop it with the arrival of the γ-second quantum (in a standard set up with four detectors, any detector can function as a start or stop detector). If there is an interaction between the aligned spins and some surrounding electric or magnetic field (or both), either due to the structure itself or an externally applied field, the spins will start to precess about the axis of the field (in a classical picture) and subsequently the population of the sublevels will be changed (in a quantum picture). This in turn changes the angular correlation function W, which now will depend on θ and t. This is the basis of PAC–perturbed angular correlation spectroscopy–; due to the interaction of the intermediate state with some field, the angular correlation is changed from the unperturbed state. To sum up the most important points: By measuring the first emitted γ-quantum, certain sublevels for the intermediate state are chosen. Measuring the second γ-quantum *in coincidence* with the first one leads to a spatial distribution of the radiation. If the intermediate state is perturbed by some interaction, either electric or magnetic or both, the emitted radiation does not depend only on the angle, but also on time. Because in a standard set-up the detectors are fixed in space, the change of the correlation function with respect to time is what is being measured.

4.2 In-Depth Treatment

Extensive treatment of how to get from the Hamiltonian to the angular perturbation function $W(\theta,t)$ can be found in several papers and books. The most rigorous is by Frauenfelder and Steffen [45]. Additional treatments can be found in a textbook by Schatz and Weidlich [36] and a paper by Butz [46]. In order to investigate the interaction between the nuclear electric charge distribution $\rho(\mathbf{r})$ and the potential $\phi(\mathbf{r})$ caused by the charge distribution due to the surrounding electrons and positive ions one can write the interaction energy as

$$E_{electr} = \int \rho(r)\Phi(r)\mathrm{d}^3 r \tag{4.1}$$

Expanding the electrical potential in a Taylor series leads to the following expressions:

$$\begin{aligned} E_{electr} &= E^{(0)} + E^{(1)} + E^{(2)} + \ldots \\ &= \Phi_0 \int \rho(\mathbf{r})\mathrm{d}^3 r \\ &+ \sum_{\alpha=1}^{3} \left(\frac{\partial \Phi}{\partial x_\alpha}\right)_0 \int \rho(\mathbf{r}) x_\alpha \mathrm{d}^3 r \\ &+ \frac{1}{2}\sum_{\alpha,\beta} \left(\frac{\partial^2 \Phi}{\partial x_\alpha \partial x_\beta}\right)_0 \int \rho(\mathbf{r}) x_\alpha x_\beta \mathrm{d}^3 r + \ldots \end{aligned} \tag{4.2}$$

The monopole term $E^{(0)}$ introduces the same energy shift for all sublevels m for a given nuclear spin I and the dipole term $E^{(1)}$ vanishes. The quadrupole term $E^{(2)}$, on the other hand introduces an energy shift which depends on the sublevel quantum number m.

This can be seen more clearly after introducing

$$\left(\frac{\partial^2 \Phi}{\partial x_\alpha \partial x_\beta}\right)_0 = \Phi_{\alpha\beta} \tag{4.3}$$

diagonalizing this symmetric matrix and splitting off another monopole term which describes the interaction of the extended nucleus with the electrons at the nuclear site. If one additionally defines the electric quadrupole moment as

$$Q_{\alpha\alpha} = \frac{1}{e}\int \rho(\boldsymbol{r})(3x_\alpha^2 - r^2)\mathrm{d}^3r \tag{4.4}$$

and the electric field gradient $V_{\alpha\alpha}$ via

$$\Phi_{\alpha\alpha} = V_{\alpha\alpha} + \frac{1}{3}\sum\Phi_{\alpha\alpha} \tag{4.5}$$

one is left with the energy

$$E_Q = \frac{e}{6}\sum_\alpha V_{\alpha\alpha}Q_{\alpha\alpha} \tag{4.6}$$

which means that the energy is the product of the electric field gradient with the nuclear electric quadrupole moment. The m dependence of this energy comes from expressing the electric quadrupole tensor with the help of spherical harmonics and calculating the matrix elements (a more in–depth treatment of the above paragraph is in Ref. [36]).

We take a closer look at the electric field gradient, the quantity of interest that we measure in the PAC experiments. It is considered an interaction reaching not much further than next-nearest neighbors and as we have seen from the above discussion, it yields information about the strength and symmetries of the charge distribution surrounding the probe atom. $V_{\alpha\beta}$ is a second degree tensor which is symmetric, diagonal and traceless (due to the definition) and can therefore be described completely by five components.

The Hamiltonian for the quadrupole interaction using the above definition of the electric field gradient can be written as

$$\mathrm{H}_Q = \frac{eQ}{6I(2I-1)}\sum_{\alpha,\beta}V_{\alpha\beta}\left[\frac{3}{2}(I_\alpha I_\beta + I_\beta I_\alpha) - \delta_{\alpha\beta}I^2\right] \tag{4.7}$$

Because the tensor of the electric field gradient is symmetric, one can choose a principal-axis system in which $V_{\alpha\beta} = 0$ for $\alpha \neq \beta$. In this coordinate system, the above equation becomes

$$H_Q = \frac{eQ}{4I(2I-1)}\left[V_{zz}(3I_z^2 - I^2) + \frac{1}{2}(V_{xx} - V_{yy})(I_x^2 - I_y^2)\right] \tag{4.8}$$

The above equation shows that two parameters of the electric field gradient are enough to describe the interaction with the quadrupole moment. Usually the largest component of the field gradient V_{zz} and the difference $V_{xx}-V_{yy}$ are given. The difference is given by introducing a new parameter, the asymmetry η, which is defined as

$$\eta = \frac{V_{xx} - V_{yy}}{V_{zz}} \tag{4.9}$$

with $|V_{xx}| \leq |V_{yy}| \leq |V_{zz}|$. Because the electric field gradient tensor is traceless and with the above relationship between the V_{ii}, $0 \leq \eta \leq 1$ holds. In addition, by giving V_{zz} and η, the other two components can be calculated.

The remaining three parameters which are necessary to describe the electric field gradient tensor within any system of coordinates are the three Euler angles. They are used to transform the laboratory coordinate system, which is usually the host crystal system, into the principal axis system of the electric field gradient.

4.3 General Perturbation Function

Several intrepid theorists, especially Frauenfelder and Steffen [45] put the above description into a solid theoretical framework and showed how the decay of a probe atom via a $\gamma-\gamma$ cascade and the interaction of the intermediate state with either an electric or a magnetic field can be expressed

in an terms of an angular correlation function. In its most general form, the perturbed angular correlation function can be written as

$$W(\mathbf{p}_{\gamma_1},\mathbf{p}_{\gamma_2},t)=\sum_{k_1,k_2}A_{k_1}(\gamma_1)A_{k_2}(\gamma_2)\frac{1}{\sqrt{(2k_1+1)}\sqrt{(2k_2+1)}}$$
$$\bullet\sum_{N_1,N_2}G_{k_1k_2}^{N_1N_2}(t)Y_{k_1}^{N_1^*}(\theta_1,\varphi_1)Y_{k_2}^{N_2}(\theta_2,\varphi_2) \qquad (4.10)$$

the angles and directions are defined in Fig. 4.4, the Y_k are the spherical harmonics, the $A_{k_1}(\gamma_1)$ and $A_{k_2}(\gamma_2)$ are angular correlation coefficients. They depend on the spins of the nuclear states and the angular momentum l of the emitted γ-rays, but are independent of any kind of perturbation. These coefficients can be calculated for general nuclei (see Ref. [46]) and for the ^{111}In can be calculated from a table by Ferentz and Rosenzweig (in [45]) and are:

$$A_2(\gamma_1) = 0.3299,\ A_2(\gamma_2) = -0.5345,\ A_4(\gamma_1) = 0.0023,\ A_4(\gamma_2) = -0.6172$$

These theoretical values have to be corrected for the finite solid angles of the detectors and for the distance from the sample to the detector.

Because of conservation of parity, the sum runs only over even k_i. Terms with $k_i > 4$ contribute less than 1% and are neglected. The information about the interaction of the intermediate nuclear state with spin I is contained in the $G_{k_1k_2}^{N_1N_2}$. These perturbation functions are given by:

$$G_{k_1k_2}^{N_1N_2}(t)=\sum_{m_a,m_b}(-1)^{2I+m_a+m_b}\sqrt{2k_1+1}\sqrt{2k_2+1}\begin{pmatrix} I & I & k_1 \\ m_a & -m_a & N_1\end{pmatrix}\begin{pmatrix} I & I & k_2 \\ m_b' & -m_b & N_2\end{pmatrix} \qquad (4.11)$$
$$\bullet\langle m_b|\Lambda(t)|m_a\rangle\langle m_b'|\Lambda(t)|m_a''\rangle^*$$

The $\Lambda(t)$ is the time evolution operator, which is given for time-independent interactions by:

$$\Lambda(t) = e^{-i\hat{H}t/\hbar} \tag{4.12}$$

$\hat{H}$ is the Hamiltonian describing the interaction of the intermediate nuclear state with its environment via the nuclear dipole or quadrupole moment.

Butz [46] showed in his paper how the above $G_{k_1k_2}^{N_1N_2}$ can be transformed into a significantly easier form. This is done by calculating the matrix elements. Furthermore, it can be shown that for static electric quadrupole interaction the perturbation functions are real. As a consequence, the exponentials will turn into cosines during the calculations and one can put

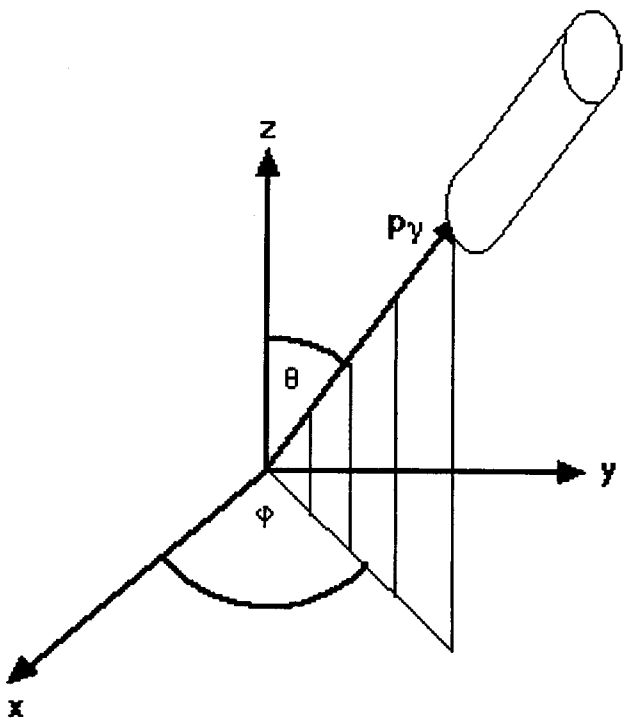

Fig. 4.4 Definitions of angles and orientations for detector–probe system. For clarity, only one detector is shown, but a real PAC set up has at least 2 detectors, the standard set up has 4 detectors, in one plane and at 90° to each other.

the correlation function into the much simpler looking form:

$$W(\mathbf{p}_{\gamma_1}, \mathbf{p}_{\gamma_2}, t) = 1 + S_0' + \sum_{n=1}^{3} S_n' \cos \omega_n t \qquad (4.13)$$

The S_k contain all the information about the orientation of the electric field gradient and the detectors relative to the crystal lattice, as well as the angle θ between $\mathbf{p}_{\gamma_1}$ and $\mathbf{p}_{\gamma_2}$. They also depend on the asymmetry η as do the frequencies ω_k. Butz [46] gives analytical solutions for the perturbation functions and the frequencies, while Wegner [47] gives the perturbation functions for doped cubic single crystals in different orientations and for

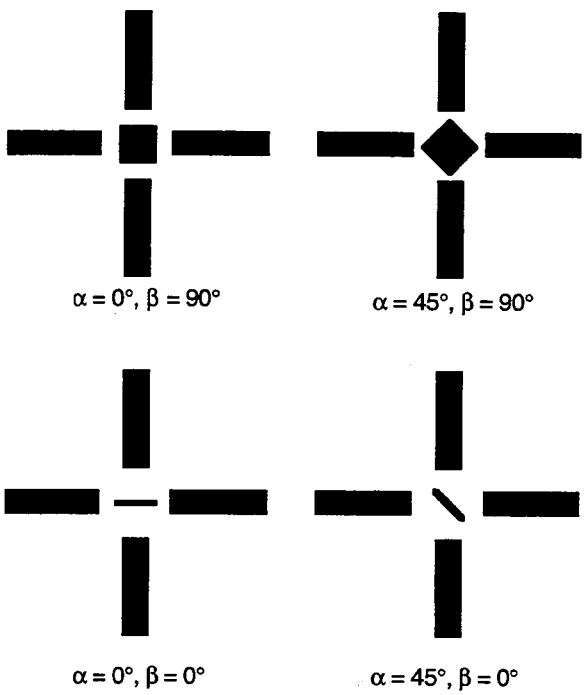

Fig. 4.5 Definition of angles used to describe the orientation of the film relative to the detectors. α gives the angle between the (100) direction of the substrate and a line connecting two detectors (at 180° to each other), β is the complement of the angle between the normal to the detector plane and the substrate normal, when the substrate is rotated about an axis parallel to the (100) direction. This figure give a bird's–eye–view of the four orientations used in this thesis and the associated α and β.

different values of the asymmetry, stretching over several pages. These functions are rather complicated and it would go beyond the scope of this thesis to even start quoting them, because they depend on so many different factors and they are seldom intuitive.

Because the PAC investigation are carried out on films, the angles describing the orientation of the substrate relative to the detectors have to be defined. Positioning the normal of the substrate perpendicular to the detector plane, α is the angle between the (100) direction of the substrate and a line connecting two detectors. The angle β is the complement of the angle between the normal of the detector plane and the normal to the substrate, when the substrate is rotated about an axis parallel to the (100) direction of the substrate, starting from the position used to define α. A substrate in the detector plane therefore has $\beta = 90°$, a substrate with the normal in the detector plane has $\beta = 0°$. Fig. 4.5 shows a birds–eye view of the four orientations used in this thesis.

To illustrate how the orientation of the electric field gradient influences the spectra, we consider a sample with the main axis of the electric field gradient pointing perpendicular to the detector plane. There are no differences (within error bars) between a spectrum taken with the corners of the film pointing into the detectors ($\alpha = 45°$) or between the detectors ($\alpha = 0°$) (Fig. 4.5 defines these angles).

As a different example, one sees a marked difference if the main axis of the electric field gradient is in the detector plane. In this case, taking a *c*-axis oriented orthorhombic film, which has the main axis of the electric field gradient along the *b*-axis, in the $\alpha = 0°$ spectrum, which has the main axis of the electric field gradient pointing into the detectors, ω_1 is the strongest component, while ω_2 is suppressed. In the $\alpha = 45°$ spectrum, with the main axis of the electric field gradient now pointing in between the detectors, ω_1 is

suppressed, while ω_2 is the strongest component. In all orientation, the amplitude of ω_3 is very small. In a powder spectrum, which averages over all possible orientations, the amplitudes decrease with increasing frequency.

Fig. 4.6 shows calculations done by Dr. Roland Platzer which illustrate the influence of the different orientations and the symmetry on the different

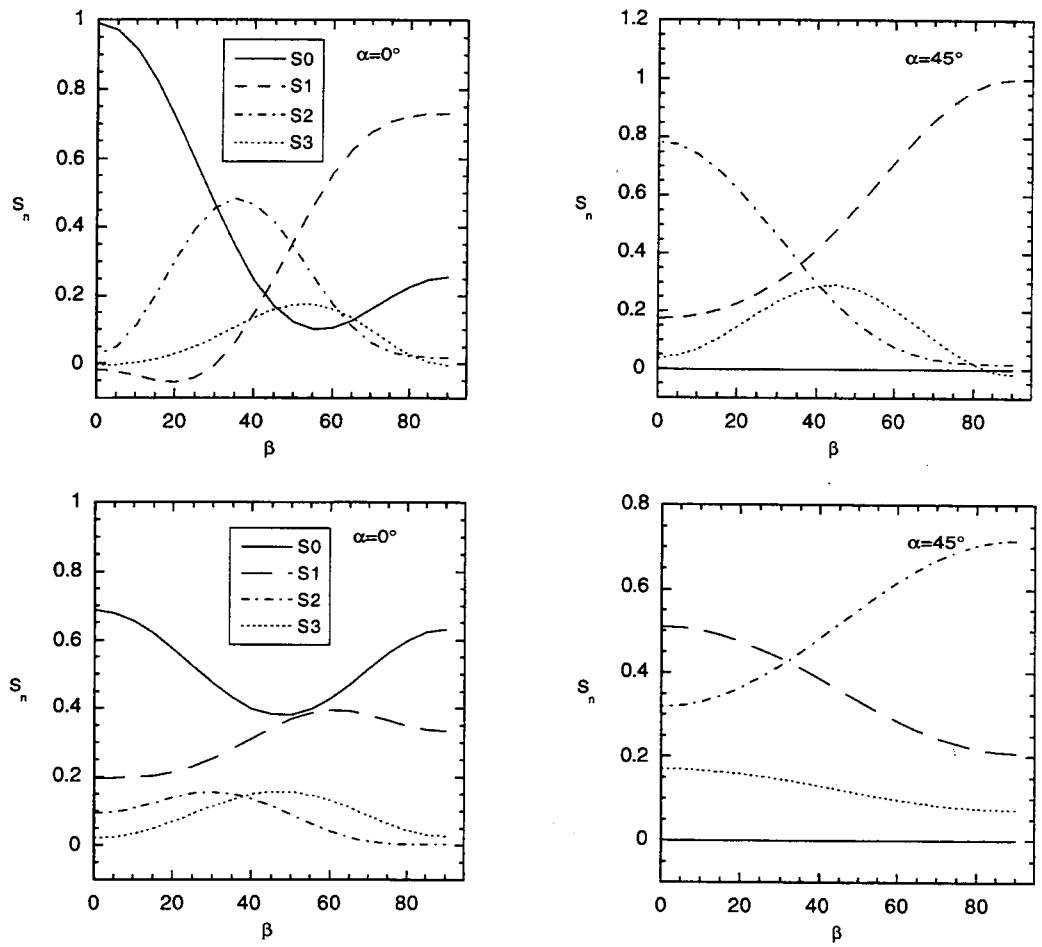

Fig. 4.6 Calculated amplitudes for different orientations, with the electric field gradient perpendicular to the film plane or in the film plane. The upper two plots assume the main axis of the electric field gradient perpendicular to the film plane and $\eta = 0.4$. (Used for *c*-axis oriented $YBa_2Cu_3O_{6.25}$.) The two lower plots assume a completely twinned film with the main axis of the electric field gradient in the film plane and $\eta = 0.5$ (Used for *c*-axis oriented $YBa_2Cu_3O_7$.) The angles are defined in Fig. 4.5.

amplitudes and are a summary as well as an extension of the discussion in the above paragraph. The calculations were done for a *c*-axis oriented, tetragonal $YBa_2Cu_3O_{6.25}$ film, with an asymmetry $\eta = 0.4$ as well as for a *c*-axis oriented, completely twinned $YBa_2Cu_3O_7$ film. Note that for the tetragonal case for $\beta = 90°$, the Si are almost the same for $\alpha = 0°$ and $\alpha = 45°$, except for the hard–core contribution. The main axis of the electric field gradient is perpendicular to the detector plane and rotating the film by 45° does not make much of a difference.

Fig. 4.7 illustrates the above discussion and shows the spectra of an orthorhombic and a tetragonal film in the same orientation ($\alpha = 45°$, $\beta = 90°$).

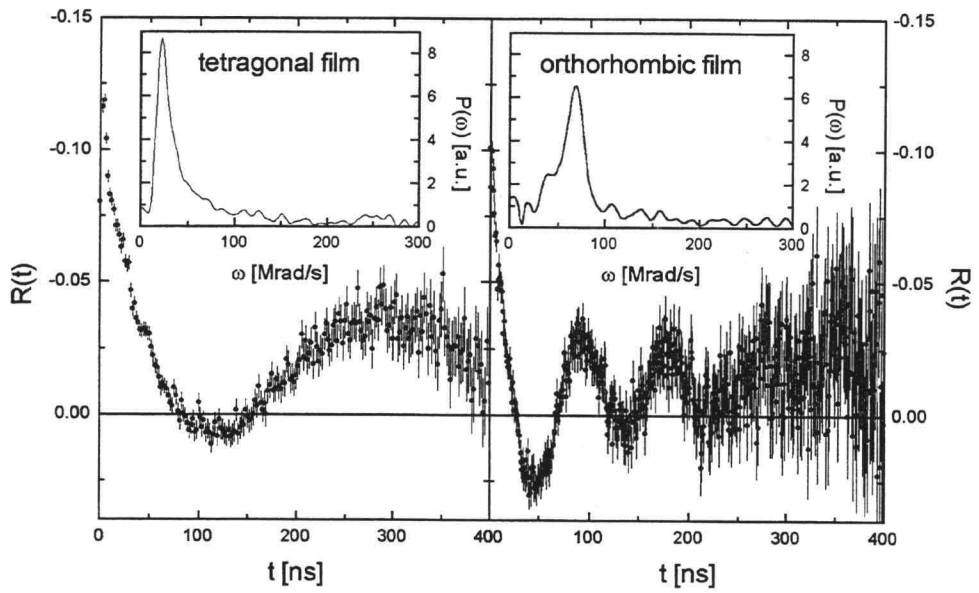

Fig. 4.7 $R(t)$ and Fourier transform of a tetragonal (left) and an orthorhombic film, with the films in the same orientation ($\alpha = 45°$, $\beta = 90°$). The $R(t)$ spectra clearly show the higher frequency of the orthorhombic film, the data "wiggles" a lot faster. The Fourier transforms shows the orientation dependence more clearly, with ω_2 suppresed for the tetragonal film, and ω_1 suppresed for the orthorhombic film.

All the analysis is done in the time domain, but it is often easier to look at and interpret the spectra in the frequency domain. As can be clearly seen, in the orthorhombic phase the amplitude of ω_1 is suppressed and in the tetragonal phase, the amplitude of ω_2 is suppressed (for the immediate comparison, one also has to remember that the value of ω_1 in the tetragonal case is about 1/2 of the orthorhombic case.

The change in the amplitudes for the different phases and orientations shows clearly that the electric field gradient changes orientation. From our experiments we deduce that the main axis of the electric field gradient (V_{zz}) changes from pointing along the *c*-axis in the tetragonal phase to pointing along the *b*-axis in the orthorhombic case, which is in agreement with the theoretical calculations by Yu *et al.* [48].

4.4 Data Acquisition

In order to take a PAC spectrum, at least two detectors are needed. Several different kinds can be used, depending on requirements for energy and time resolution. We use BaF_2 scintillation detectors ($\Delta t \approx 300$ ps for 511 keV γ–rays). The γ–quantum enters the detectors and interacts with the detector material either due to the photo–effect or Compton effect, creating an excited electron. This electrons excite (or ionize) atoms in the scintillator with the number being proportional to E_e. The excited atoms relax by emission of light, which enters a photomultiplier that gives a signal proportional to the energy of the original γ–quantum. One detector is used as the start detector, and starts a clock when γ_1 is detected. The second one stops the clock as soon as it detects γ_2. For ^{111}In, γ_1 has an energy of 171 keV and γ_2 of 245 keV, and the detectors can clearly differentiate between the two γ–quanta. In a standard

4–detector set up, each detector can be a start and stop detector. The time difference t are binned by a multi-channel analyzer. Over time, a coincidence spectrum is collected.

The coincident count rate N_{ij} between a start detector i and a stop detector j is related to the angular correlation function $W(\theta,t)$ by:

$$N_{ij}(\theta,t) = N_0 \exp(-\frac{t}{\tau_N}) W(\theta,t) + B \tag{4.14}$$

B is the time-independent background random coincident count rate and is subtracted, τ_N is the lifetime of the intermediate level (85 ns for ^{111}In).

In order to collect as much information as possible, several detectors are used with the most common arrangement being four detectors at 90° to each other, each of which can be used as a start or stop detector. This leads to 12 possible coincidence spectra. In order to extract the perturbation function $W(\theta,t)$ and hence the asymmetry and the orientation of the electric field gradient, different count rate ratios can be formed. The ratio used here is:

$$R(t) = 2\frac{N_{13}(180°,t) + N_{24}(180°,t)}{N_{14}(90°,t) - 2N_{23}(90°,t)} \approx \frac{2}{3}\left[\sqrt{\frac{N_{13}(180°,t)N_{24}(180°,t)}{N_{14}(90°,t)N_{23}(90°,t)}} - 1\right] \tag{4.15}$$

The second ratio is a very close approximation of the first one and shows more clearly that the detector efficiencies cancel, if self-absorption in the sample is negligible [49], which is the case in a thin film.

This equation is the starting point for extracting data. The above equation is fitted to

$$R(t) = A_{22} \sum_i f_i \sum_{n=0}^{3} S_{kn}(\eta) \cos[\omega_n(\eta)t] \exp(-\Delta\omega_n t) \tag{4.16}$$

A_{22} is the effective anisotropy, typically ≈ –0.1 for ^{111}In. In the case of several different probe sites, an appropriate fraction f_i is assigned to the different sites with $\sum_i f_i = 1$. The S_n contain the information about the orientation of the electric field gradient, while the ω_n contain the information

about the asymmetry η and the strength of the electric field gradient V_{zz}. The exponential term is included to account for minor variations in the electric field gradient due to impurities and other defects.

To get as good a fit as possible, good statistics are crucial. Spectra should have at least 20000 counts, but ideal would be 100000. Right after deposition, about 2000 counts/hour are accumulated, but even at this count rate, it would take over two days to get 100000 counts. We make do with the 20000 counts in order to be able to perform as many experiments as possible.

4.5 Data Analysis

The actual fitting is done by a program written by Dr. B. Lindgren (Uppsala University, Sweden) and modified by Dr. Roland Platzer. The program uses a least squares fit to vary the frequencies, asymmetry, the frequency distribution, the fraction of probes in one site as well as the Euler angles (and therefore the orientation of the electric field gradient), trying to achieve the best fit possible, with the user determining which parameters should be fit parameters and which should be fixed. It takes the data and an estimate for the Euler angles which connect the laboratory frame with the principal axis system of the electric field gradient. (Even though both coordinate systems use x, y and z for their axes, none of these axis have to be the same (but they can be)). The lab system is transformed into the principal axis system of the field-gradient via three rotations characterized by these Euler angles.

The fitting program calculates $R(t)$ from equations (4.10) and (4.11). and compares it with the measured $R(t)$. Calculating this $R(t)$ is the heart and soul

of the program. Equation (4.11) contains information about the transition itself, while equation (4.10) contains the information about the orientation of the electric field gradient due to the spherical harmonics, which are tied to the laboratory coordinate system via the Euler angles.

Even though it sounds fairly automatic, there are still points were human intervention is needed. Because the program does the fit numerically, step sizes are involved. This can become important especially with the Euler angles, because one has to differentiate them numerically, and it is possible to overshoot with too big a stepsize. An additional factor, especially in films which are inherently more disordered than crystals, is the so-called missing fraction, from probes which are not in a well-defined surrounding and therefore only contribute to an amorphous background signal. In our films this fraction is about 40%, and must be taken into account, to achieve a good fit. To achieve the best fit, several spectra for different orientations are fitted at the same time. The best fit with respect to the Euler angles is achieved with fitting the $\alpha = 45°$ spectra simultaneously.

The user also has to determine the number of parameters to be fitted and check if the results obtained are reasonable or whether one should start with a different set of initial parameters. (As can happen with fitting routines, if the starting parameters are too far away from the true values, the routine might not find the solution). Also, depending on what orientations have been measured, not all variables can be fitted. For a tetragonal, *c*-axis oriented $YBa_2Cu_3O_{6.25}$ film, η cannot be determined if the sample has only been measured in the $\beta = 90°$ (horizontal) orientation, because in this case, the main axis of the electric field gradient is perpendicular to the detector plane. (This is not quite true; for samples with a narrower linewidth is would be possible to fit the η, but we need two orientations to get a good fit.)

Some comments have to be made with respect to the fast Fourier transforms (FFT) commonly shown in the spectra which are intended only as a guide to the eye. All of the analysis is done on the R(t) spectra, but it is easier to see which component is the strongest in the Fourier spectra. Because the time window is limited to 500 ns (and the function has to converge to zero for the FFT to work, which is done by subtracting the background and using an envelope function), there already is an uncertainty of 2 MHz in Fourier spectra, which for the 20 MHz tetragonal line is 10%. This linewidth is not the true linewidth, which is calculated from the fit done according to (4.16). If one of two lines looks narrower in the FFT, the linewidth will also be narrower in the fit.

The linewidth may depend on the temperature. It first increases with increasing temperature, because with the motion of the atoms due to the temperature, each probe atom experiences a slightly different environment, which translates into a broadened linewidth. Once the timescale of this motion is of the same order as the lifetime of the intermediate state or faster the motion averages out, the probes all see an average environment and the linewidth narrows again. This is referred to as motional narrowing.

4.6 Perturbed Angular Correlation Experiments in $YBa_2Cu_3O_{7-\delta}$

Nuclear hyperfine spectroscopies are among the myriad techniques brought to bear on $YBa_2Cu_3O_{7-\delta}$. Nuclear magnetic resonance and Mössbauer Spectroscopy are more common techniques and their results are nicely reviewed in Ref. [50], but PAC has the advantage of being more sensitive and temperature independent. PAC measures the strength, and in oriented material, the direction of the principal components of the electric field

gradient. Virtually all the PAC work on $YBa_2Cu_3O_{7-\delta}$ has been done on powders, because it is easier to incorporate the radioactive isotope. However, in powder or polycrystalline samples, information is lost about the orientation of the electric field gradient with respect to the crystal structure, because the microcrystallites are randomly oriented.

PAC in $YBa_2Cu_3O_{7-\delta}$ poses several problems. The first is how to get the probes atoms into the material, because fairly stringent criteria have to be met for an atom to be suitable for PAC. Usually ^{111}In is used, even though it is not part of the $YBa_2Cu_3O_{7-\delta}$ structure, but ^{133}Ba is not a very favorable probe atom [51] because of its small anisotropy and short halflife of the intermediate state. There are several different ways to introduce ^{111}In into $YBa_2Cu_3O_{7-\delta}$, each with its own limitations. Bartos and Uhrmacher [52] introduced the PAC probes into pressed powder samples via ion implantation, accelerating the In^+ ions to energies of 400keV, achieving an implantation depth of ≈100 nm. This method has the disadvantage that it causes radiation damage, clearly visible in their PAC spectra, and has to be annealed out, using temperatures between 975K and 1275K and another annealing step at 775K in order to restore the oxygen content. A different approach was chosen by Saitovitch *et al.* [53], who diffused the indium into their powder samples at temperatures between 500 °C and 750 °C. Schwenker [54] and Füssel [55] used a sol-gel method to incorporate the indium during the formation of the $YBa_2Cu_3O_{7-\delta}$ powder.

The approach taken in our laboratory is to implement a fourth source in the evaporation system [56] which incorporates about 10^{11} atoms during the deposition of the film, causing the indium atoms to be incorporated while the structure is forming.

In most of the early ^{111}In:$YBa_2Cu_3O_{7-\delta}$ PAC experiments, several different sites were identified, most attributed to ^{111}In substitution at different

sites within the $YBa_2Cu_3O_{7-\delta}$ structure. Bartos and Uhrmacher [52] have an extensive list in their paper summarizing the frequencies and the suggested site identifications.

More recent work on PAC on $YBa_2Cu_3O_{7-\delta}$ and possible impurities in Refs. [55], [57-61] show that ^{111}In substitutes at only one location in the $YBa_2Cu_3O_{7-\delta}$ lattice, with all the evidence pointing towards the yttrium site with a $\nu_Q = 39$ MHz, and $\eta = 0.5$. All the other observed sites can be attributed to impurities, formed either during the sample preparation or while incorporating the indium into the structure and the anneal that usually follows.

The evidence for the indium substituting for yttrium is only circumstantial, but several good arguments can be made. Both indium and yttrium have valence 3^+ and their ionic radii are very close ($r_Y = 0.89$Å, $r_{In} = 0.91$Å), while the radii for Cu and Ba are 0.69Å and 1.35Å, respectively. A study done by Weidlich [62] showed that up to 3 atom % of the yttrium can be exchanged with indium. If doped above the solubility limit, $InBa_2Cu_3O_x$ forms. Uhrmacher and Bartos [58] show that using a simple point charge model to calculate the frequencies, the yttrium site has a significantly lower frequencies than all the other sites. Furthermore, the PAC data taken in this laboratory [27] agree very well with the theoretical predictions by Yu *et al.* [48] for a substitution at the yttrium site. Additional work by me, presented in Chapter 5, shows that if an impurity can be identified in the x-ray spectra, only the impurities containing yttrium will show additional PAC signals. None of these arguments taken by itself is strong enough to state clearly that the indium substitutes at the yttrium site, but taken together, they make a very strong case.

Measuring the electric field gradient at the yttrium site is especially important because the two main theories by Ambrosch–Draxl *et al.* [63] and by Yu *et al.* [48], while agreeing for all the other possible sites in the orientation and the strength, differ for the yttrium site. Yu *et al.* [48] calculate the main axis of the field gradient to be pointing along the *b*-axis with a V_{zz} of $0.201 \times 10^{22} Vm^{-2}$ and an asymmetry $\eta = 0.43$, the Ambrosch–Draxl [63] paper calculates the main axis of the electric field gradient pointing along the *c*-axis with a V_{zz} of $0.34 \times 10^{22} Vm^{-2}$ and an asymmetry $\eta=0.9$. Because all the other research had been done on powders[12], the orientation could not be determined. Tom *et al.* [56] found that in twinned $YBa_2Cu_3O_{7-\delta}$ films the electric field gradient was in the *ab*-plane, but the research on *a*-axis oriented films in this thesis was needed to determine the direction of the main axis of the electric field gradient, which points along the *b*-axis, as predicted by Yu *et al.* [48].

Observing the electric field gradient can be used to get some insight into the motion of oxygen in $YBa_2Cu_3O_{7-\delta}$. The frequency decreases with decreasing oxygen content as shown by Plank *et al.* [64] or with increasing temperature (which according to the phase diagram is essentially the same as decreasing the oxygen content [65]). In addition, work done here on tetragonal films (Ref. [65] and this thesis) showed that with the phase transition the main axis of the electric field gradient changed from being along the *b*-axis to being along the *c*-axis. Tröger and Butz [51] used ^{133}Ba as the probe atom which has the advantage of being very close to the Cu–O chains which are responsible for the oxygen ordering, found a static electric field gradient for

---

[12] Plank *et al.* [64] published a spectrum done on a $YBa_2Cu_3O_{7-\delta}$ film on $SrTiO_3$, but the spectrum is more likely to be of $Y_2Cu_2O_5$. They identified it as the Cu(1) site in $YBa_2Cu_3O_{7-\delta}$ and did not determine the orientation of the main axis of the electric field gradient.

temperatures up to 400 K (100 °C). For higher temperatures the observed data can be explained by a fluctuating electric field gradient due to oxygen diffusion. Theoretically, their data could be used to derive a hopping rate, but because of insufficient accuracy in the data they did not try this approach.

Chapter 5
a-Axis Oriented $YBa_2Cu_3O_{6+x}$ Films

$YBa_2Cu_3O_{6+x}$ can be grown epitaxially in several preferred orientations. The most commonly grown orientations are with the *c*-axis normal to the substrate or the *a*-axis normal to substrate. It is usually easy to grow *c*-axis oriented material with very good characteristics, but for films with the *a*-axis normal to the substrate, the characteristics are not quite as good as in general they have lower T_c, but there is interest in growing films in this orientation.

From an applications point of view, it is advantageous to grow films with the *a*-axis normal to the substrate because the current transport takes place mostly in the *ab*-plane. The coherence length along the *ab*-plane ($\xi_{ab}\approx$1.2–1.5 nm) [66] is much longer than the coherence length along the *c*-axis (ξ_c=0.1–0.3 nm), which makes *c*-axis oriented films less suited for the production of superconductor–normal conductor–superconductor (SNS) or superconductor–insulator–superconductor (SIS) Josephson tunnel junctions.

There is another reason to investigate the *a*-axis films. Previous PAC experiments in this laboratory on twinned *c*-axis oriented films were able to establish that the main axis of the electric field gradient in $YBa_2Cu_3O_7$ is in the *ab*-plane but, due to the twinning, could not distinguish between the *a*- or *b*-directions. Furthermore, the two main theories differ in the predicted orientation of the main axis of the electric field gradient with respect to the yttrium site. Yu *et al.* [48] calculated the main axis of the electric field gradient at this site to be pointing along the *b*-axis, but Ambrosch–Draxl [63] calculated it as pointing along the *c*-axis. Our PAC experiments on *a*-axis oriented films were able to confirm Yu's predictions.

The usual consensus is that in order to grow *a*-axis oriented films, the temperature of the substrate has to be about 100 °C [13] lower than in the case of the *c*-axis film (see for example Refs. [67-69]). Yet there are several other factors which also play an important role in what fraction of the film grows in which direction. The choice of substrate is important and the optimum temperature varies for different substrates, a fact that Ref. [70] demonstrates very clearly. They conclude that *a*-axis growth is favored by good lattice matching and in order to achieve *c*-axis growth, a higher substrate temperature is needed. In addition, the oxygen pressure during the deposition influences the orientation, shown in Refs. [71] or [72]. Terashima *et al.* [71] investigated films sputtered at temperatures between 530 °C and 680 °C. At an oxygen pressure of 0.032 Pa there was only *c*-axis oriented growth, while for pressures greater than 0.65 Pa, only *a*-axis oriented growth was found. On the other hand, sputtering a film at 730 °C yielded *c*-axis oriented growth even at a pressure of 0.32 Pa. Zhong *et al.* [72] found, using MOCVD to deposit their films, that the higher the total partial pressure of the oxidizers, the wider the temperature window they had to grow films in a purely *a*-axis normal orientation. Yet all these papers show that the most important factor is lowering the substrate temperature, the other factors listed above only improve the ratio of *a*-axis oriented grains to *c*-axis oriented grains.

On the other hand, a lower substrate temperature during deposition is detrimental to the quality of the film produced. *a*-axis films usually show reduced T_c and their resistance vs temperature curves do not have the shape that is expected from a good *c*-axis film, namely linear (extrapolating to zero)

---

[13] The different growth techniques like sputtering, MBE, reactive co-evaporation or laser ablation have different optimum temperatures for the respective orientations. This is due to the fact that, depending on the technique, the evaporants hit the substrate with different energies.

until slightly higher than the transition temperature, with a very narrow transition (< 1 K). Raven *et al.* [73] show nicely how the shape of the resistance vs temperature changes with the change in the ratio of *a*-axis oriented grains to *c*-axis oriented grains. With increasing *a*-axis fraction, the transition temperature is lower, the curves remain linear, but the slope becomes shallower. One of their resistance vs temperature curves first shows a slight decrease in resistance with decreasing temperature, but at around 200 K, the resistance rises again, before the sample goes through the superconducting transition. They also show that this change in the resistance curves is different from the change introduced by a change in oxygen content, which changes the transition temperature, but not the slope of the curve. Li *et al.* [69] investigated the dependence of several film characteristics with decreasing substrate temperature. The T_c of a film deposited at 690 °C, which does not show any *a*-axis growth, is 90 K, decreasing with decreasing substrate temperature so that for the film deposited at 570 °C, which clearly shows *a*-axis peaks in the x-ray diffraction spectrum, the T_c is 82 K. The critical current density decreases from being higher than 10^6 A/cm^2 for the film deposited at 650 °C to slightly more than 10^4 A/cm^2 for the film deposited at 570 °C. The FWHM (full width half maximum) of the (006) x-ray diffraction peak widened from about 0.3° for the film deposited at 690 °C to almost 0.6° for the film deposited at 570 °C, indicating decreased crystallinity with increasing *a*-axis content.

In order to improve the quality of the films, a template method, with either the same material or a different one, is often used. This technique was pioneered by Inam *et al.* [74]. Trying to grow $YBa_2Cu_3O_{7-\delta}/PrBa_2Cu_3O_{7-y}$[14]

[14] $PrBa_2Cu_3O_{7-y}$ is not superconducting and is used in conjunction with $YBa_2Cu_3O_{7-\delta}$ to make devices with several epitaxial layers

superlattices, they noted that the $PrBa_2Cu_3O_{7-y}$ layer occasionally had grains with the *a*-axis normal to the substrate and that this was less common in the $YBa_2Cu_3O_{7-\delta}$ layer. $YBa_2Cu_3O_{7-\delta}$ that nucleated on top of these *a*-axis oriented grains grew with an *a*-axis orientation under conditions that normally yield *c*-axis oriented material. Investigating the optimum conditions, they showed by ion channeling experiments that there is an optimum temperature for *c*-axis oriented growth (820 °C) and an optimum temperature for *a*-axis oriented growth (700 °C) of the template layer with the region in between showing mixed *a*- and *c*-axis growth and decreased crystallinity. $YBa_2Cu_3O_{7-\delta}$ films deposited at 800 °C on a template layer of $PrBa_2Cu_3O_{7-y}$ deposited at 700 °C showed less than 5% *c*-axis oriented grains in x-ray diffraction studies and a T_c of 83 K in ac susceptibility measurements. A more recent paper by Trajanovic *et al.* [75] using the same technique achieved T_c's of up to 88 K. Rosova *et al.* [76] showed that the deposition temperature of the template influences the volume fraction in the $YBa_2Cu_3O_{6+x}$ film with 98.6% for a template deposited at 680 °C, decreasing to 56.1% for a template deposited at 700 °C, even though the films were all deposited at the same temperature of 710 °C. This result can be interpreted with the help of the paper by Inam *et al.* [74], because it clearly shows that the amount of *a*- and *c*-axis oriented grains in the template layer determine the orientation in the $YBa_2Cu_3O_{7-\delta}$ film.

Sodtke and Münder [77] investigated the reason for the T_c suppression for films deposited with a $PrBa_2Cu_3O_{7-y}$ template with Raman spectroscopy and found that the frequencies, especially of the 500 cm^{-1} phonon vibration, do not indicate any oxygen deficiency, but that the FWHM narrows with increasing deposition temperature of the film (the template being deposited at the same temperature for all the films), especially for the apical oxygen (the O(4) atom, compare Fig. 1.2) and the plane copper vibration modes. This

indicates that during the growth at lower temperatures, a very stable disorder is introduced among the chain oxygen and the apex oxygen. If the deposition temperature is raised, this disorder vanishes and consequently the T_c rises.

Another method is the so-called self-template method. In this case, a template of $YBa_2Cu_3O_{6+x}$ is deposited at a lower substrate temperature, again resulting in an *a*-axis film of reduced quality and then the temperature is raised. The template forces the film to remain in the *a*-axis orientation despite the higher temperature, but the higher deposition temperature results in better film characteristics. Hamet *et al.* [78] raised the temperature to that normally used to deposit *c*-axis oriented films without stopping the deposition, which seems to be the most common way. Ha *et al.* [79] used a self-template method, stopping the deposition between the deposition of the template layer and the $YBa_2Cu_3O_{6+x}$ film. Mahajan *et al.* [80], in a very thorough paper investigating the influence of several deposition parameters in sputtering using the self-template layer, found that stopping the deposition while raising the temperature did not change the T_c and ΔT_c for films deposited on MgO and $SrTiO_3$, but stopping the deposition while raising the temperature introduced *c*-axis and (110)-oriented grains in addition to the *a*-axis oriented grains for films deposited on MgO (and another perovskite phase which they mentioned, but could not identify). Yet if the deposition was not stopped during the raising of temperature, only *a*-axis oriented grains and the unidentified phase were observed. On the other hand, films deposited on $SrTiO_3$ and $NdGaO_3$ showed only *a*-axis oriented grains in both cases. They explain the results on MgO by comparing it to "the seeding process in crystal growth in which the growth of a crystal occurs by slow pulling of a seed crystal with the purity and properties of the resulting crystal depending on the pulling rate."

A question addressed in a paper by Kawamoto and Hirabayashi [81] is why the films grow with only the *a*-axis perpendicular to the substrate rather than the *b*-axis perpendicular to the substrate. The question is important, because it is related to oxygen ordering. For *a*-axis oriented grains, the Cu–O chains are parallel to the substrate, while for the *b*-axis oriented grains, the chains run perpendicular to the substrate surface. Their explanation considers the oxygen–deficient state in which the films are grown. During the subsequent oxygen loading, it is energetically preferable to form chains parallel to the surface, which corresponds to *a*-axis oriented material, because there are fewer terminations for the Cu–O chains than for chains running perpendicular to the substrate surface. Citing a paper by Ronay and Nordlander [82], who calculated the activation for the oxygen motion (energies of 1.7 and 1.6 eV are required for motion in the *a*- and *c*- directions respectively and no energy barrier in the *b*-direction) they conclude further that once the short Cu–O chains parallel to the surface have formed, they will grow very fast.

5.1 X-Ray and Resistance Studies on *a*-Axis Oriented Films

Before doing PAC experiments on *a*-axis oriented films, it was necessary to characterize their growth mode. Especially important is the effect of the substrate temperature and local oxygen pressure at deposition.

A series of films at decreasing substrate temperatures was grown, starting at 670 °C, which had proved to be the best temperature to grow high quality *c*-axis oriented films on $SrTiO_3$, all the way down to 570°C, which is 100°C lower. Fig. 5.1 shows the development of the $YBa_2Cu_3O_{6+x}$ (200) peak,

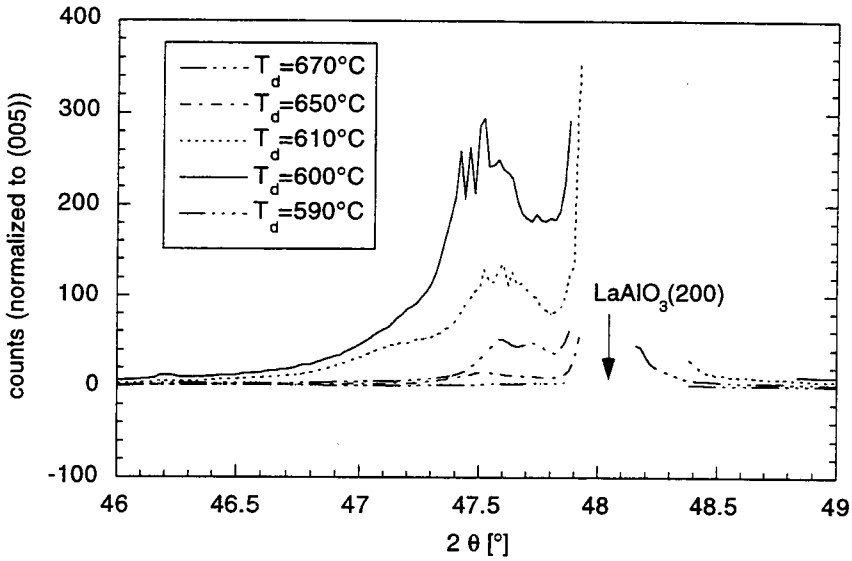

Fig. 5.1 Rise in the (200) peak of $YBa_2Cu_3O_7$ with decreasing deposition temperature. All films were deposited at 25% of 50sccm of oxygen (included is data from a film deposited at 590 °C, where the peak height decreases again). The x-ray data is normalized with respect to the (005) peak. The position of the $LaAlO_3$ (200) is indicated; the data are suppressed because substrate peaks cause the detector to overload.

which clearly increases with decreasing temperature until 600 °C, after which it decreases.

The θ-2θ scans taken at OSU, as well as pole-figures taken by Dr. Roberta Bigelow at Willamette University, were carefully checked for any evidence of *b*-axis oriented grains. If there are any *b*-axis oriented grains, they are below the detection limit of x-ray diffraction, which is usually around 5%. Table 5.4 shows that the separation of the (*n*00) and (0*n*0) peaks, caused by the orthorhombic distortion is at least 0.4°. The peaks should be very clearly resolved for $n = 3$ and $n = 4$ (the linewidth of the peaks is less than 1°, as shown in chapter 3).

n	$LaAlO_3$ (n00)	$YBa_2Cu_3O_7$ (n00)	$YBa_2Cu_3O_7$ (0n0)
1	23.444	23.258	22.833
2	47.949	47.549	46.643
3	75.107	74.416	72.859
4	108.714	107.469	104.703

Table 5.4. 2θ (in °) values for $LaAlO_3$ and *a*-axis and *b*-axis oriented $YBa_2Cu_3O_7$. $LaAlO_3$ has a lattice constant of 3.79Å, the *a*-axis of $YBa_2Cu_3O_7$ is 3.82Å, the *b*-axis of $YBa_2Cu_3O_7$ is 3.89Å.

It is difficult to quantify the ratio of *a*-axis to *c*-axis oriented grains from the x-ray diffraction spectrum, but it is useful to compare the maximum peak intensities of the (005) peak, representing the *c*-axis grains, and the (200) peak, representing the *a*-axis grains (Fig. 5.2). The ratio is used because the absolute number of counts is not fixed. Fig. 5.2 shows a maximum in the *a*-axis content at about 600 °C. Because the θ-values for the (*h*00) of $YBa_2Cu_3O_{7-\delta}$ and $LaAlO_3$ are very close together, as shown in Table 5.4 and Fig. 5.1, the substrate contributes significantly to the peak intensity of the (200) peak. Rocking curves on the (200) and (005) peak of the $YBa_2Cu_3O_7$ were performed to minimize the substrate interference. Because of the slightly different θ values required to bring the substrate and film into the diffraction condition (Table 5.4) the substrate will contribute only minimally, as seen in Fig. 5.3 Integrating the area under these curves and taking the ratio gives an estimate of the amount of material in each of the orientations.

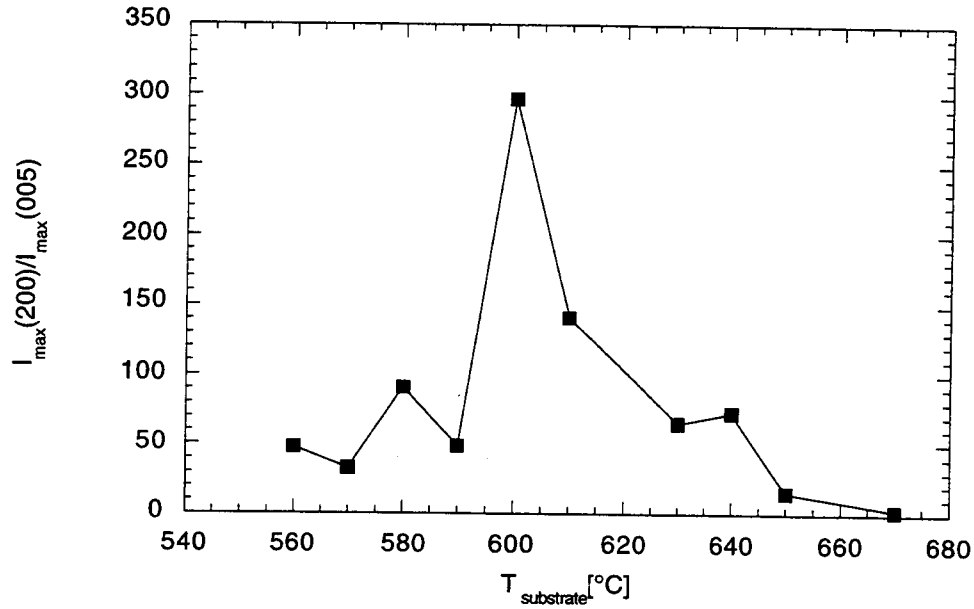

Fig. 5.2 Ratio of the maximum peak intensities of the (200) and (005) peaks. All films were deposited at 25% of 50 sccm of flowing oxygen, which is a local pressure at the substrate of 1.8×10^{-3} torr.

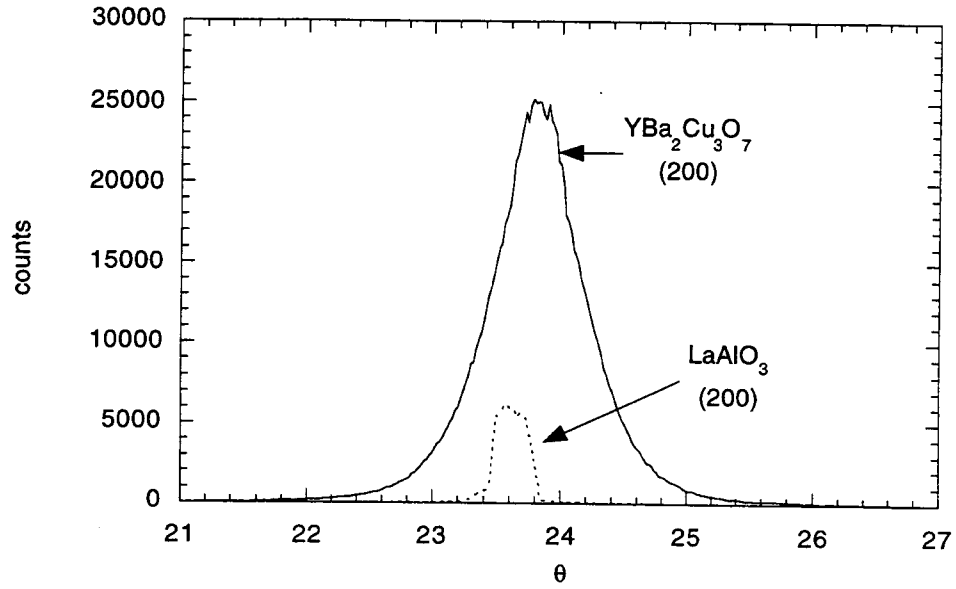

Fig. 5.3 Rocking curves of an *a*-axis $YBa_2Cu_3O_{6+x}$ film on a $LaAlO_3$ substrate and the $LaAlO_3$ alone. The diffractometer was set at $2\theta = 47.549°$ for both. The substrate curve was obtained by flipping the substrate over so that the film did not contribute. The film was deposited at 590 °C and 15% of 50 sccm.

The previous set of films was deposited at various substrate temperatures at 25% of 50 sccm of flowing oxygen during deposition, which corresponds to a pressure of 1.8 mtorr at the substrate (Fig. 5.4). During the deposition, oxygen is supplied at the substrate and therefore the local pressure at the substrate is significantly higher than the background pressure (typically $\approx 10^{-5}$ torr).

A similar investigation into the pressure dependence of the growth mode was carried out for films deposited at a temperature of 600 °C, the temperature of the maximum *a*-axis content found for films deposited at 25% of 50 sccm. The result is shown in Fig. 5.5, which indicates that the lower pressure of 1.1 mtorr at 600 °C optimizes *a*-axis growth.

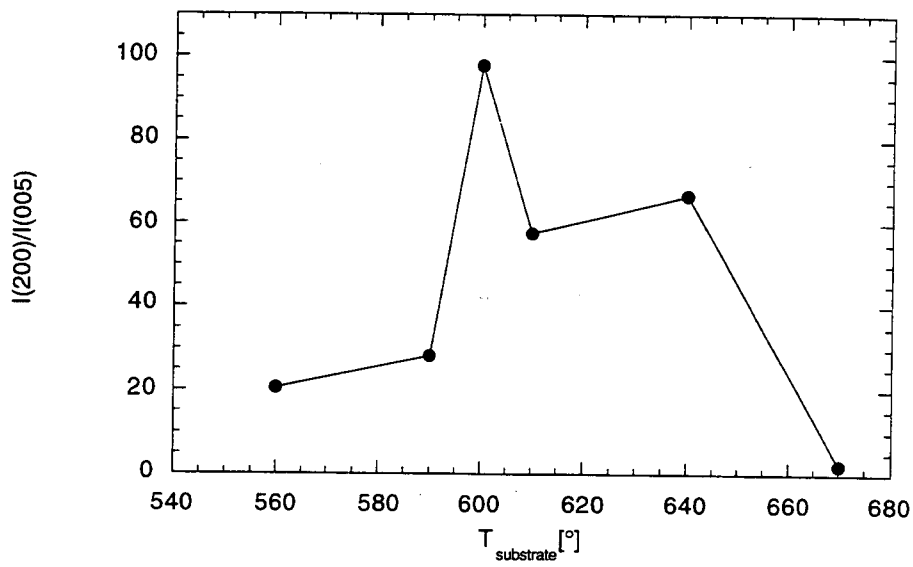

Fig. 5.4 Ratios of the integrated intensities of rocking curves on the (200) and (005) peaks. All films were deposited at 25% of 50 sccm of flowing oxygen. There is a maxium for a deposition temperature of 600 °C.

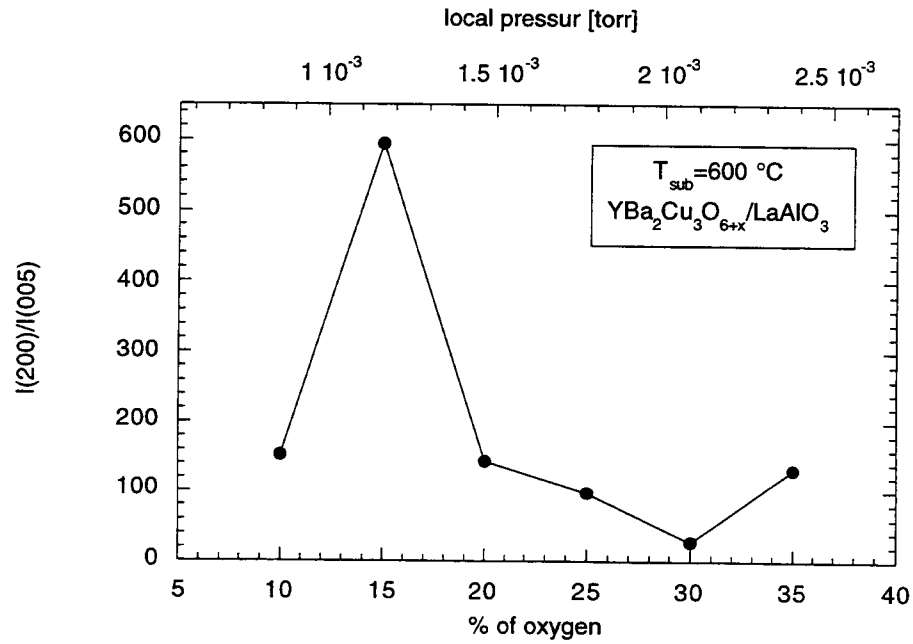

Fig. 5.5 Dependence of the ratio of the integrated intensities of the (200) and (005) peak (calculated from rocking curves) of $YBa_2Cu_3O_7$ on the pressure during deposition. All films were deposited at a substrate temperature of 600 °C.

The all-important question of T_c is addressed in Fig. 5.6, which shows some of the T_c's for a series of films, deposited at decreasing temperatures with an oxygen pressure of 25% of 50 sccm (1.8 mtorr). The slope flattens and for films deposited at relatively low deposition temperatures, the resistance rises before the films go through the transitions. The decrease in the transition temperature T_c and the increase in the width of the transition is illustrated in Fig. 5.7. Neither is surprising, because the films were grown without a template[15], which generally improves the crystallinity, as shown in the literature overview. In the literature, a reduced T_c is in general attributed either to disorder within the oxygen sublattice or to cation disorder, both of which are more likely to occur at reduced substrate temperature, which reduces diffusion in the newly deposited film.

[15] In our system, it is not practical to grow a template layer, because of the short deposition time. Shuttering the substrate, changing the substrate temperature, waiting for the heater to stabilize and than continuing the deposition requires more material in the boat, but the deposition rates, especially of the barium tend to be less stable if the boat is overfilled.

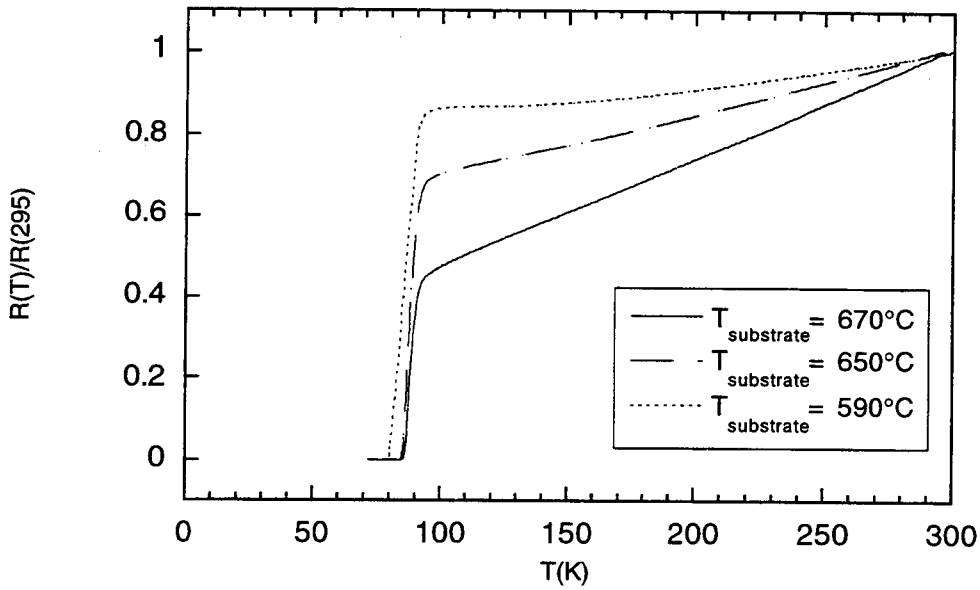

Fig. 5.6 Normalized resistance for several films grown at decreasing deposition temperatures with increasing *a*-axis content. The pressure during the deposition was 25% of 50 sccm. It is important to note that the slope and the general shape change, becoming increasingly flatter. This is especially important to note in comparison with the oxygen–deficient films.

Comparison of Fig. 5.7 and Fig. 5.8 shows that an optimum in one characteristic of the film does not necessarily mean that the other characteristics are optimized under the same conditions. Fig. 5.8 shows clearly that at the maximum *a*-axis content (15% of 50 sccm), the T_c is substantially reduced.

From Fig. 5.7, we see that T_c can be recovered by increasing the oxygen pressure at deposition. However the maximum *a*-axis concentration for this pressure is 6 times lower than for the pressure shown in Fig. 5.8.

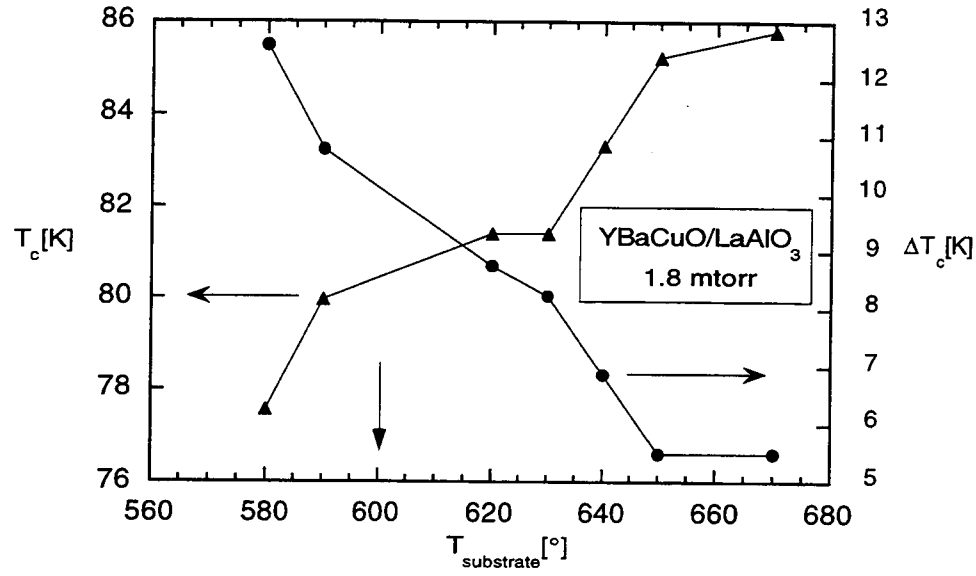

Fig. 5.7 Development of T_c and ΔT_c with decreasing substrate temperature. Both show clear evidence of increasing disorder, the T_c decreases and the ΔT_c increases with decreasing deposition temperature (films were deposited at 25% of 50 sccm (1.8 mtorr at substrate)). The vertical arrow indicates the temperature where a maximum in the amount of *a*-axis grains was found.

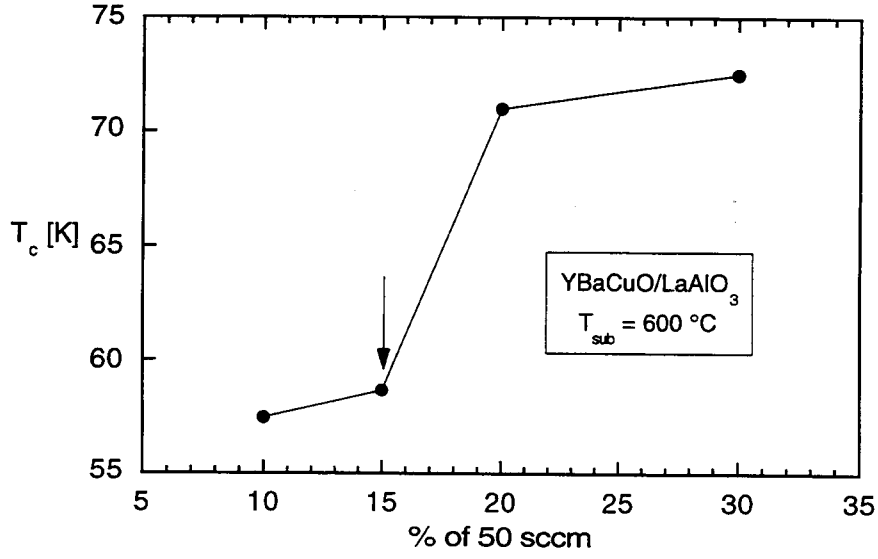

Fig. 5.8 Dependence of T_c on the oxygen pressure for films deposited at 600 °C. Fig. 5.5 shows that the maximum amount of *a*-axis oriented grains is for an oxygen pressure of 15% of 50 sccm, but for this value the T_c is significantly reduced.

5.2 Investigation of *a*-Axis Oriented Films with PAC

The preliminary investigation showed that it was possible to grow *a*-axis oriented films in our evaporation system. Several *a*-axis oriented films were made, with an oxygen content of $x \approx 7$ as well as $x \approx 6.25$. The fully oxygenated films were used to establish the direction of the electric field gradient in $YBa_2Cu_3O_7$, the $YBa_2Cu_3O_{6.25}$ films were grown to further investigate the tetragonal phase, especially because at that time the second site "mystery" had not been solved. Because of the known orientation of the electric field gradient for the tetragonal phase, they could also be used as

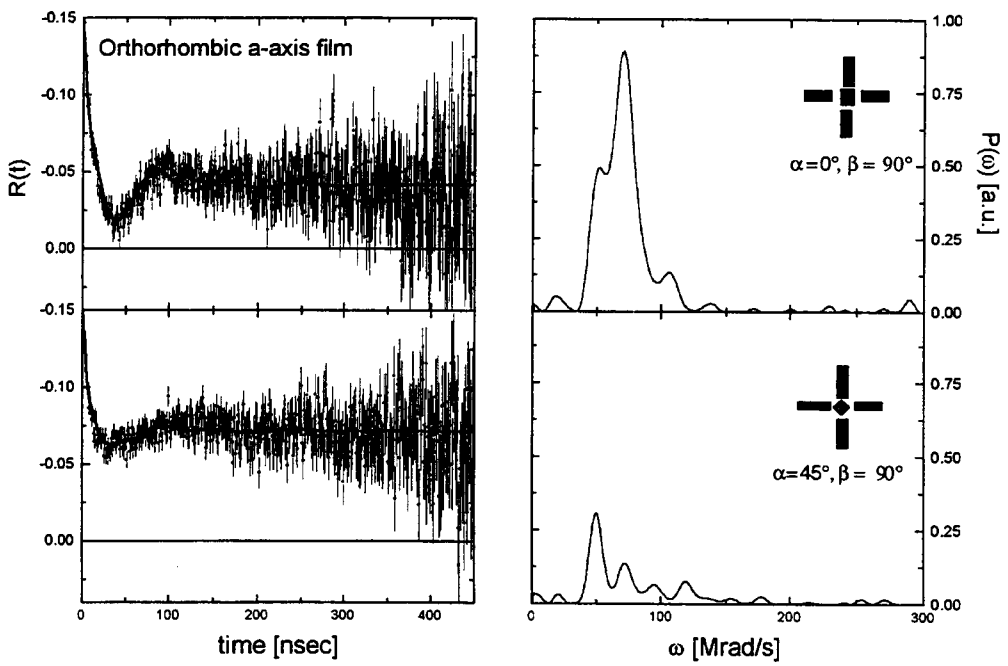

Fig. 5.9 $R(t)$ and Fourier transforms of an orthorhombic *a*-axis oriented $YBa_2Cu_3O_7$ film at room temperature. For a *c*-axis oriented film in the upper (α=0°, β=90°) orientation, ω_1 would have the higher amplitude and ω_2 would be suppressed. For the lower orientation (α=45°, β=90°), a *c*-axis oriented film would have ω_1 suppressed and ω_2 would have the higher amplitude.

another test that the films were *a*-axis oriented. (This proved to be the only use, because for some reason, the film became disordered in the PAC signal if annealed in oxygen at rather low temperatures (≈ 200 °C). Surprisingly they still showed x-ray peaks.) The PAC *a*-axis oriented films were grown at 580 °C, and an oxygen flow of 25% of 50 sccm, not quite at the optimum conditions shown earlier in this chapter.

Fig. 5.9 shows the typical PAC spectrum of an *a*-axis oriented orthorhombic $YBa_2Cu_3O_7$ film. In comparison to a *c*-axis oriented film (compare Fig. 4.7) one sees that for the same orientation of the film, ω_1 is suppressed in the *a*-axis case and ω_2 is suppressed in the *c*-axis case.

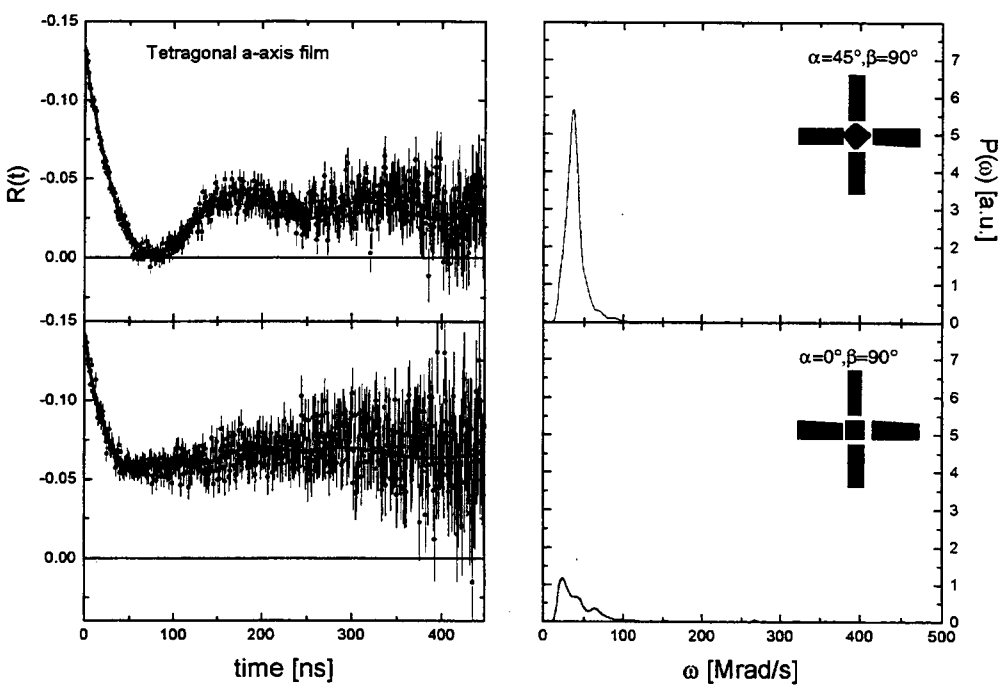

Fig. 5.10 $R(t)$ and Fourier transform of a tetragonal *a*-axis oriented $YBa_2Cu_3O_{6.25}$ film. For a tetragonal *c*-axis oriented $YBa_2Cu_3O_{6.25}$ film, these two spectra are nearly identical.

Fig. 5.10 shows the spectrum of a tetragonal *a*-axis oriented film with the plane of the film in the detector plane. These spectra very clearly show the difference between the *a*-axis and *c*-axis oriented films in this particular orientation. For a *c*-axis oriented films, these two spectra should be nearly identical, because the main axis of the electric field gradient is perpendicular to the detector and film plane and turning the film by 45° in the detector plane does not make a difference. For the *a*-axis oriented films, on the other hand, the main axis of the electric field gradient is in the film and detector plane. For $\alpha = 0°$, the main axis of the electric field gradient points into the detectors, while for $\alpha = 45°$, the main axis of the electric field gradient points between the detectors, so one expects to see a significant difference in the spectra.

The most important result from the *a*-axis films is that we finally could determine the complete orientation of the electric field gradient at the yttrium site. As predicted by Yu *et al.* [48], it points along the *b*-axis, with $V_{zz} = 2.1(1)\times10^{-7}$ V/cm^2 and an asymmetry $\eta = 0.5$. (The predicted values are $V_{zz} = 2.01\times10^{-7}$ V/cm^2 and $\eta = 0.43$.) This fit could only be obtained if a *b*-axis fraction of about 15%–20% was assumed, a number which was not confirmed by x-ray diffraction. These differences have not been resolved yet, but one educated guess can be based on the fact that x-ray diffraction and PAC measure on two very different length scales. PAC does not measure much farther than next–nearest neighbors (20Å to be generous), and very locally the structure could be *b*-axis oriented, maybe even induced due to the foreign ^{111}In atom (which is after all an impurity) but not more than a couple of unit cells in either direction. X-ray diffraction would not be able to see such small domains (it averages over at least 1000Å) and would only show the *a*-axis oriented material. The probe atom locally changing the structure from *a*-axis to *b*-axis

would also go a long way towards explaining the fairly high number of 20 %, because the probe atoms are in a layer only about 500Å thick (in a 2000Å thick film), but x-ray diffraction averages over the whole thickness of the film.

Chapter 6
Oxygen-Deficient Films

The investigation in this thesis was started by the fact that we could easily produce films with an oxygen content of ≈ 7 and with an oxygen content of 6.25. From our experiments using PAC we knew that in the case of $YBa_2Cu_3O_{7-\delta}$ the main axis of the electric field gradient was pointing along the *b*-axis with a frequency $\nu_Q = 39$ MHz, in the case of $YBa_2Cu_3O_{6.25}$ the main axis was pointing along the *c*-axis with a frequency $\nu_Q = 20$ MHz. Yet we did not know what happened in between this two values, for example in what way the frequency changes with respect to the oxygen content and for what oxygen content the orientation of the electric field gradient changes.

6.1 Investigation of Tetragonal $YBa_2Cu_3O_{6+x}$

The tetragonal phase of $YBa_2Cu_3O_{6+x}$ shows semiconducting behavior and not the superconducting behavior which is the hallmark of orthorhombic $YBa_2Cu_3O_{7-\delta}$. There are several good reasons for studying the tetragonal phase. The main reason is that films are deposited at high temperatures and low pressures. Low pressures are needed in order to use vacuum deposition techniques successfully, and it is common knowledge that in order to produce high quality thin films, high substrate temperatures during the deposition are needed. If the films are deposited on "cold" substrates, they are amorphous and a post-anneal at temperatures higher than 700 °C is required to induce crystallinity [83-85]. Low pressures and high temperatures put most of the vacuum deposition techniques into the region of the phase-diagram (Refs. [86] and [87]), where the material is tetragonal.

(The transition from tetragonal to orthorhombic is accomplished during a subsequent anneal in oxygen at lower temperatures, typically around 450 °C to 500 °C and higher pressures, typically around several torr to atmospheric pressure.) Learning more about the tetragonal phase by quenching the material right after the deposition can tell us more about the processes during the deposition and can help us improve the orthorhombic films.

6.2 Previous Work on Tetragonal $YBa_2Cu_3O_{6+x}$ Films

Because the tetragonal phase is not superconducting, it has met with less interest than the superconducting phase. One of its applications is in devices, where parts of a film are turned semiconducting in order to provide an insulating area in the devices [88]. This is accomplished by laser-heating or some other form of very localized heating. Li *et al.* [89] investigated the influence of laser writing power densities and scanning speed as well as different atmospheres (N_2 or O_2) on slightly oxygen–deficient films ($x \approx 6.87$) and found that the oxygen content increased or decreased, depending on how high a temperature the film reached during the annealing and how fast it cooled through the optimum annealing temperature region of 400 °C to 500 °C.

As an interesting aside, some researchers also have sputter–deposited a superconducting ($\delta \approx 0$) *tetragonal* phase of $YBa_2Cu_3O_{7-\delta}$ [90]. They claim that due to the presence of activated oxygen species, the oxygen content of their newly deposited films is higher than generally found. The tetragonal films are quenched from the deposition temperature of 750 °C at a rate of 220 °C/min at a pressure of 1 bar [91]. These superconducting tetragonal

$YBa_2Cu_3O_7$ thin films are very disordered, especially with respect to the cations.

In addition, work has been done on the formation of secondary phases and the decomposition of $YBa_2Cu_3O_{6+x}$. This is important, because some of the deposition techniques use conditions which are in a region of the phase-diagram where $YBa_2Cu_3O_{6+x}$ is unstable [15]. It is therefore important whether and under what circumstances, any secondary phases form and if they do, whether they are detectable in the orthorhombic phase and by what techniques. Eibl and Roas [92] produced laser ablated films at reduced oxygen pressures (10^{-2} mbar) and found $BaCu_2O_2$, Y_2O_3, Cu_2O_x and Y_2BaCuO_{5-x} in TEM. Interestingly, they never found $Y_2Cu_2O_5$ under these conditions. Secondary phases and impurities are important, because they might provide pinning sites, therefore improving characteristics like J_c, as pointed out by Tinkham [93], on the other hand, disorder is detrimental to the T_c. The mechanisms of formation have to be properly understood to tailor the material to ones needs.

6.3 Starting Point for the Investigation

The starting point for the investigations in this thesis was some very interesting data collected by Dr. Dennis Tom and Dr. Roland Platzer [27]. Their PAC spectra on tetragonal $YBa_2Cu_3O_{6.25}$ contained the signatures of the ^{111}In atoms experiencing two different well–defined electric field gradients, also called sites. I will refer to the site already identified as the signal from the $YBa_2Cu_3O_{6+x}$ material as the A site and this new site as the B site. The B site is remarkable for several reasons.

1) It was never seen in a spectrum of an orthorhombic film, regardless of whether that film had been grown orthorhombic or whether it had been grown tetragonal (and had shown the second site), and annealed ex–situ in oxygen to go through the phase transition. Tetragonal films showed varying degrees of the B site: its appearance was clearly very sensitive to the exact growth and in–situ anneal conditions.
2) Because of the tetragonal symmetry of $YBa_2Cu_3O_{6+x}$, the material is expected to have an asymmetry of $\eta = 0$. Yet the A site has a surprisingly high asymmetry of $\eta \approx 0.4$, but the second site has the correct asymmetry of $\eta = 0$.
3) The main axis of the field gradient of the B site did not point along any of the major axes of the $YBa_2Cu_3O_{6+x}$, but was at an angle of 22° with the c-axis of the $YBa_2Cu_3O_{6+x}$.

Fig. 4.7 shows a typical orthorhombic spectrum where only one site is seen. The same figure also shows a tetragonal spectrum without the B site. Fig. 6.1 shows two tetragonal spectrum where the B site can be very clearly seen. These three tetragonal spectra point to strong dependence of the

	ν_Q [MHz]	η
A site ($YBa_2Cu_3O_{6.25}$)	20(1)	0.40(5)
B site	133(1)	0

Table 6.5 Frequency and asymmetry of the A and B sites.

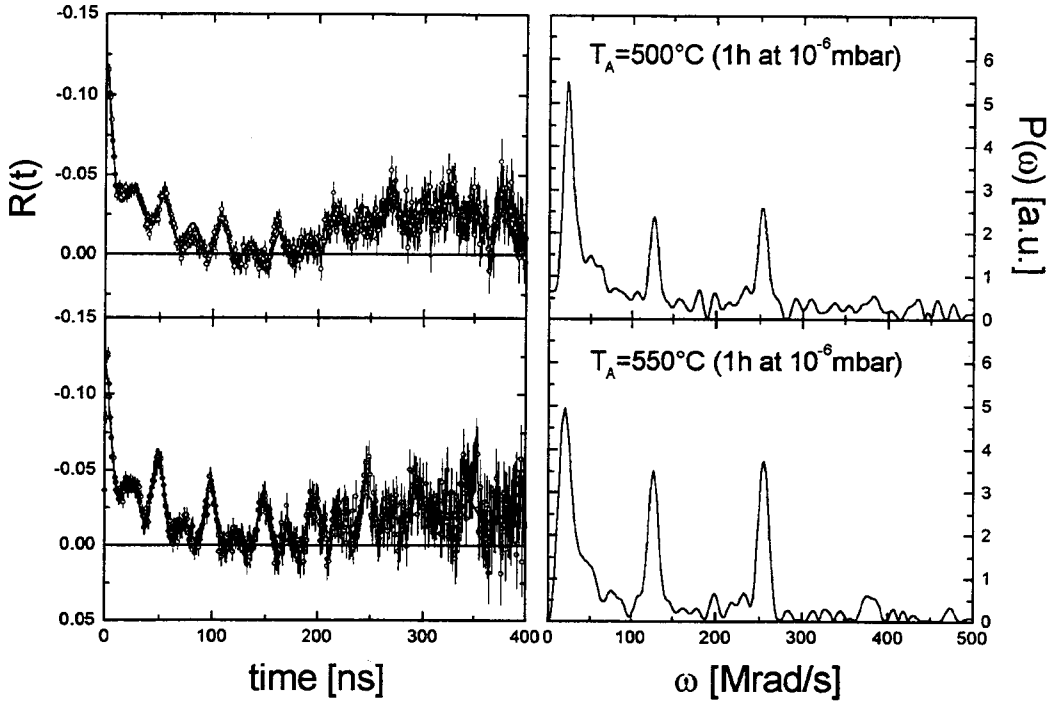

Fig. 6.1 $R(t)$ and Fourier transform of two tetragonal films annealed at 500 °C and 550 °C. These two spectra clearly show the influence of the annealing conditions on the amount of B site formed.

amount of B site formed on the deposition and anneal conditions, something which is not yet well understood.

At this time, the origin of the B site was unknown. One possible explanation was that it could be an impurity formed during the deposition or right afterwards, when the oxygen was removed and the films were cooled down in vacuum. Another explanation, which held a lot of appeal, was that the B site was the signal of $YBa_2Cu_3O_6$, with exactly 6 oxygen atoms per unit cell. Raman studies of the films had shown that their oxygen content was approximately 6.25 and that the length of the anneal did not make a difference in the oxygen content. It was speculated that nanometer–sized (at least) regions of $YBa_2Cu_3O_6$ existed within $YBa_2Cu_3O_{6.25}$ and that the PAC

technique might have detected this separation. (Other techniques, less local, would not have detected this.) This explanation is consistent with the observed asymmetry parameter, because the $YBa_2Cu_3O_6$ phase is expected to have $\eta = 0$, with no oxygen atoms in the basal plane and therefore no preferred direction, and is also consistent with the disappearance of the B site on oxygenation, but it ultimately proved incorrect as will be seen later.

6.4 X-ray Studies on Tetragonal Films

In order to solve the second site mystery, a very careful x-ray study of the tetragonal films was undertaken. Films which had been annealed in vacuum for different amounts of time as well as quenched right after the deposition or ramped down from the deposition temperature at a rate of 10°/min were used.

Careful investigation of the spectra showed two sets of very small impurity peaks in the vicinity of the (004) and the (008) peaks, which themselves are very small peaks in the x-ray spectrum of $YBa_2Cu_3O_{7-\delta}$. Fig. 6.2 shows examples of the additional peaks for different kind of anneals, all of them at a pressure of about 10^{-7} torr. Except for the fact that the additional peaks are in each of the spectra, there does not seem to be a particular pattern to their peak height. This may mean that their formation is very sensitive to the exact substrate temperature and oxygen pressure during deposition, or some other possible factors like the stability of the deposition rate or the quality of substrate surface.

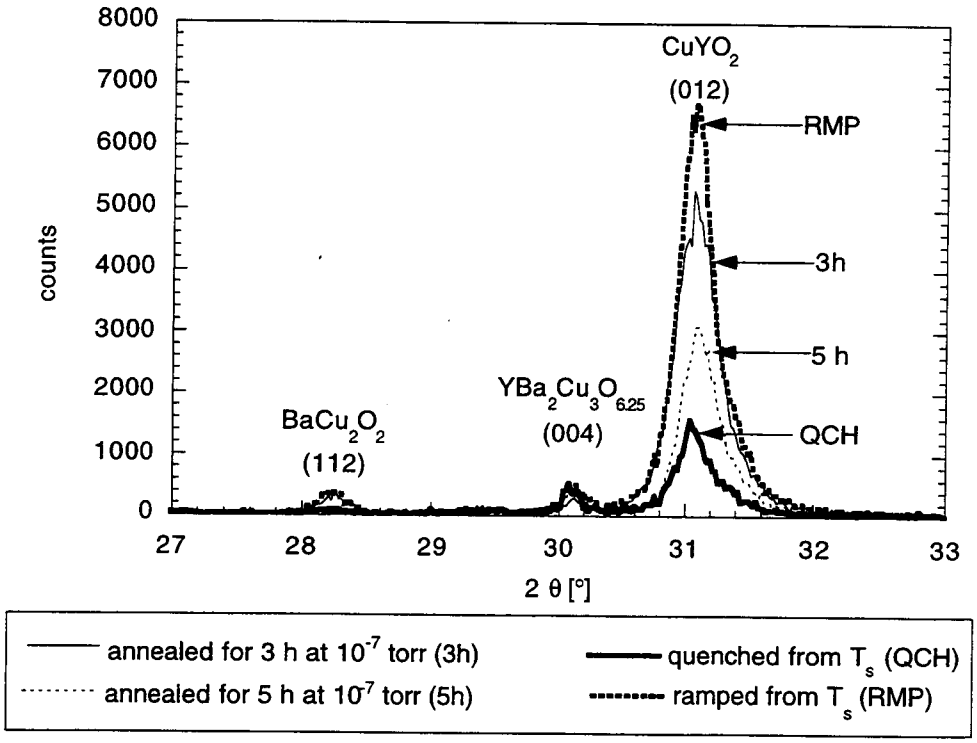

Fig. 6.2 X-ray spectra of $YBa_2Cu_3O_{6.25}$ films showing the two impurity peaks near the (004) of $YBa_2Cu_3O_{6.25}$. The ramp rate for the "ramped" film was 10 °C/min, the two annealed films were annealed at 500 °C for the times indicated. All anneals were in a vacuum of $\approx 10^{-7}$ torr. The spectra are not normalized, but all have about the same peak–height for the $YBa_2Cu_3O_{6.25}$ (004) peak.

Identification of secondary phases in an x-ray spectra is an art-form in itself. In an oriented film, most of the reflections are missing and the reflections that are there are not necessarily in the ratios given in the tables, if they belong to different sets of planes. The identification of secondary phases in $YBa_2Cu_3O_{6+x}$ is further complicated by the fact that there are 4 elements, which can form a large number of possible secondary phases. Table 6.6 gives the 2θ values and the accompanying *d* values for the impurity peaks observed in several different samples.

6.5 Identification of the Second Site

For the identification, it was assumed that the two sets of peaks belong to different orders of reflection from the same set of planes. This helped to eliminate most of the possible candidates from a search performed on the set of peaks around the (004) peak and the (008) peak separately and in the end left only two possibilities, $CuYO_2$ in the (012) and (024) orientation, corresponding to peak #2 and #4 in Table 6.6 and $BaCu_2O_2$ in the (112) and (224) orientation, corresponding to peak #1 and #3 in Table 6.6 (JCPDS files #39-244 [94] and #39-245 [95]).

The identification of two impurities in x-ray diffraction must be reconciled with the appearance of only one impurity in the PAC spectra. In all the research done in Dr. Gardner's group [62], [55] it was shown repeatedly that ^{111}In substitutes readily for Y, preferring Y-rich phases. One of the possible explanations is that both the indium and the yttrium have the same valence 3^+ and they are also very close in ionic radius. Our x-ray investigation now found two impurities, one containing yttrium, the second containing no yttrium at all. We speculate that the In does not substitute in $BaCu_2O_2$ at all,

	#1 [°]	#1 [Å]	#2 [°]	#2 [Å]	#3 [°]	#3 [Å]	#4 [°]	#4 [Å]
RMP	28.22	3.159	31.07	2.875	61.11	1.579	64.83	1.436
QCH	28.24	3.156	31.05	2.877	61.04	1.578	62.50	1.437
3 h	28.24	3.156	31.07	2.875	61.04	1.578	62.55	1.437
5 h	28.26	3.154	31.10	2.872	61.22	1.578	62.53	1.436

Table 6.6 2θ values (in °) and the calculated *d*-values (in Å) of the impurity peaks for tetragonal $YBa_2Cu_3O_{6.25}$ films subjected to different post-deposition in-situ anneals. The names are explained in Fig. 6.2. Ref. [94] gives d=2.873 Å for the (012) peak of $CuYO_2$ and 1.436 Å for the (024), Ref. [95] finds the (112) peak of $BaCu_2O_2$ at 3.155 Å and the (224) peak at 1.578 Å.

or that it substitutes at all of the many sites in $BaCu_2O_2$, thus diluting the signal from any one site. Because PAC needs about 5% of the probe to be in one site to identify the signal, if the indium substitutes in all possible sites, it might not get over the detection limit for any single site and therefore be part of the noise.

After having identified $CuYO_2$ as a possible candidate for the B site, does our PAC data agree with what is known about $CuYO_2$? According to Attili *et al.* [60] it does so very well. They found a ν_Q of 136 MHz, which agrees with our measured data of 133 MHz and which makes the identification more plausible.

As an aside, there are two different sets of data for the x-ray spectra of $CuYO_2$. As I have just shown, we can get an excellent agreement with one set of published data [94], especially with respect to the orientation and confirm it with PAC, but the second set of published data [96] does not give as good an agreement in the 2θ values and it assigns them to different *h, k, l* values. Interestingly, this paper is used by Marshall *et al.* [97] to identify $CuYO_2$ in their films deposited at low oxygen pressures with a different orientation than in ours.

Furthermore, because $CuYO_2$ is rhombohedral, the field-gradient can be assumed to point along the *c*-axis, with the same reasoning as in the case of the tetragonal $YBa_2Cu_3O_6$, because there is nothing to distinguish the a_1– and a_2–axis, but the *c*-axis is different from these axes. With this assumption, the measured orientation of the field gradient (an angle of 22 ° of the main axis of the electric field gradient with the *c*-axis of the $YBa_2Cu_3O_{6.25}$) agrees with the orientation seen in the x-ray spectra.

Additional evidence that the B site signal is from $CuYO_2$ is that if a B site signal is observed in the PAC spectrum, $CuYO_2$ is observed in the θ-2θ

scan. As already mentioned, the B site signal was never observed in orthorhombic films and likewise was $CuYO_2$ never seen in θ-2θ spectra taken on orthorhombic films. Furthermore, one tetragonal film with a B site was annealed in flowing argon and up to 500 °C, the fraction of the B site remained constant. At 600 °C and higher temperatures the B site disappeared from the spectrum. After cooling the film in flowing argon and taken a θ-2θ spectrum of it, no $CuYO_2$ peaks were found in the spectrum.

Pressure–temperature phase diagrams are widely used to ascertain which impurity phases are likely to appear in a material, but for the most part are done on bulk samples and in air at temperatures higher (> 800 °C) than what is used in our deposition system (< 700 °C). These phase diagrams are used by researchers trying to grow crystals from a melt and are therefore interested in the liquid phases. Yet it is surprising how little is known about the phase equilibrium at reduced oxygen pressures and lower temperatures, characteristic of typical thin film deposition conditions. Ahn *et al.* [98] investigated the phase diagram of $YBa_2Cu_3O_{6+x}$ at 850 °C and reduced pressures and found that CuO and $BaCuO_2$ are no longer stable in contact with $YBa_2Cu_3O_{6+x}$, but that $BaCu_2O_2$ becomes stable in contact with $YBa_2Cu_3O_{6+x}$ at low oxygen pressure, appearing first at a partial pressure of oxygen of 3.0×10^{-3} atm (≈ 20 torr). $BaCu_2O_2$ does not exist along the BaO–CuO pseudobinary at temperatures between 900 °C and 1000 °C in air [99]. Based on the appearance of different oxides at reduced oxygen pressures for the Cu–Ba–O system, Beyers and Ahn [100] suggest either a $YBa_2Cu_3O_{6+x}$–$CuYO_2$ tie-line at low pressures and temperature or they suggest that in off–stoichiometry films $CuYO_2$ nucleates and grows faster than the Y_2BaCuO_5 and Cu_2O expected from the studies done in air at high temperatures. The faster nucleation is supported by the fact that the $CuYO_2$ grows highly oriented, reported by

Marshall *et al.* [97] as well as in this thesis, even if the orientations do not agree. Pankajavalli and Sreedharan [101] investigated the high temperature stability of $CuYO_2$ with oxide electrolyte e.m.f. measurements and found it marginally stable with respect to dissociation into constituent binary oxides over the range from room temperature to 1400 K. Konetzki and Schmid–Fetzer [102], using oxygen coulometric titration measurements in the Y–Cu–O found $CuYO_2$ to be metastable and forming rather easily if the partial pressure of oxygen is reduced. They almost sound annoyed at it, because it forms rather easily, but the decomposition into the binary oxides is very sluggish, meaning once it formed, it stayed around, even though it is only metastable. As a last point, the Cu in both $BaCu_2O_2$ and $CuYO_2$ is monovalent, which makes sense under the reducing conditions of a very "reduced" oxygen pressure of less than 10^{-7} torr.

All the above confirms that $CuYO_2$ can and should form under conditions of reduced oxygen pressures and high temperatures. Further evidence for this was provided by the PAC spectra on the films with reduced oxygen content, where in some of them the signal of $CuYO_2$ appeared, even though the annealing conditions were by far not as extreme as for the tetragonal films (temperatures not above 600 °C and pressures greater than 10^{-4} torr (at 400 °C), at 600 °C, the pressures were even higher).

6.6 Oxygen–Deficient $YBa_2Cu_3O_{6+x}$: Examples from Literature

As already pointed out in chapter 1, the oxygen content plays a crucial role with respect to the characteristics of $YBa_2Cu_3O_{6+x}$. The introductory part in Chapter 1 was concerned with the differences between crystals and films,

especially pointing out that results cannot be easily carried over because of the inherent differences in order between crystals and films. In this chapter I look at some of the properties of oxygen–deficient $YBa_2Cu_3O_{6+x}$. Chapter 1 illustrated the influence of the oxygen content on the T_c and the *c*-axis length. Several other properties have been investigated with respect to the oxygen content.

Cochrane *et al.* [103] measured the Seebeck coefficient in oxygen–deficient polycrystalline $YBa_2Cu_3O_{6+x}$ samples and found that for oxygen contents $7-\delta < 6.95$ the carriers are positive (holes) but for very high oxygen contents $7-\delta > 6.95$ the carriers are negative (electrons).

Ludwig *et al.* [104] found an increase in the London penetration depth λ_L from 175 nm for a $YBa_2Cu_3O_{6.95}$ film to 380 nm for a $YBa_2Cu_3O_{6.55}$ film. They also measured the plasma frequency and found it to decrease from 9100 cm^{-1} for the $YBa_2Cu_3O_{6.95}$ film to 4200 cm^{-1} for the $YBa_2Cu_3O_{6.55}$ film.

Fietz *et al.* [105] investigated the influence of pressure on the T_c. They investigated the change in T_c for polycrystalline and single crystal samples stored at room temperature and for samples stored at 100 K. For both temperatures they found a peak in dT_c/dp at an oxygen content of 6.7. In addition the samples stored at 298 K, with the lowest oxygen content being 6.4, show an decreasing dT_c/dp with increasing oxygen content. They explain their results with two different effects; one is oxygen ordering within the whole structure, facilitated by the increased pressure; the other is changing distances between the oxygen chains and planes due to the applied pressure. Because essentially no oxygen motion occurs at 100 K, they use their results at this temperature to differentiate between the two different effects for the 298 K results.

6.7 Early Results: Anneals in Evaporator

To control the oxygen content in our films, two approaches were tried. The first series of experiments was done in the deposition chamber itself, using two different methods. For one set, after the deposition the pressure in the chamber was brought up to the desired values (pressures of 1.5 torr, 1.5×10^{-1} torr, 7.7×10^{-1} torr, and 1.5×10^{-2} torr were used), and then the temperature was lowered to the anneal temperature of 450 °C for 1 hour. Fig. 6.3 shows how the T_c and ΔT_c change with decreasing anneal pressure. The film annealed with the chamber backfilled to a pressure of 1.5×10^{-2} torr did not have a transition at all, but showed semiconducting behavior.

During the anneal, the chamber pressure dropped significantly from the original pressure (for the lower pressures by more than an order of

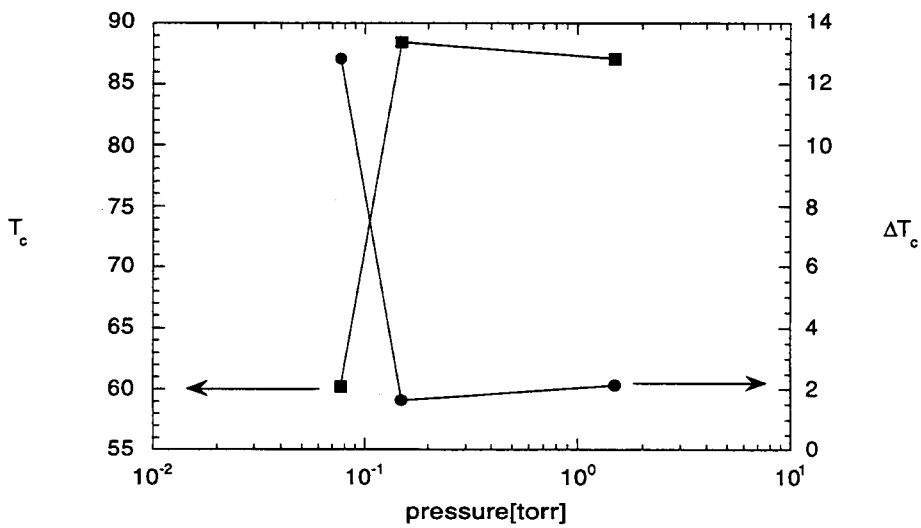

Fig. 6.3 Development of the T_c and ΔT_c for films annealed at different pressures, if the pressure is adjusted only once. The pressure was adjusted while the films were still at the deposition temperature, then the films were ramped down to the anneal temperature of 450 °C with no further adjustment to the pressure. Films annealed at lower pressures had no transition temperature.

magnitude). A second set of films was prepared with the pressure during the initial cool down and anneal adjusted to stay at the desired value. For these films, pressures of 15 torr, 1.5 torr, 1.5×10^{-1} torr, 1.5×10^{-2} torr, 7×10^{-3} torr and 1.5×10^{-3} torr were chosen. Fig. 6.4 shows how the T_c and ΔT_c change with decreasing pressure. The transition width decreases by more than a factor of two and the T_c is much improved for the higher pressures. For the two lowest anneal pressures, the films showed semiconducting behavior. (As an interesting aside, the film annealed at 7×10^{-3} torr was measured right after the deposition and showed a fairly high T_c of 87.8 K and a ΔT_c of 3 K. Because it did not look quite like a fully oxygenated film, but was speckled and brownish instead of solidly black, the same film was remeasured a couple of days later and then showed semiconducting behavior).

What can be learned from these two sets is that a surprisingly low anneal pressure of 10^{-2} torr is enough to get a decent T_c. Many published

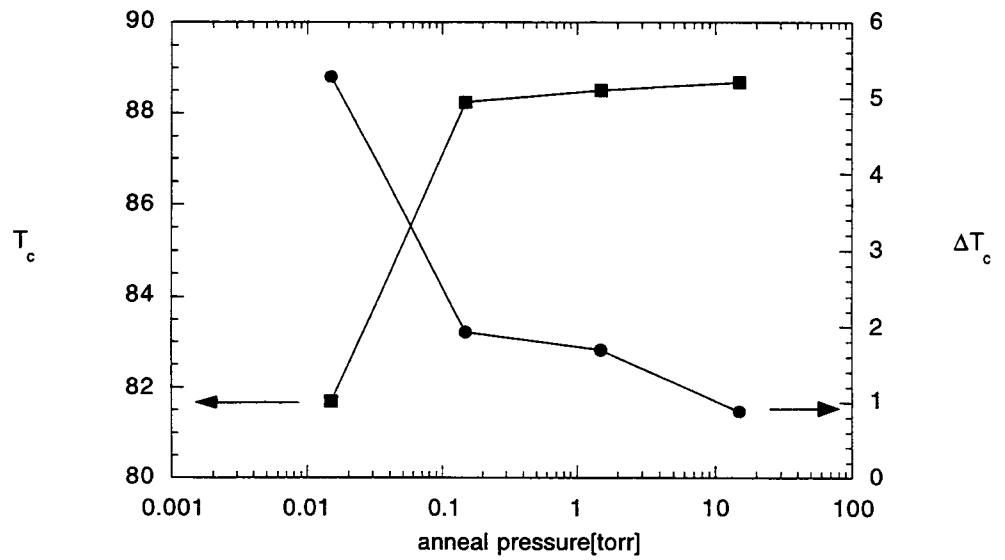

Fig. 6.4 Development of T_c and ΔT_c if the pressure is kept constant during the cool-down and the anneal. For lower anneal pressures, the films did not have a superconducting transition.

papers report that the chambers are backfilled to atmospheric pressure for the post deposition anneal. In both sets, the films annealed at 1.5×10^{-1} torr still had a T_c of ≈ 88 K. The most interesting region with $T_c \approx 60$ K is not very easy to reach and a T_c of 60 K was reached only in the anneal which felt less controlled. Furthermore, it was hard to control the pressure precisely, due to the large volume of the chamber (84000 cm^3) and the oxygen inlet and the pressure gauge being far apart in the chamber. This was especially true for anneal pressures between 10^{-2} torr (resulting in a film with a T_c of 81.7 K) and 10^{-3} torr (resulting in a film with semiconducting behavior), which can be deduced as the region one should be able to reach all the intermediate T_c values. In addition, I was hesitant to use the cryo-pump to adjust the pressure downward, for example to follow the proposed phase lines by Gallangher [28], because either the pump might pump too much, but cannot be throttled in the current set–up, or a large influx of oxygen might overburden the pump.

Therefore a system, described in detail in section 2.5.1, was designed, according to some suggestions in the literature [11], [12]. This system has a much smaller volume of 4277 cm^3 (about 5% of the evaporator volume). Both references make a point about bulk material in the vicinity of the sample. Ye and Nakamura [14] used it to prevent the film from becoming contaminated with impurities in the gas flow, but also remarks that if they tried to take out as much oxygen as possible, the films would decompose without the bulk material. Co-evaporation is messy, because it evaporates the metals not just on the substrate, but everywhere within the chamber, so some bulk is close to the sample, but in a very uncontrolled way. In our new system, a pellet of bulk $YBa_2Cu_3O_7$ can be put right next to the film, giving one more control about the amount and quality. Because of its much larger volume, the pellet helps stabilize the oxygen content. Also taking the data

presented in Ref. [61], which shows significant barium loss at high temperatures, the pellet with its much greater barium content might keep the barium partial pressure high enough to keep the film from decomposing. From data presented later in this chapter it can be inferred that whatever it does, the pellet works better.

6.8 Results from the New System

The new system was very successful from the start and provided us with means to reach T_c's down to 30 K, with values in between, exactly what we had hoped to achieve.

The procedure is explained in more detail in section 2.5.2 and is based on a phase diagram published in Ref. [28] and reproduced in Fig. 2.1, and gives the pressure–temperature phase lines needed to achieve oxygen contents between 6.2 and 6.7. A series of anneals was carried out, from a nominal oxygen content of 6.4 to 6.8. All anneals included an annealing step at 600 °C, except for the 6.8 film, which was done at 550 °C (doing it at higher temperatures would have required overpressurizing the system). A second annealing step was done at 450 °C, all the time staying on the phase line [28]. Afterwards, the samples were cooled down to 400 °C, still staying on the phase line and then quenched by pulling out of the furnace. Due to some technical difficulties with the cryogens, we were not able to see the resistive transition in the 6.6 and 6.8 film, but in each case the onset of the transition was observed and a rough guess for the T_c for the 6.6 film would be between 34 K and 50 K and for the 6.8 film between 68 K and 75 K. The 6.7 film has a T_c of 52.45 K. What is really remarkable about the resistance curves is the fact that they decrease almost linearly in resistance with a slope of almost 3 until they

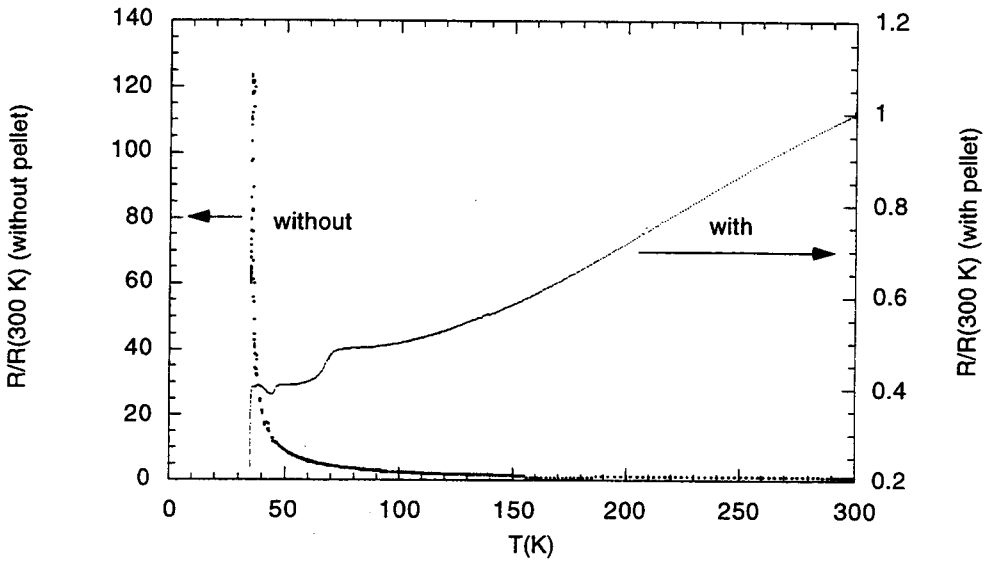

Fig. 6.5 Resistance of two films annealed on the 6.6 phase line, one with bulk $YBa_2Cu_3O_7$, the other with no bulk material in the vicinity. The structure in the resistance of the "with pellet" film was repeatable during the measurement itself, but might be an artifact of some measurement problems. Due to contact and probe problems, the resistance measurement could not be repeated after thermal cycling.

start going through the transition (Fig. 6.5), unlike the *a*-axis films where the slope flattened, and sometimes the resistance started to rise again with decreasing temperature before finally going through the transition.

To check for reproducibility, two 6.7 anneals on different films were carried out. For these two films, the T_c's matched within 0.5 K and the change in *c*-axis length matched within 0.01 Å, which points towards excellent reproducibility. Much to our surprise, this reproducibility was not evidenced in the PAC films, a nominal 6.7 anneal gave a T_c of 37.39 K for HTC 32 and of 47 K for HTC 34. But these films had suppressed T_c after the deposition, and therefore the widely different T_c might be less a sign of non–reproducibility of

the annealing system and more an indication of problems during the deposition.

Because the literature stresses the importance of $YBa_2Cu_3O_7$ bulk in the vicinity, one anneal (nominally 6.6) was done without any bulk. Even though the anneal was otherwise identical to the same anneal with bulk material, the electrical behavior was very different. The "bulk" film showed a transition, while "no-bulk" film showed semiconducting behavior, clearly evident in Fig. 6.5. At the same time, the *c*-axis length for the "no-bulk" 6.6 film is 11.86Å, while the *c*-axis length for the "with bulk" film is 11.84 Å, a difference which is significant and which indicates together with the resistance behavior that the oxygen content is lower than warranted by the anneal.

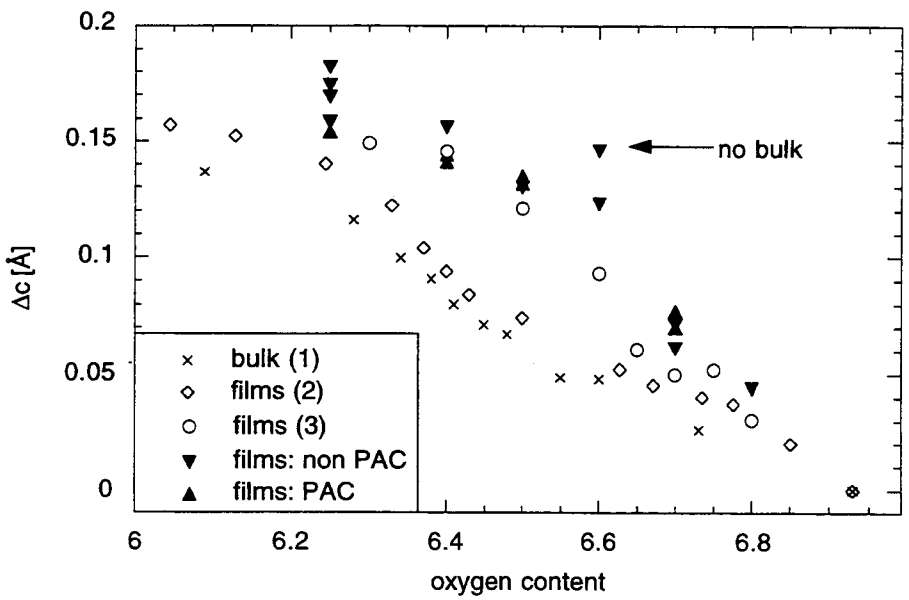

Fig. 6.6 Change in *c*-axis length for PAC and non-PAC films and comparison to published values. (1) is from Ref. [5], (2) is from Ref. [14], (3) is from Ref. [12]. (1) and (2) match very well, as does our data with (3), but they do not match with each other. The PAC and non–PAC match also, which is important because the non PAC film underwent only one anneal, while the PAC films were subjected to several.

The oxygen content of the films is not easily established. We have access to two basic methods to determine the oxygen content: the *c*-axis length, especially the change in the length, and for films above a certain oxygen content, the transition temperature. The high temperature resistance R(T)/R(300K) also appears to be systematically dependent on oxygen content, but we have yet to investigate it fully.

Fig. 6.7 plots the transition temperature vs the nominal oxygen content (as determined by the anneal conditions) and compares it to published data [12], [14]. The T_c vs oxygen content curve published by Ye and Nakamura [14] is very close to the curves published for bulk material and crystals, and in particular shows the 60–K plateau so characteristic of bulk $YBa_2Cu_3O_{6+x}$, but seldom seen in films. The curve of Ref. [12] has a very different behavior, namely showing no evidence of a plateau. Our data falls in between these two curves. Osquiguil *et al.* [12] in their paper are very careful about calling their

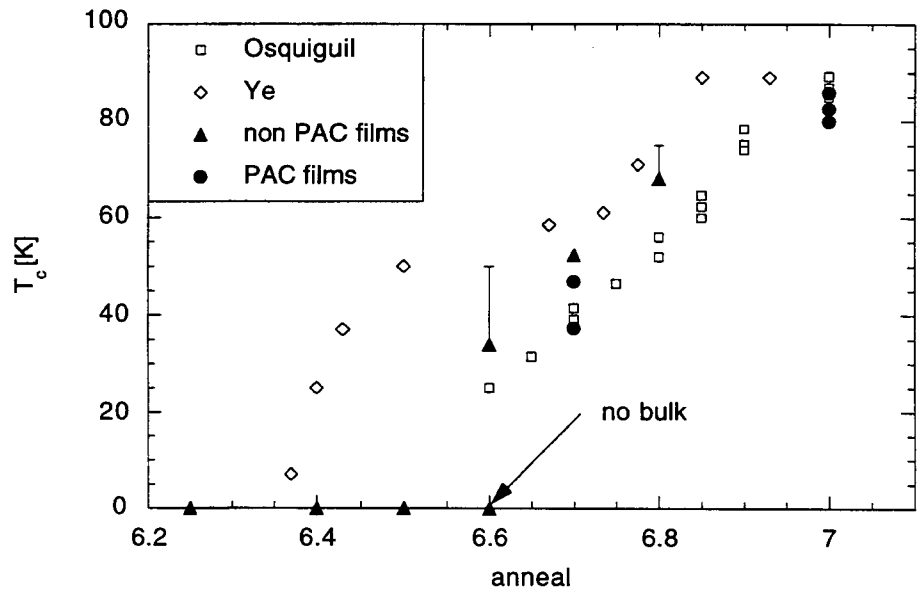

Fig. 6.7 T_c for our oxygen–deficient $YBa_2Cu_3O_{6+x}$ films compared to published data. Our films fall between the two curves.

oxygen content "nominal", and the suppressed T_c could indicate that the true oxygen content might be lower than that suggested by the anneal.

More evidence for this is shown in Fig. 6.6. This graph plots the change in *c*-axis length vs the oxygen content for powders [5] and films [12], [14]. The change in *c*-axis length (as opposed to the absolute *c*-axis length) was chosen to account for the generally elongated *c*-axis length in films, which can be attributed to several factors, including cation disorder. Because it is unlikely that our anneals at 600 °C changed the amount of cation disorder [106], the contribution of the cation disorder to the elongation of the *c*-axis length should be the same at any oxygen content.

Two important points are to be made about Fig. 6.6. Even though the films made by Ye [14] seem to be very well equilibrated, judging from the T_c vs oxygen content curve, the change in *c*-axis length is slightly larger for films than for the crystal data, again a sign that films are more disordered and strained in general. The more important point is that while our data matches very well for the oxygen content of 6.25 and for the 6.8 and higher, for the range between 6.4 and 6.7 the curves do not match at all, but the change is always larger, indicating again less oxygen in the material than what should be in there according to the anneal. This deviation seems to depend on the anneal itself and not the processing history, because the non-PAC films usually were subjected to only one anneal, while the PAC films were annealed several times without reoxygenation in between the different anneals. Interestingly, the data taken by Osquiguil *et al.* [12] matches our data fairly well, except perhaps for the 6.6 point, but even at this point their data is clearly deviating from the published data by Jorgensen *et al.* [5] and Ye and Nakamura [14]. At this point there is no good explanation for the differences, especially because the anneal we used was closer to the method used by Ye

than Osquiguil, who surrounded the film completely with bulk material, while Ye and we only had the bulk material in the vicinity. Osquiguil considered the possible explanation of no oxygen ordering for their suppressed T_c's unlikely (similar data had been observed in bulk materials quenched from high temperatures [13]), because of the relatively low quenching temperature. A second explanation was that the preparation time was too short with respect to the oxygen diffusion coefficient and the films did not have time to order properly. This is unlikely for the data presented by Ye, who took about the same time to prepare their films. On the other hand, in a paper published a year later by the group led by Bruynserade (which includes Osquiguil) [107], they observe room temperature annealing for oxygen–deficient films. The change in T_c is most striking for a film with a nominal oxygen content of 6.55 which changes by 20 K. For oxygen contents higher than 6.6, the T_c changes by less than 4 K. The saturation T_c is plotted vs the oxygen content and a "guide to the eye" line is indicated, which shows the 2–plateau behavior, but the spread in data is considerable. Room temperature annealing was not investigated in our data, and the only real data to investigate is in the case of a nominal oxygen content of 6.7. While the non–PAC films usually were measured several days after the anneal, the PAC films were measured no later than 24 hours after the anneal, but at this time the films had almost reached their saturation T_c according to [107]. The differences in the T_c between the PAC and non-PAC films are more likely due to defects in the PAC films (they had suppressed T_c right after the deposition) than to room temperature annealing. Some of the non-PAC films are being investigated by Raman-spectroscopy at the moment, which should tell us more about the true oxygen content of the films. Whatever the physical conditions that caused the differences to the data published by Ye, it happened

in two very different systems with film deposited by two different methods (the Osquiguil films are sputtered, our films are co-evaporated).

6.9 PAC Results

The first set of PAC experiments on deoxygenated films at room temperature showed that there is a significant change in frequency of the A site with changing oxygen content as well as change in the orientation of the electric field gradient. The latter is expected, because for fully oxygenated films, the main axis of the electric field gradient is along the *b*-axis, while for $YBa_2Cu_3O_{6.25}$ it points along the *c*-axis. The question is, for what oxygen

Film Name	anneal	T_c [K]	*c*-axis length [Å]
HTC 32	7 (as deposited)	79.9 K	11.7
HTC 32	6.7	37.9 K	11.77
HTC 32	6.5	n/a	11.835
HTC 32	6.4	n/a	11.841
HTC 33	7 (as deposited)	82.55K	not measured
HTC 33	6.7	not measured	not measured
HTC 33	6.4	n/a	not measured
HTC 33	6.25	n/a	not measured
HTC 34	7 (as deposited)	85.84	11.705
HTC 34	6.7	47	11.782
HTC 34	6.5	n/a	11.837
HTC 34	6.4	n/a	11.849
HTC 34	6.25	n/a	11.859
HTC 35	7 (as deposited)	82.92	11.719
HTC 35	6.7 @400 °C		
HTC 35	6.7 @550 °C		
HTC 35	6.7 @600 °C		
HTC 35	6.7 @750 °C		

Table 6.7 Summary of anneals performed on several PAC–films, as well as T_c and *c*-axis length, when applicable.

content does it flip? We found that the main axis of the electric field gradient had already flipped at a nominal oxygen content of 6.7 which was surprising, but considering that the "6.7" is more likely to be a film with an oxygen content of $x \approx 6.5$ considering the discussion earlier in this chapter, perhaps it is not quite so unexpected. Because of inferior quality substrates, only some preliminary information could be deduced, including the need to measure the films in both orientations to be able to fit an η to the data (The main axis of the electric field gradient was pointing along the *c*-axis after the 6.7 anneal. Fig. 4.6 shows clearly, that in that case for $\alpha = 45°$, for $\beta = 90°$ ω_2 is almost completely suppressed and for $\beta = 0°$, ω_1 is almost completely suppressed. To determine η from the ratio ω_1/ω_2, both orientation have to be measured to determine the frequencies.) Table 6.7 sums up the anneals done to the different PAC films and gives the T_c's and measured *c*-axis length.

HTC 34 provided us with a lot of valuable data. As seen in the Table 6.7, we were able to perform a series of anneals, at a nominal oxygen contents of $x \approx 7$, 6.7, 6.5, 6.4 and 6.25. The 6.25 anneal was done by putting the film into the deposition chamber, pumping down to a pressure of 10^{-6} torr, heating the substrate to 500 °C for 1 hour and then quenching the film. Table 6.8 gives the dependence of the asymmetry and the line width as well as the frequency on the oxygen content.

The most important result is for a nominal oxygen content of 6.7, which is more likely to be closer to 6.5, (further Raman studies are underway) the asymmetry is 1, indicating that one of the components of the electric field gradient is zero. Because the main axis of the electric field gradient points along the *c*-axis, the zero component is in the *ab*-plane. Assuming an oxygen content of 6.5 instead of the nominal 6.7, this would indicate a complete ordering of the oxygen atoms into long chains, with every other chain unfilled, as indicated in Fig. 1.6. For decreasing oxygen contents, the asymmetry decreases again, indicating that the V_{xx} and V_{yy} become more equal, which can be explained by oxygen moving out of the long ordered chains. The line width is a measure of how well–defined the environment is around the set of probes. The seeming contradiction between the asymmetry indicating completely ordered chains and the line width widening at the same time (see Fig. 6.9) can be resolved by considering that each probe which contributes to the signal is in a site with an asymmetry of 1, which in turn ends up forming the long chains, but because of small variations in the lattice (the general theme of films being more disordered) the environments might be slightly different, leading to a bigger linewidth. Because there are obvious changes within the lattice (the *c*-axis length increases with decreasing oxygen

oxygen content	ν_Q [MHz]	η	$\Delta\omega/\omega$ [%]
7	36.0(1)	0.51(1)	12.2
6.7	24.0(1)	0.99(1)	19.4
6.5	24.3(1)	0.50(1)	21.5
6.4	21.5(1)	0.46(1)	12.8
6.25	19.6(1)	0.34(1)	12.8

Table 6.8 ν_Q, η, $\Delta\omega/\omega$ for film HTC 34 annealed for nominal oxygen contents of 7 (as deposited), 6.7, 6.5, 6.4 and 6.25.

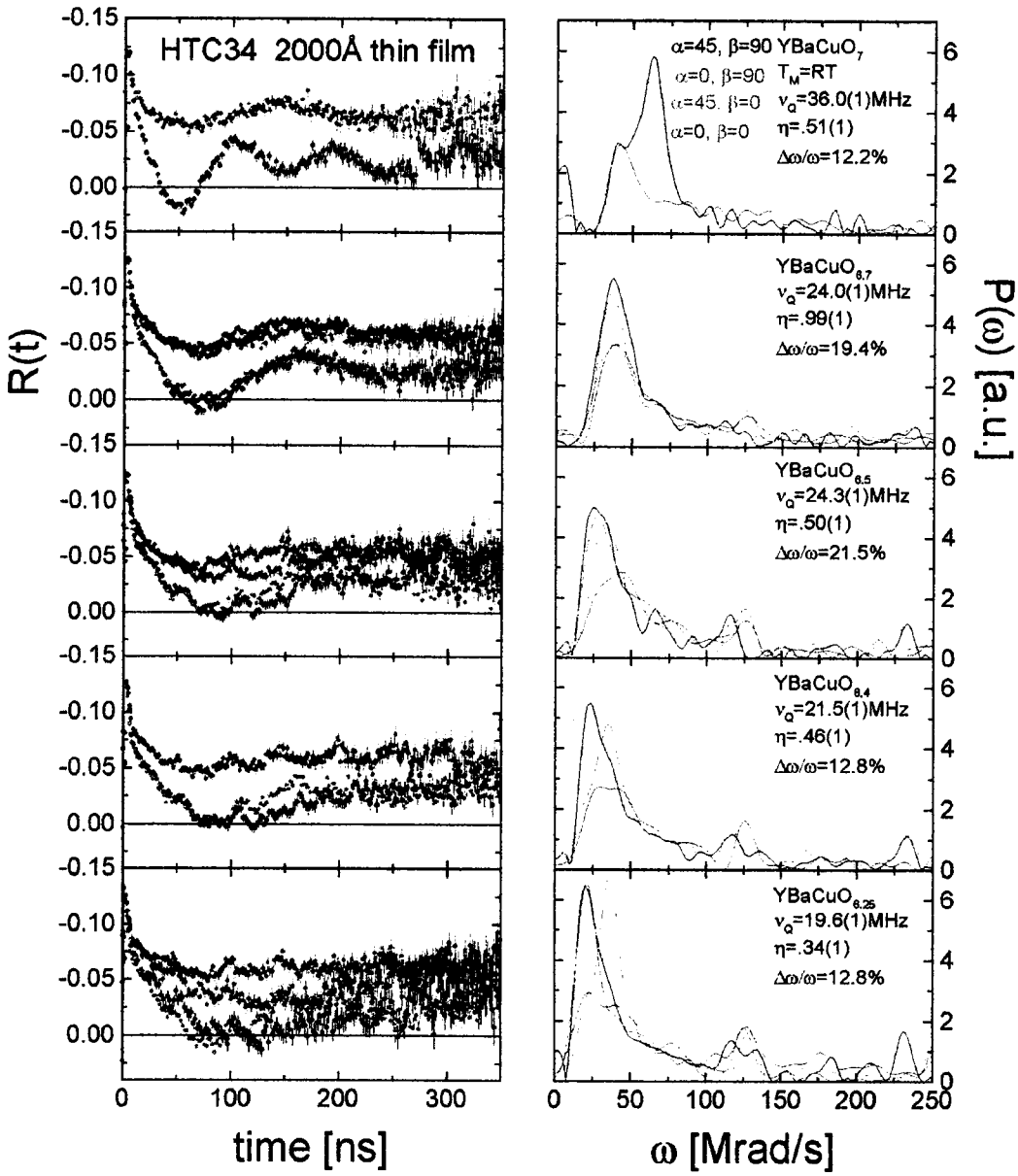

Fig. 6.8 $R(t)$ curves and Fourier transforms of all of the spectra taken on HTC 34, with the anneals indicated. All spectra were taken at room temperature.

content), this could explain why the line width changes, but it would require more investigation.

A final set of experiments was done by moving the annealing set up to the spectrometers and, using a different furnace, observing the PAC spectra in–situ while keeping the films at the various temperatures and appropriate pressures to reach a nominal 6.7 oxygen content. It was hoped to see some dynamic effects, particularly seeing the oxygen move, which allows the calculation of hopping rates. The oxygen motion influences the linewidth, and the line first widens with increasing temperature due to the thermal motion. At a certain temperature, the motion becomes faster than the lifetime of the probe nucleus and the line width narrows again. This phenomenon is called motional narrowing. Wang [108] in her thesis measured this behavior in ceria and has an overview of the literature.

The motional narrowing was not observed in HTC 35, the linewidth stayed the same over the whole range from 400 °C to 750 °C , as can be seen in Fig. 6.10. The reason for this behavior is not clear at the moment, but one can

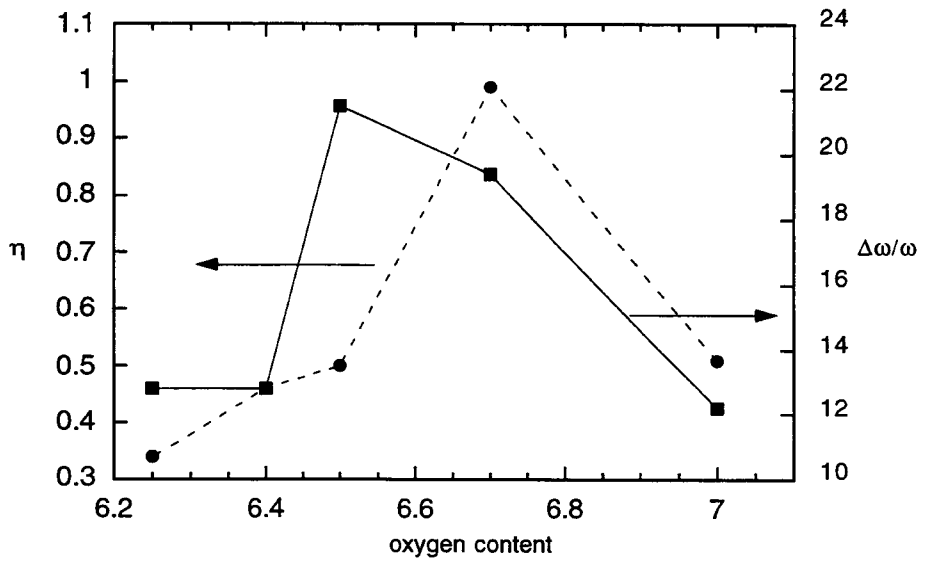

Fig. 6.9 Asymmetry and linewidth as a function of oxygen content for HTC 34. While the asymmetry has a maximum for an oxygen content of 6.7, the relative linewidth is the biggest for an oxygen content of 6.5.

speculate. One reason might be that we had already reached the tail–end of the motional narrowing and that the linewidth could not narrow any more. Furthermore, the above behavior was calculated for materials with the symmetry axis of the electric field gradient fluctuating randomly in all three dimensions [109] but in the $YBa_2Cu_3O_{7-\delta}$ we have the oxygen moving in only two dimensions. These guesses show that more investigation has to be done, including giving the theory a chance to catch up and calculate what one would expect to see.

We learned something else from this film, because in our bid to see some dynamic effects, we heated the sample up to 750 °C (while slightly overpressurizing it) and did not see any decomposition, in contrast to early films where decomposition began at 700 °C, when heated in flowing oxygen (at 800 °C, the amount of $Y_2Cu_2O_5$ was significant). This indicates that the $YBa_2Cu_3O_{6+x}$ pellet kept the sample from decomposing, most probably by providing a high enough barium partial pressure to keep the barium in the film (the vapor pressure of barium at ≈775 °C is of the order of 10^{-1} torr [110]).

These experiments on oxygen–deficient $YBa_2Cu_3O_{6+x}$ films showed some very promising first results. The most important step now is to determine the oxygen content of the films by Raman spectroscopy. In addition, the oxygen contents between the nominal 6.7 and the fully oxygenated 7.0 need to be investigated, especially with respect to the asymmetry. Our last set of experiments also indicates that oxygen–deficient films should be investigated below 400 °C, because some significant oxygen motion might be occurring at temperatures below 400 °C. Our films were quenched from 400 °C, assuming that the oxygen atoms were moving too slow at lower temperatures to cause significant uptake during cool–down and

therefore increasing the oxygen content, which they did not do judging from the measured T_c and *c*-axis length.

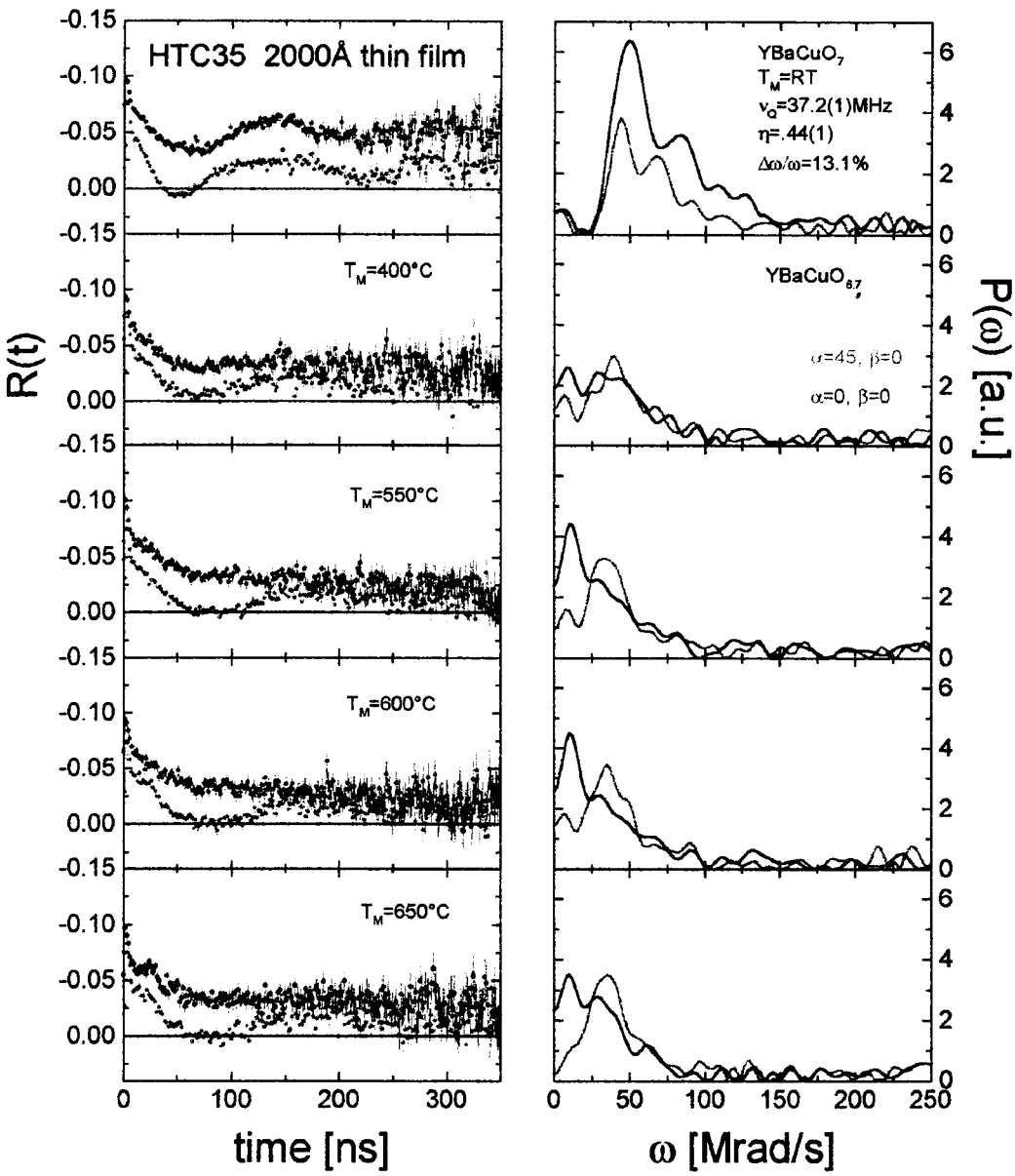

Fig. 6.10 *R*(*t*) and Fourier transforms for HTC 35, annealed in–situ at different temperatures to achieve a 6.7 anneal. The pressure was kept at the value appropriate according to the phase–diagramm [28].

Chapter 7
Summary

7.1 The Electric Field Gradient in $YBa_2Cu_3O_{7-\delta}$ Films

Perturbed angular correlation spectroscopy (PAC) is used as a tool to study phase transition in materials, because its sensitivity is temperature independent, and it can therefore be used to very high temperatures (1000 °C), unlike some of the related hyperfine techniques of nuclear quadrupole resonance (NQR) and Mößbauer spectroscopy. For the study of thin films, PAC has the added advantage that the number of probe atoms needed (10^{10} to 10^{11}) to perform the measurements is several orders of magnitudes smaller than for Mößbauer spectroscopy (10^{14}) and NQR (10^{18}).

All of these hyperfine techniques measure the interaction of the quadrupole moment of the probe nucleus with electric field gradient at the site of the nucleus. The electric field gradient stems from the distribution of charges around the probe nucleus and is a tensor. It characterizes the asphericity of the charge distribution. As a consequence, in cubic materials the electric field gradient is zero, and hyperfine techniques can be used in cubic materials to study defects.

It is possible to do PAC studies in powders as well as oriented samples. If oriented samples are used, either in the form of single crystals or thin films, the orientation of the electric field gradient with respect to the host crystal can be determined. This thesis completed the determination of the orientation of the electric field gradient, in orthorhombic $YBa_2Cu_3O_7$ as well as tetragonal $YBa_2Cu_3O_{6.25}$ at room temperature and ambient pressure. Table 7.9 is a summary of the information determined.

	main axis of efg	ν_Q [MHz]	η
$YBa_2Cu_3O_7$	along *b*-axis	39	0.5
$YBa_2Cu_3O_{6.25}$	along *c*-axis	19	0.4

Table 7.9 Summary of electric field gradient in $YBa_2Cu_3O_7$ and $YBa_2Cu_3O_{6.25}$ at room temperature.

c-Axis oriented $YBa_2Cu_3O_{6+x}$ films are twinned. This required the growth of *a*-axis oriented films, because the main axis of the electric field gradient points along the *b*-axis. This conclusion could only be reached if about 20% of the film were assumed to be *b*-axis oriented, an assumption which could not be confirmed by x-ray diffraction measurements. This issue has not been conclusively resolved, but arguments based on the differences between x-ray diffraction and PAC can be used to explain it. For $YBa_2Cu_3O_{6.25}$ films, the direction of the main axis of the electric field gradient is readily determined from *c*-axis oriented films, because it is pointing along the *c*-axis.

To determine the optimum growth conditions for *a*-axis films, studies on the dependence of the amount of *a*-axis oriented grains depending on the temperature and pressure were carried out. It was shown that the largest amount of *a*-axis oriented grains was formed at a deposition temperature of 600 °C and a local oxygen pressure at the substrate of 1.1 mtorr, but under these conditions the T_c was suppressed to 58 K.

7.2 Impurity Phases in $YBa_2Cu_3O_{6+x}$

Much of the early PAC work in $YBa_2Cu_3O_{6+x}$ was plagued by uncertainty about which is the true $YBa_2Cu_3O_{6+x}$ signal and at what site within the structure does the ^{111}In substitute. In retrospect, we see that much of the

earlier work determined signals from impurity phases and not from the $YBa_2Cu_3O_{6+x}$ itself.

Once all of the PAC signals of possible impurity phases had been identified, PAC is a useful tool to determine the quality of $YBa_2Cu_3O_{6+x}$ films and can give early warning signals about pressure and temperature conditions which lead to degradation of this films. PAC has advantages over x-ray diffraction, a common tool to determine the existence of impurity phases, because it is more local. In addition, x-ray diffraction can only show the existence of oriented phases, but an impurity will show a PAC signal regardless of orientation.

Orthorhombic $YBa_2Cu_3O_{7-\delta}$ films deposited in this laboratory showed only one site, which had been identified in earlier work as the signal of the ^{111}In substituting at the Y site. None of the commonly seen impurities in $YBa_2Cu_3O_{7-\delta}$ like $Y_2Cu_2O_5$ and Y_2BaCuO_5 were seen in our PAC spectra.

Tetragonal $YBa_2Cu_3O_{6.25}$ films, which were either quenched from the deposition conditions or were subjected to an additional anneal at 10^{-7} torr and 500 °C, showed a second site, called the B site. This signal was identified as $CuYO_2$ growing in the (012) orientation. Supporting x-ray studies confirmed this and also showed the formation of $BaCu_2O_2$ in the (112) orientation.

The B site signal was never seen in orthorhombic films and it disappeared in films when they were annealed in oxygen. It was also shown to disappear when the film was annealed in argon around 600 °C.

Gaining as much information as possible about the formation of the B site is important, because it forms under conditions commonly employed in the deposition of $YBa_2Cu_3O_{6+x}$ films, which are deposited in the tetragonal phase and are transformed to the superconducting orthorhombic phase by annealing them in oxygen at temperatures around 450 °C. Being able to prove

the formation of $CuYO_2$ under conditions not far removed from the actual deposition could mean, that even under standard condition $CuYO_2$ forms, but in amounts to small to detect.

7.3 Oxygen–deficient Films

$YBa_2Cu_3O_{6+x}$ films with varying oxygen contents were made to determine the change in the electric field gradient between a fully oxygenated $YBa_2Cu_3O_7$ and a $YBa_2Cu_3O_{6.25}$ film. To change the oxygen content a system was built which allows fine control of the pressure and the temperature. The films were annealed according to a phase diagram proposed by Gallagher [28], by staying on the pressure–temperature phase line for a given oxygen content. The anneals are a two–step process, with one annealing step at 600 °C and a second one at 450 °C. After the anneal the films were quenched from 400 °C to room temperature.

We have not yet verified that the oxygen content indicated by the anneal conditions was indeed obtained in our films. We suspect that the films have lower oxygen content than that intended. This suspicion is based on reduced T_c's compared to published data as well as the observed change in the *c*-axis length. Comparing our data to published data, we find a surprisingly good match to published film data [12], but both theirs and our data do not match published data for crystals [5] for oxygen contents between $\approx$ 6.7 and 6.3.

We found that the frequency ν_Q decreased with decreasing oxygen content. A surprising result was the behavior of the asymmetry. The asymmetry is 1 at an nominal oxygen content of 6.7 and then decreases again. X-ray as well as T_c measurement indicate that this oxygen content might be 6.5

(Raman studies are under way) and that the result can be explained by a complete ordering of the oxygen atoms along the *b*-axis with every other row unoccupied.

In–situ anneals, where the pressure and temperature were controlled while the sample was in the spectrometer did not show the motional narrowing expected, which would be evidenced in the line width.

7.4 Future Direction

In order to fully understand our results, the oxygen content of the films has to be determined. X-ray studies as well as the measured T_c's (where applicable) indicate that the actual oxygen contents are lower than they should be according to the anneal. This might work to our advantage, because there is every indication that the nominal 6.7 film is actually a 6.5 film, which is an oxygen content we are very much interested in.

This thesis presented some very promising first results, but also shows that there is a lot more to explore. The region between the nominal oxygen content of 6.5 and the fully oxygenated $YBa_2Cu_3O_7$ has to be carefully investigated to determine the change in the asymmetry. From the behavior of the asymmetry, one should be able to conclude more about the oxygen ordering in $YBa_2Cu_3O_{6+x}$. In order to do this, some experimental difficulties have to be solved for films with an oxygen content higher than 6.7, because the current procedure would require me to overpressurize the system. However the region with oxygen content less than 6.7 should be easily accessible.

Our first try at dynamic studies showed that we looked in the wrong place and did not see any dynamic behavior. This problem now has to be

attacked on two different fronts. One is the theoretical front, what we expected to see was deduced from behavior seen in ceria. Because $YBa_2Cu_3O_{6+x}$ is very different from ceria, starting with the crystal structure, theoretical calculations need to be carried out to calculate what is expected. On the experimental front, the region between room-temperature and 400 °C has to be investigated. Oxygen diffusion is very slow at these temperature, but for oxygen ordering to occur, the oxygen atoms only have to move on the order of one unit cell, which is definitely possible at room temperature, as evidenced by room temperature annealing.

The experiments carried out in this thesis answered some questions, like the final determination of the direction of the main axis of the electric field gradient, but as it normally happens in science, they provided us with a whole new set of questions to be answered, especially with respect to the work on oxygen–deficient films.

Bibliography

1. Fiory, A.T., Martin, S., Fleming, R.M., Schneemeyer, L.F., Waszczak, J.V., Hebard, A.F., and Sunshine, S.A., Physica C, (1989), **162-164**, 1195.

2. Onnes, K.H., Commun. Phys. Lab. Univ. Leiden, (1911) **124c.**

3. Bednorz, J.G. and Müller, K.A., Zeitschrift für Physik B., (1986) **64**, 189.

4. Wu, M.K., Ashburn, J.R., Torng, C.J., Hor, P.M., Meng, R.L., Gao, L., Huang, Z.J., Wang, Y.Q., and Chu, C.W., Phys. Rev. Lett., (1987) **58**(9), 908

5. Jorgensen, J.D., Veal, B.W., Paulikas, A.P., Nowicki, L.J., Crabtree, G.W., Claus, H., and Kwok, W.K., Phys. Rev. B, (1990) **41**(4), 1863.

6. Poole, C.P.J., Farach, H.A., and Creswick, R.J., *Superconductivity.* (1995), San Diego, Academic Press.

7. Neiman, R.L., Giapintzakis, J., and Ginsberg, D.M., Phys. Rev. B, (1994) **50**(21), 16028.

8. Burmann, T., Geerk, J., Meyer, O., Schneider, R., and Linker, G., Solid State Communications (1994) **90**(9), 599.

9. Karppinen, M., Fukuoka, A., Niinisto, L., and Yamauchi, H., Superconductor Science and Technology, (1996) **9**(3), 121.

10. Appelman, E.H., Morss, L.R., Kini, A.M., Geiser, U., Umezawa, A., Crabtree, G.W., and Carlson, K.D., Inorg. Chem., (1987) **26**(20), 3237.

11. Nakamura, K., Ye, J., and Ishii, A., Physica C, (1991) **213**, 1.

12. Osquiguil, E., Maenhoudt, M., Wuyts, B., and Bruynseraede, Y., Appl. Phys. Lett., (1992) **60**(13), 1627.

13. Namgung, C., Irvine, J.T.S., and West, A.R., Physica C, (1990) **168**, 346.

14. Ye, J. and Nakamura, K., Phys. Rev. B, (1993) **48**(10), 7554.

15. Matijasevic, V., Rosenthal, P., Shinohara, K., Marshall, A.F., Hammond, R.H., and Beasley, M.R., J. Mater. Res., (1991) **6**(4), 682.

16. Martínez, O., Jiménez, J., Martín, P., Prieto, A.C., Degoy, S., Chambonnet, D., Belouet, C., Nicoletti, S., and Correra, L., Physica C, (1996) **270**, 144.

17. Huong, P.V., Bruyère, J.C., Bustarret, E., and Granchamp, P., Solid State Communications, (1989) **72**(2), 191.

18. Ceder, G., McCormack, R., and de Fontaine, D., Phys. Rev. B, (1991) **44**(5), 2377.

19. Cava, R.J., Batlogg, B., Rabe, K.M., Rietman, E.A., Gallagher, P.K., and Rupp, L.W.J., Physica C, (1988) **156**, 523.

20. Lütgemeier, H., Schmenn, S., Meuffels, P., Storz, O., Schöllhorn, R., Niedermayer, C., Heinmaa, I., and Baikov, Y., Physica C, (1996) **267**, 191.

21. de Fontaine, D., Wille, L.T., and Moss, S.C., Phys. Rev. B, (1987) **36**(10), 5709.

22. Aligia, A.A., Garcés, J., and Bonadeo, H., Phys. Rev. B, (1990) **42**(16), 10226.

23. Veal, B.W., Paulikas, A.P., You, H., Shi, H., Fang, Y., and Downey, J.W., Phys. Rev. B, (1990) **42**(10), 6305.

24. Shaked, H., Jorgensen, J.D., Hunter, B.A., Hitterman, R.L., Paulikas, A.P., and Veal, B.W., Phys. Rev. B, (1995) **51**(1), 547.

25. Shin, D.C., Park, Y.K., Park, J.-C.L., Kang, S.-J.l., and Yonn, D.Y., Physica C, (1997) **280**, 142.

26. Maissel, L.I. and Glang, R., eds. *Handbook of Thin Film Technology.* (1970), McGraw-Hill Book Company, New York.

27. Tom, D.W., *Microstructural Characterization of $YBa_2Cu_3O_{7-\delta}$ Thin Films with Time Differential Perturbed Angular Correlation Spectroscopy,* PhD thesis in *Physics.* (1995), Oregon State University, Corvallis, Oregon

28. Gallagher, P.K., Advanced Ceramic Materials, (1987) **2**(3B), 632.

29. Thomsen, C. and Cardona, M., *Raman Scattering in High-T_c Superconductors,* in *Physical Properties of High Temperature Superconductors I,* D.M. Ginsberg, Editor. (1989) World Scientific, Singapore.

30. Dieckmann, N., Kürsten, R., Löhndorf, M., and Bock, A., Physcia C, (1995). **245**, 212.

31. Feile, R., Physica C, (1989) **159**, 1.

32. Macfarlane, R.M., Rosen, H.J., Engler, E.M., Jacowitz, R.D., and Lee, V.Y., Phys. Rev. B, (1988) **38**(1), 284.

33. Thomsen, C., Wegerer, R., Habermeier, H.-U., and Cardona, M., Solid State Communications, (1992) **83**(3), 199.

34. Gibson, G., MacManus-Driscoll, J.L., and Cohen, L.F., IEEE Transactions on Applied Superconductivity, (1997) **7**(2), 2130.

35. Cohen, L.F., Li, Y.B., Gibson, G., and MacManus-Driscoll, J.L. *Investigation of cation disorder in c-axis YBCO 123 thin films using Raman miscroscopy*, in *MRS (Fall Meeting)*. (1995) Boston.

36. Schatz, G. and Weidinger, A., *Nuclear condensed matter physics: nuclear methods and applications*. 2 nd ed. (1996), Chichester; John Wiley & Sons Ltd.

37. Ito, W., Mahajan, S., Yoshida, Y., Morishita, T., Kumagai, M., and Yabuta, K., Jpn. J. Appl. Phys., (1994) **33**(Part 1), 5701.

38. Ashcroft, N.W. and Mermin, N.D., *Solid State Physic*. 1976: Holt, Rinehart and Winston, 826.

39. Scherrer, P., Nachr. Ges. Wiss. Göttingen, Math.-Phys. Kl., (1918) **2**, 96.

40. Prakash, S. and Bunshah, R.F., J. Mater. Res., (1992) **7**(9), 2343.

41. Nuffield, E.W., *X-ray Diffraction Methods*. 1966: John Wiley & Sons, Inc.

42. Cullity, B.D., *Elements of X-ray Diffraction*. 2nd ed. 1978: Addison-Wesley Publishing Company, Inc.

43. Knorr, D.B., Weiland, H., and Szpunar, J.A., JOM, (1994,September), 32.

44. Zheng, J.P., Dong, S.Y., and Kwok, H.S., Appl. Phys. Lett., (1991) **58**(5), 540.

45. Frauenfelder, H. and Steffen, R.M., in *Alpha-, Beta- and Gamma-Ray Spectroscopy*, K. Siegbahn, Editor. (1965), North-Holland: Amsterdam. p. 997.

46. Butz, T., Hyperfine Interact., (1989) **52**, 189.

47. Wegner, D., Hyperfine Interact., 91985) **23**, 179.

48. Yu, J., Freeman, A.J., Podloucky, R., Herzig, P., and Weinberger, P., Phys. Rev. B, (1991) **43**(1), 532.

49. Arends, A.R., Hohenemser, C., Pleiter, F., De Waard, H., Chow, L., and Suter, R.M., Hyperfine Interact., (1980) **8**, 191.

50. Masterov, V.F., Nasredinov, F.S., and Seregin, P.P., Phys. Solid State, (1995) **37**(5), 687.

51. Tröger, W. and Butz, T., Z. Naturforsch., (1992) **47a**, 12.

52. Bartos, A. and Uhrmacher, M., Phys. Rev. B, (1993) **48**(10), 7478.

53. Saitovitch, H., Silva, P.R.J., and Rodríguez, A.M., Hyperfine Interact., (1992) **73**, 277.

54. Schwenker, R., *Perturbed angular correlation spectroscopy in the high temperature superconducting material* $YBa_2Cu_3O_{7-x}$, MS thesis in *Physics*. (1990), Oregon State University, Corvallis,Oregon.

55. Füssel, A., *Chemical Phases in the Y-Ba-Cu-O System Identified by TDPAC*, MS thesis in *Physics*. (1993), Oregon State University: Corvallis, Oregon.

56. Tom, D.W., Platzer, R., Gardner, J.A., and Tate, J., Appl. Phys. Lett., (1993) **63**(23), 3224.

57. Bartos, A. and Uhrmacher, M., Hyperfine Interact., (1990) **61**, 1101.

58. Uhrmacher, M. and Bartos, A., Hyperfine Interact., (1990) **61**, 1097.

59. Wiarda, D., Uhrmacher, M., Bartos, A., and Lieb, K.P., J. Phys.: Condens. Matter, (1993) **5**, 4111.

60. Attili, R.N., Uhrmacher, M., Lieb, K.P., and Ziegeler, L., Phys. Rev. B, 1996. **53**(2), 600.

61. Platzer, R., Schwenker, R., Füssel, A., Tom, D.W., Tate, J., Gardner, J.A., Evenson, W.E., and Sommers, J.A., Hyperfine Interact., (1997) **110**, 271.

62. Weidlich, G.A., *Structural Properties of Indium Doped* $YBa_2Cu_3O_{7-x}$ *High* T_c *Superconductors*, MS thesis in *Physics*. 1989, Oregon State University, Corvallis.

63. Ambrosch-Draxl, C., Blaha, P., and Schwarz, K., Hyperfine Interact., (1990) **61**, 1117.

64. Plank, H., Bauer, O., Forkel, D., Meyer, F., Roas, B., Saemann-Ischenko, G., Ströbel, J., Wolf, H., and Witthuhn, W., Hyperfine Interact., (1990) **61**, 1139.

65. Platzer, R., Dumkow, I.D., Tom, D.W., Tate, J., and Gardner, J.A., J. Mater. Res., (1998), accepted for publication March 1998.

66. Braginski, A.I., Physica C, (1991) **185-189**(1), 391.

67. Ito, W., Mahajan, S., Yoshida, Y., Watanabe, N., and Morishita, T., J. Mater. Res., (1994) **9**(7), 1625.

68. Eom, C.B., Marshall, A.F., Laderman, S.S., Jacowitz, R.D., and Geballe, T.H., Science, (1990) **249**, 1549.

69. Li, Y.Q., Zhao, J., Chern, C.S., Gallois, B., Norris, P., and Kear, B., J. Appl. Phys., (1992) **71**(5), 2472.

70. Jeschke, U., Schneider, R., Ulmer, G., and Linker, G., Physica C, (1995) **243**, 243.

71. Terashima, Y., Sagoi, M., Kubo, K., Mizutani, Y., Miura, T., Yoshida, J., and Mizushima, K., Jpn. J. Appl. Phys., (1989) **28**(4), L653.

72. Zhong, Q., Chou, P.C., Li, Q.L., Taraldsen, G.S., and Ignatiev, A., Physica C, (1995) **246**, 288.

73. Raven, M.S., Inameti, E.E., Wan, Y.M., and Murray, B.G., phys. stat. sol. (a), (1994) **146**, 685.

74. Inam, A., Rogers, C.T., Ramesh, R., Remschnig, K., Farrow, L., Hart, D., Venkatesan, T., and Wilkens, B., Appl. Phys. Lett., (1990) **57**(23), 2484.

75. Trajanovic, Z., Takeuchi, I., Warburton, P.A., Lobb, C.J., and Venkatesan, T., Physica C, (1996) **265**, 79.

76. Rosova, A., Chromik, S., Benacka, S., and Wuyts, B., Physica C, (1995) **253**, 39.

77. Sodtke, E. and Münder, H., Appl. Phys. Lett., (1992) **60**(13), 1630.

78. Hamet, J.F., Mercey, B., Hervieu, M., and Raveau, B., Physica C, (1992) **193**, 465.

79. Ha, D.H., Park, Y.K., and Park, J.-C., Jpn. J. Appl. Phys., (1994) **33**, L1588.

80. Mahajan, S., Ito, W., Yoshida, Y., and Morishita, T., Physica C, (1993) **213**, 445.

81. Kawamoto, K. and Hirabayashi, I., *Oxygen ordering and transformation from a-axis oriented to b-axis oriented films in* $YBa_2Cu_3O_y$., in *Advances in Superconductivity VII.* 1994.

82. Ronay, M. and Nordlander, P., Physica C, (1988) **153-155**, 834.

83. Mogro-Campero, A. and Turner, L.G., Journal of Superconductivity, (1991) **4**(4), 279.

84. Filipczuk, S.W., Driver, R., and Smith, G.B., Physica C, (1990) **170**, 457.

85. Siegal, M.P., Philips, J.M., van Dover, R.B., Tiefel, T.H., and Marshall, J.H., J. Appl. Phys., (1990) **68**, 6353.

86. Bormann, R. and Nölting, J., Appl. Phys. Lett., (1989) **54**, 2148.

87. Hammond, R.H. and Bormann, R., Physica C, (1989) **162**, 703.

88. Yoshida, A., Tamura, H., Gotoh, K., Imamura, T., and Hasuo, S., J. Appl. Phys., (1993) **73**(11), 7549.

89. Li, Y.B., Shelley, C., Cohen, L.F., Caplin, A.D., and Stradling, R.A., J. Appl. Phys., (1996) **80**(5), 2929.

90. López, J.G., Siejka, J., Mercandalli, L.M., Bisaro, R., Blanchin, M.G., and Teodorescu, V., Physica C, (1997) **275**, 65.

91. Blanchin, M.-G., Teodorescu, V.S., Garcia-Lopez, J., Siejka, J., Bisaro, R., and Mercandalli, L.M., Phil. Mag. A, (1996) **74**(1), 151.

92. Eibl, O. and Roas, B., J. Mater. Res., (1990) **5**(11), 2620.

93. Tinkham, M., Helv. Phys. Acta, (1988) **61**, 443.

94. Kohler, B. and Jansen, M., Z. Anorg. Allg. Chem., (1986) **543**, 73.

95. Teske, C.L. and Müller-Buschbaum, H., Z. Naturforsch., B: Anorg. Chem., Org. Chem., (1972) **27**, 296.

96. Ishiguro, T., Ishizawa, N., Mizutani, N., and Kato, M., J. Solid State Chem., (1983) **49**, 232.

97. Marshall, A.F., Matijasevic, V., Rosenthal, P., Shinohara, K., Hammond, R.H., and Beasley, M.R., Appl. Phys. Lett., (1990) **57**(11), 1158.

98. Ahn, B.T., Lee, V.Y., Beyers, R., Gür, T.M., and Huggins, R.A., Physica C, (1990) **167**, 529.

99. Whitler, J.D. and Roth, R.S., *Phase Diagrams for High T_c superconductors*, American Ceramic Society, Washington, (1991).

100. Beyers, R. and Ahn, B.T., Annu. Rev. Mater. Sci., (1991) **21**, 335.

101. Pankajavalli, R. and Sreedharan, O.M., Journal of Materials Science, (1996) **31**, 3137.

102. Konetzki, R.A. and Schmid-Fetzer, R., J. Solid State Chem., (1995) **114**, 420.

103. Cochrane, J.W., Russell, G.J., and Matthews, D.N., Physica C, (1994) **232**, 89.

104. Ludwig, C., Jiang, Q., Kuhl, J., and Zegenhagen, J., Physica C, (1996) **269**, 249.

105. Fietz, W.H., Quenzel, R., Ludwig, H.A., Grube, K., Schlachter, S.I., Hornung, F.W., Wolf, T., Erb, A., Kläser, M., and Müller-Vogt, G., Physica C, (1996) **270**, 258.

106. Ye, J. and Nakamura, K., Physica C, (1995) **254**, 113.

107. Libbrecht, S., Osquiguil, E., Wuyts, B., Maenhoudt, M., Gao, Z.X., and Bruynseraede, Y., Physica C, (1993) **206**, 51.

108. Wang, R., *Perturbed Angular Correlation Spectroscopy of Defects in Ceria*, PhD thesis in *Physics*. 1991, Oregon State University, Corvallis

109. Evenson, W.E., McKale, A.G., Su, H.T., and Gardner, J.A., Hyperfine Interact., (1990) **61**, 1379.

110. Lide, D.R., ed. *CRC Handbook of Chemistry and Physics*. 73rd ed. (1993), CRC, Boca Raton.

Appendices

Appendix A
How to grow a film

The growth process of a films can be split up into several steps

– choice and cleaning of the substrate

– loading the chamber

– heating the substrate in preparation for the actual film growth

– depositing the film

– annealing the film

– cool-down after deposition

A.1 Choice and Cleaning of the Substrate

Three main substrates are being used in this lab to grow $YBa_2Cu_3O_{6+x}$ films on them. Magnesiumoxide (MgO) can be considered the workhorse substrate. It is used especially when a new procedure is being tried and one goes through a lot of substrates trying to determine the optimum parameters. MgO is significantly cheaper than the other substrates. Its disadvantages are that it has a fairly large lattice mismatch (a=4.213 Å, which is a mismatch of 10.2% with respect to the a-axis and 8.2% with respect to the b-axis) and it is hydroscopic and has a tendency to form an amorphous surface layer after a fairly short time. One can still grow films on these substrates, but their quality is usually not as good as films on a new, fresh substrate.

A second substrate used is strontium titanate ($SrTiO_3$). This substrate has a very good lattice match (a=3.90Å). This substrate is the substrate of choice for the PAC films, because it usually produces higher quality films. Its

biggest disadvantage, namely a high dielectric constant, is of no concern to us, because we are not interested in microwave applications.

The substrate of choice for the a-axis films was lanthanum aluminate ($LaAlO_3$). Its lattice match is not quite as good as in the case of the $SrTiO_3$ (a=3.79 Å), but considering that we were developing a new technique, we needed a workhorse substrate again. In addition, the dielectric properties for $LaAlO_3$ are a lot better than for the $SrTiO_3$, important in device applications, which is one of the reasons *a*-axis films are interesting.

All substrates are subjected to the same cleaning procedures before being loaded into the chamber. They are cleaned for 10 min. each in an ultrasonic cleaner, first in acetone, then methanol, then ethyl alcohol. In between each bath, they are carefully dabbed dry with a KimWipe, because air-drying them leaves residues on the surface of the substrate.

A.2 Loading the Chamber

Loading the chamber is a top–down process. First the substrate is placed in the substrate holder with the polished side down. The heater is positioned on top of the holder and tested to make sure that is does not wiggle.

Because the barium oxidizes rather rapidly, the quartz-crystal monitoring the barium boat has to be cleaned each time to remove any oxidized and therefore loose barium. This is done by removing the crystal holder, gently pushing the crystal out of the holder, cleaning the crystal with alcohol and putting it back into the holder and the holder back into the chamber. If this procedure has not been done before the barium boat was outgassed, it has to be done now.

Otherwise the chamber can be loaded now. Barium pieces, which have been carefully dabbed to remove most of the oil in which they were stored in order to avoid or at least slow down oxidation, are put into the barium boat and the yttrium and copper boat are loaded with the respective metals.

The last step is to check the shutter. Its function is to protect the substrate from the evaporants while the rates still stabilize and to end the deposition by covering the substrate before the boats are being switched off. Testing the working of the shutter also gives a chance to check if the substrate is still in the proper position after the heater has been placed on top of it.

A.3 Heating the Substrate before Deposition

After the chamber has been pumped down to 10^{-7} torr a film can be made. First the substrate has to be preheated. This is done to get rid of anything on the surface of the substrate, including water. The heating procedure is a three step procedure, controlled by a computer program:

heating at 10°C/min to 400°C
staying at 400°C for 10 min
heating at 10°C/min to 600°C
staying at 600°C for 10 min
heating at 10°C/min to 720°C
staying at 720°C for 30 min

after the 30 min at 720°C the temperature is ramped manually to the desired temperature for the deposition.

In addition, it is a good idea to switch on the quartz-rate monitors now. One reason is that it gives the crystals time to stabilize. The other reason is that if anything is wrong with the quartz-rate monitors, especially something

that requires opening the chamber, the chamber is not that hot yet and one does not have to wait too long for it to cool down (there is not possibility to actively cool the chamber) and therefore saves time.

A.4 Depositing the Film

Before the actual deposition is done, the choice has to be made about which orientation the film is supposed to grow in. This influences the substrate temperature during deposition and to a lesser degree the oxygen pressure during the deposition. For a *c*-axis film on MgO, the substrate temperature is 650 °C, while for the same kind of film on $SrTiO_3$, a substrate temperature of 670 °C is used. For the *a*-axis films on $LaAlO_3$, the temperature is reduced to between 580 °C and 600 °C.

In order to grow the right structure, it is important to supply some oxygen during the deposition. For a "standard", orthorhombic, *c*-axis oriented film, the pressure is set at 25% of 50 sccm, which yields a back-ground pressure of about 5.5×10^{-5} torr, with the local pressure at the substrate being in the mtorr range. For the *a*-axis films, in order to maximize the amount of film growing in the right orientation, it is advantages to lower the pressure to 10% to 15% of 50 sccm, even though that reduces the transition temperature.

In addition, the shutter has to be switched on and set on *open* (it will not actually open until the *operate* button is pressed). And most importantly, the power to the boats has to be switched on and the settings on the power controllers have to be checked. This is most important for the barium boat, because two different settings are used for the outgassing and the actual deposition.

After everything has been set to the desired values, the actual deposition can be started. Similar to the heating of the substrate, the boats are heated in a two step process. After the rates stabilized and the oxygen has been switched on, the shutter is opened and the actual deposition is started. While the deposition is going on, not much can be done by the operator except noting if the rates are stable enough or if they are that unstable that the deposition has to be stopped before the desired thickness has been reached. Our films are deposited at 500Å /min, which means that a 2000Å thickness is reached after 4 min. After the desired thickness has been reached, the deposition is stopped by closing the shutter and then switching off the boats.

A.5 Annealing the Film

This step is responsible for the oxygen content of the film. The experiments have shown that it is only feasible to achieve two different oxygen contents by the in-situ anneal: one which is almost 7 and therefore has the orthorhombic structure and an oxygen content of 6.25, which shows the tetragonal structure. For an orthorhombic film, the chamber is backfilled with oxygen to a pressure of 15 torr, the temperature is ramped to 450°C at 10°C/min and the film stays at that temperature for 30 min. For a tetragonal film, the oxygen is switched off as fast as possible and the film is annealed in vacuum, which means that the pump pumps on the chamber for the whole time of the anneal. The temperature during the anneal is 500°C. Higher temperatures increase the amount of impurities formed. The anneal time is usually around 1 h, with longer anneals again introducing more impurities.

A.6 Cool-down after Deposition

There are two basic options after the anneal. The film can either be ramped down slowly at 20°C/min. This is used for the orthorhombic films in order to make sure that the films stay fully oxygenated.

The other option is a quench, meaning that the film is cooled down as fast as possible. We do not have the option here of doing a true quench by dropping the film in liquid nitrogen, therefore our quench is done by switching off the heater and letting the film and chamber cool down by itself.

As a summary, the temperature and to a lesser degree the oxygen-pressure during the deposition are responsible for the orientation of the film, while the structure of the film (orthorhombic or tetragonal) is controlled mostly by the oxygen pressure during the anneal, with the temperature mostly being responsible for the possible formation of impurities and secondary phases.

Appendix B
Settings of X-Ray Diffractometer

Diffractometer: Siemens, D5000

Step drive: Normal, coupled

Step mode: continuous scan

Step time: 0.1s

Step size: 0.02°

Start position: 2°

Stop position: 120°

Divergence slit: 0.299°

Antiscatter slit: 0.299°

Rotation: None

Tube current: 30 mA

Tube voltage: 50 kV

Appendix C
Fitting of X-Ray Data

To determine the lattice parameters, the peak position are determine by a fitting program called PROFILE, used in Dr. Sleight's lab. After choosing the peaks to be fitted (the program can not fit the whole spectrum all at once, for our film spectra, it is only able to fit one peak at a time), the program marks the peaks to get a starting point for the fit. These peak positions can be changed, if they do not seem likely. The raw data is fitted to the Pseudo-Voigt1 function (but other fit functions are available)

$$\frac{I}{I_0} = \eta \frac{1}{1+\left(\frac{X-p}{W}\right)^2} + (1-\eta) * 2^{-\left(\frac{X-p}{W}\right)^2} \qquad (7.1)$$

I is the intensity at the current angle, I_0 the intensity at the peak position, given by p in degrees 2θ, with X being the current angle and W=0.5*FWHM.

The parameters that are varied by this function to determine the best fit are therefore I_0, p, W and the mixing factor η, because the Pseudo-Voigt1 function is a combination of a Lorentzian and a Gaussian. The quality of the fit is determined by to quantities the reliability (Rel);

$$Rel = \left[\frac{\sum W * (I_{obs} - I_{cal})^2}{\sum W * I_{obs}^2}\right]^{1/2} * 100\% \qquad (7.2)$$

and a theoretical reliability (TR), which takes into account the statistical character of the observed intensities:

$$TR = \left[\frac{\sum W * I_{obs}}{\sum W * I_{obs}^2}\right]^{1/2} * 100\% \qquad (7.3)$$

W(x) is a weight function, usually set to give equal importance to all data points, but can be adjusted to either give the peaks or the data near the background more importance. The fit is accomplished by minimizing Rel and the better the fit, the closer TR is to Rel. For peaks with a high number of counts, Rel ≈ 4-5%, but for small and therefore noisy peak, Rel can be as high as 30%.